STUDIES OF TWO-PRONG INTERACTIONS IN K^+p AT 4.6 GeV/c AND π^+p AT 3.6 GeV/c

Jimmy N. MacNaughton
(Ph. D. Thesis)

May 1971

AEC Contract No. W-7405-eng-48

TWO-WEEK LOAN COPY

This is a Library Circulating Copy
which may be borrowed for two weeks.
For a personal retention copy, call
Tech. Info. Division, Ext. 5545

UCRL-20178

DISCLAIMER

This document was prepared as an account of work sponsored by the United States Government. While this document is believed to contain correct information, neither the United States Government nor any agency thereof, nor the Regents of the University of California, nor any of their employees, makes any warranty, express or implied, or assumes any legal responsibility for the accuracy, completeness, or usefulness of any information, apparatus, product, or process disclosed, or represents that its use would not infringe privately owned rights. Reference herein to any specific commercial product, process, or service by its trade name, trademark, manufacturer, or otherwise, does not necessarily constitute or imply its endorsement, recommendation, or favoring by the United States Government or any agency thereof, or the Regents of the University of California. The views and opinions of authors expressed herein do not necessarily state or reflect those of the United States Government or any agency thereof or the Regents of the University of California.

Contents

Abstract 1
I. Introduction 2
II. Experimental Details — The K^+ Experiment
A. Source of Film 4
B. Scanning Procedure 4
C. Measuring Procedure 4
D. Difficulties Encountered in the Measuring Process . . . 5
E. Kinematic Fitting 6
III. Cross-Section Determination for the K^+ Experiment
A. General Procedure 8
B. Determination of Total Cross Section 9
1. Estimate of Pion Contamination in Beam 9
2. Evaluation of Total Cross Section from Other Experiments 10
C. Determination of the Ratio of Two-Prong Cross Section to the Total Cross Section 10
D. Subdivision of Two-Prong Cross Section into Various Channels 11
1. Determination of Elastic-Scattering Cross Section σ_e 11
2. Determination of Cross Sections for Other Two-Prong Reactions 11
IV. K + p Elastic Scattering
A. Angular Distribution 13
B. Discussion and Comparison with Other Data 14
V. Single-Pion Production
A. The $K\Delta(1236)$ Final State 16
B. The $pK^*(891)$ Final State 17
C. The $pK^*(1420)$ Final State 19
D. Diffractive Dissociation 19
VI. Missing-Mass Events 21
A. The Reaction $K^+p \rightarrow K^+pMM$ 21
B. The Reaction $K^+p \rightarrow \pi^+pMM$ 21

VII. Experimental Details in the π^+ Experiment
A. Source of Film 22
B. Scanning 22
C. Measurement 23
1. Bookkeeping 23
2. Difficulties Avoided 23
D. Kinematic Fitting 24
1. Decision-Making 24
2. Remeasurement 24
3. Rejects 24
4. Reactions Considered 24
E. Proton Contamination 26
1. Correction for Proton Contamination 26
VIII. Cross Section Determination in the π^+p Experiment
A. Elastic-Scattering Cross Section 28
1. Selection of a Sample 28
2. Determination of W 28
3. Difficulties in Cross-Section Determination . . . 29
4. Results 33
5. Calculation of Errors 33
B. Determinations of Cross Sections for $\pi^+p \rightarrow \pi^+p\pi^+\pi^-$, $\pi^+p\pi^+\pi^-\pi^+\pi^-$ 34
C. Cross Sections for the Final States $p\pi^+\pi^0$, $\pi^+\pi^+n$, $p\pi^+MM$, $\pi^+\pi^+MM$, $p\pi^+\pi^+\pi^-\pi^0$, $\pi^+\pi^+\pi^+\pi^-n$, $p\pi^+\pi^+\pi^-MM$, $\pi^+\pi^+\pi^+\pi^-MM$, $p\pi^+\pi^+\pi^+\pi^-\pi^-\pi^0$, $n\pi^+\pi^+\pi^+\pi^+\pi^-\pi^-$, $p\pi^+\pi^+\pi^+\pi^-\pi^-MM$, $\pi^+\pi^+\pi^+\pi^+\pi^-\pi^-MM$ . . 34
IX. Elastic Scattering
A. Angular Distribution 36
X. The Reactions $p\pi^+\pi^0$ and $n\pi^+\pi^+$ 37
A. General Features 37
B. The $\pi\Delta(1236)$ Final State 37
C. Diffractive Dissociation of the Proton into $n\pi^+$ and $p\pi^0$ 38
D. ρ^+ Production 39
1. Determination of the Mass and Width of the ρ^+ . . 39
2. ρ^+-Diffraction Interference 40
3. Momentum Transfer Dependence of ρ^+ Production . 44

4. Spin Density Matrix Elements 45
5. Δ^{++} - ρ^{+} Interference Model 46
6. Difficulties of Determination of π-π Phase Shifts . 48
E. $N^{*}(1688)$ 48
F. Other Peaks in Mass Spectra 48
1. $\pi^{+}\pi^{+}$ Spectrum 48
2. $\pi^{+}\pi^{0}$ Spectrum 50
XI. Missing-Mass Events
A. The Final State π^{+}pMM 52
B. The Final State $\pi^{+}\pi^{+}$MM 52
XII. Acknowledgments 53
XIII. References 54
XIV. Tables 56
XV. Figures 80

Исследования взаимодействий K^+p при 4,6 GeV/c и π^+p при 3,6 GeV/c приводящих событиям с двумя ветками

Джимми Н. Макнотон

Lawrence Radiation Laboratory
University of California
Berkeley, California

май,1971

Абстракт

Эта диссертация касается вопросов образования двух заряженных частиц при реакции K^+ мезонов при 4,6 GeV/c и π^+ мезонов при 3,6 GeV/c в жидководородных пузырьковых камерах. При этом было рассмотренно упругое рассеяние, рождение одного π-мезона и несколько нейтральных гадронов.

При K^+ эксперименте были определены сечение и угловое распределение упругого рассеяния. Образование $\Delta(1236)$ и $K^*(890)$, распад которых был рассмотрен, составляет большую часть при рождении одного π-мезона. Кроме того было образовано $K^*(1420)$. Также было замечено диффракционное разъединение $p \to p\pi^0$. При рождении нескольких незаряженных гадроннов были образованы $\Delta(1236)$, $K^*(890)$, $\eta(548)$.

При π^+ эксперименте были определены сечение и угловое распределение упругого рассеяния. Образование $\Delta(1236)$, ρ^+ и диффракционное разъединение $p \to p\pi^0$ и $p \to n\pi^+$ составляют большую часть при рождении одного

π- мезона. Была замечена интерференция между образованием ρ^+ и диффракцией. Исследовалось также свойства образования и распада $\Delta(1238)$ и ρ^+ подчеркивая следствия других процессов на образование ρ^+. Кроме того было образовано $N^*(1688)$ при больших переданных импульсах. Образование $\Delta(1238)$, A_2, η, ω, $\eta'(960)$ составляют большую часть при рождении нескольких незаряженных гадронов.

STUDIES OF TWO-PRONG INTERACTIONS IN K^+p AT 4.6 GeV/c AND π^+p AT 3.6 GeV/c

Jimmy N. MacNaughton

Lawrence Radiation Laboratory
University of California
Berkeley, California 94720

May 1971

ABSTRACT

This thesis covers studies of two-prong interactions produced by a K^+ beam of 4.6 GeV/c and a π^+ beam of 3.6 GeV/c interacting in liquid hydrogen bubble chambers. Elastic scattering, single-pion production, and production of multiple neutral hadron processes were studied.

In the K^+ experiment, the cross section and angular distribution of elastic scattering were measured. Single-pion production has large contributions from $\Delta(1236)$ and $K^*(890)$, whose production and decay characteristics were studied. $K^*(1420)$ is also produced, and there is evidence of diffractive dissociation of $p \rightarrow p\pi^0$. The multiple neutral hadron events contain production of $\Delta(1236)$, $K^*(890)$ and $\eta(548)$.

In the π^+ experiment the cross section and angular distribution of elastic scattering were measured. Single-pion production has large contributions from $\Delta(1238)$, ρ^+ and diffractive dissociation $p \rightarrow p\pi^0$ and $p \rightarrow n\pi^+$. Evidence is presented for interference between ρ^+ production and diffraction. Production and decay characteristics of the $\Delta(1238)$ and ρ^+, with special emphasis on the effects of other processes on the study of the ρ^+ were investigated. There is also evidence of $N^*(1688)$ production at relatively large momentum transfer. The multiple neutral hadron events contain production of $\Delta(1238)$, A_2, $\eta, \omega, \eta'(960)$.

I. INTRODUCTION

In January 1963 the 20-in. Brookhaven National Laboratory liquid hydrogen bubble chamber was exposed to a π^+ beam of 3.67 GeV/c. Analysis of the two-prong events in the summer of 1964 led to study of diffractive dissociation of the proton into proton + π^0, a relatively new idea at that time. Further analysis suggested a shift in the mass of the ρ^+ produced in the final state ρ^+p in the region of overlap with diffraction. Subsequently two-prong events were studied in an exposure of the BNL 80-in. hydrogen bubble chamber with a K^+ beam of 4.6 GeV/c. The two-prong events were analyzed, primarily to look for diffractive dissociation $p \rightarrow p\pi^0$ in this reaction also. Some evidence for this process was found, but the cross section was too small to allow a detailed study. Many other processes in the two-prong events were studied.

In the Fall of 1966 the 72-in. LRL hydrogen bubble chamber was exposed to a π^+ beam of 3.6 GeV/c. This experiment provided much better statistics, and the earlier work could be pursued in more detail. This experiment has been long in the analysis. In the meantime there have been many studies of diffraction dissociation. This experiment has produced evidence for interference between ρ^+ production and diffraction which was fit by a very simple parametrization. Many other properties of two-prong interactions were also studied.

Both the K^+ and π^+ experiments were carried out by using traditional analysis methods for bubble chamber experiments. Pictures were taken of the bubble chamber, and the film was analyzed over a period of several years. Events of interest were located by scanners using scanning machines, and then recorded either on IBM cards or on magnetic tape.

Accurate measurements of the tracks were made by using Franckensteins or Flying Spot Digitizer (FSD)—a semiautomatic measuring machine. Both off-line and on-line Franckensteins were used. Measurement rates were about 4 events per hour for off-line Franckensteins, 8 events per hour for on-line Franckensteins, and 100 events per hour for the FSD. However, the FSD required human premeasuring of three crude points per track—"roads." The making of "roads" proceeded at 15 events per hour.

Sections II - VI deal with the K^+ experiment, Sections VII - XI with the π^+ experiment. Section II gives experimental details; Section III, cross section determination; Section IV, elastic scattering; Section V, single-pion production; Section VI, missing-mass events for the K^+ experiment; Section VII, experimental details; Section VIII, cross-section determination; Section IX, elastic scattering; Section X, single-pion production; and Section XI, missing-mass events for the π^+ experiment.

II. EXPERIMENTAL DETAILS—THE K^+ EXPERIMENT

A. Source of Film

The data came from a 50,000-picture exposure of the BNL 80-in. hydrogen bubble chamber at the Alternating Gradient Synchrotron. An electrostatically separated beam of momentum 4.6 GeV/c was used.[1,2] The film was taken in the Fall of 1964 and Spring of 1965. Figure 1 is a typical frame of film.

B. Scanning Procedure

About 90% of the film was scanned at scanning tables for all two-, four-, and six-prong events and for tau decays ($K^+ \rightarrow \pi^+\pi^+\pi^-$). Secondary decays of K^0, Λ, $K^\pm$, $\Sigma^\pm$ were included. Information about the events was recorded on IBM cards. Table II contains a list of the number of events of each topology found during this scan. The remainder of this discussion concerns only two-prong events.

C. Measuring Procedure

The first measurement for all events was carried out by the Flying Spot Digitizer (FSD). The FSD required human premeasuring of three crude points per track—"roads." Roads were made for all two-prong events. For the 90% of the film which had a prior scan, information from the previous scan was used to locate events.

A set of IBM cards was generated that contained information recorded during the road-making process. Only those events included in this set of cards were analyzed further. For 10% of the film, scanning and road-making were carried out simultaneously. This subsample should have a higher effective scanning efficiency. Most two-prong events which had a secondary positive decay were included in the sample of two-prong events. Events which were called "two-prong + vee" were not analyzed as two-prong events. Sometimes the vees were not real, e.g., electron pairs. A few legitimate two-prong events were lost for this reason.

After the road-making, events were measured by the FSD. Events for which the first FSD measurement was unsatisfactory were again "road-made" and remeasured by the FSD, and failures on the second measurement were measured on an off-line Franckenstein. Off-line Franckenstein measurements proceeded at the rate of 4 events/hour. The results of FSD and Franckenstein measurements were analyzed by

the kinematic fitting program PACKAGE. The results of the fitting program were examined for each event.

D. Difficulties Encountered in the Measuring Process

If one or more tracks failed to reconstruct, or if no satisfactory kinematic fit was obtained, the event was remeasured. If it was decided that the event should not be included in subsequent analysis, it was rejected. Reasons for rejection were as follows:

1) Not beam track—the measured momentum of the beam track was more than 3 standard deviations away from the average beam momentum.

2. Outside fiducial volume.

3. Zero constraint—if an interaction or decay occurred so close to the primary vertex that the momentum measurement of the track had an error of 39% or more and if the kinematic fitting hypothesis $K^+p \rightarrow K^+p$ did not succeed, the event was rejected.

4. Ambiguous—if more than four nonstrange kinematic fitting hypotheses of the same constraint class appeared reasonably likely the event was rejected. In all except 10 cases the choice was between more than four missing-mass hypotheses.

5. Not to be measured—event could not be measured because of damaged film, obscuration by flare, or the like.

6. No event—it was decided that what had been measured was just a coincidence.

Table III lists the number of events rejected for each of the above reasons. A large number of events that were found on the original scan could not be located while making roads. There were a number of difficulties:

1) The film was very brittle. Frequently the film was damaged between scanning and road-making.

2) Many events were covered in one view by the flare. These events were frequently recorded while road-making.

3) Certain mistakes, such as frame-number errors on the original scan, caused the event to be missed while road-making.

4) Some marginal events, such as events from slightly off-beam tracks, were recorded by the initial scanner but thrown out while road-making.

5) Finally, some valid events that were recorded on the original scan were not found while road-making.

Difficulties 1), 2), 3) and 4) are largely nonbiasing. Difficulty 5) increases somewhat the number of valid events which were not measured; the scanning efficiency is thus somewhat lower than it would have been if a different technique had been used.

E. Kinematic Fitting

The following hypotheses were included in the kinematic fitting program:

$$K^+p \rightarrow K^+p \quad (1)$$

$$K^+p \rightarrow K^+p\pi^0 \quad (2)$$

$$K^+p \rightarrow K^0p\pi^+ \text{ (no decay of } K^0 \text{ seen)} \quad (3)$$

$$K^+p \rightarrow K^+\pi^+n \quad (4)$$

$$K^+p \rightarrow K^+K^+\Lambda^0 \text{ (no decay of } \Lambda^0 \text{ seen)} \quad (5)$$

$$K^+p \rightarrow K^+K^+\Sigma^0 \text{ (no decay of } \Sigma^0 \text{ seen)} \quad (6)$$

$$K^+p \rightarrow K^+p + \text{neutrals} \quad (7)$$

$$K^+p \rightarrow \pi^+p + \text{neutrals} \quad (8)$$

$$K^+p \rightarrow \pi^+K^+ + \text{neutrals} \quad (9)$$

$$K^+p \rightarrow K^+K^+ + \text{neutrals} \quad (10)$$

$$K^+p \rightarrow \pi^+\pi^+ + \text{neutrals}. \quad (11)$$

A reaction with no missing neutrals leads to a four-constraint fit; one missing neutral, a one-constraint fit; two or more missing neutrals a zero-constraint or missing-mass fit.*

Reactions (1), (2), (3), (7), and (8) are included in the subsequent analysis. In addition the two-prong + vee topology includes events from reaction (3) which can be identified with essentially no ambiguity problems. These events were processed by Chumin Fu and are included in the analysis of reaction (3). Reactions (4), (5), (6), (9), (10), (11) were not studied owing to the extreme difficulty of picking out these reactions from the other reactions.

*A missing-mass "fit" is really a calculation rather than a fit, but it is considered as a fit in this discussion. A "no fit" event is thus an event which had neither acceptable constrained fits nor acceptable missing-mass "fits."

If the event fit $K^+p \rightarrow K^+p$ with $\chi^2 < 24$, this hypothesis and no other was accepted. One event fit $K^+p \rightarrow K^+p$ with either outgoing track as the K^+ or p. In this case both hypotheses were accepted. If the event was not yet accepted, all tracks were visually inspected to obtain an ionization estimate. All one-constraint hypotheses with $\chi^2 < 6.7$ which had masses consistent with ionization were accepted with the exception that the hypotheses $K^+p \rightarrow K^+K^+\Lambda^0$ and $K^+p \rightarrow K^+K^+\Sigma^0$ were considered only if no other one-constraint hypothesis was acceptable. If no one-constraint hypothesis was acceptable, all missing-mass fits were accepted, provided that all mass hypotheses were consistent with ionization and provided that the missing mass was large enough for the production of two neutral hadrons. If no acceptable fit was found, the event was remeasured.

After all measurements were finished, some events were still unresolved for one of two reasons:

1) There was no measurement where all tracks reconstructed.
2) The event failed to achieve an acceptable fit.

There were 10,606 accepted events, 3870 rejected events, and 867 unresolved events.

The value for the beam momentum used in kinematic fitting for each event was a weighted average of the individually measured beam momentum for that event and an empirically determined mean beam momentum. The mean momentum at the center of the chamber was 4600 ± 40 MeV/c.

III. CROSS-SECTION DETERMINATION FOR THE K^+ EXPERIMENT

A. General Procedure

Due to the fact that the two-prong events were processed separately from events of other topologies, it was difficult to compare absolute numbers of two-prong events with events of other topologies at any stage of the experiment after the initial scan. However, the ratio of the two-prong cross section to the total cross section can be determined from the original scan listing. Also, owing to the large numbers of events rejected and lost during road-making (discussed previously) it is difficult to compare numbers of two-prong events used in analysis with numbers found while scanning. However, the reasons for rejecting and losing events are largely independent of which reaction a particular event represents, so the ratio of the numbers of events in a given reaction to the number of two-prong events can be relatively accurately determined. Corrections are made for the effects of ambiguous and zero-constraint rejects.

The cross-section determination is thus subdivided into three parts:

1) Determination of total K^+p cross section.
2) Determination of the ratio of two-prong cross section to total cross section.
3) Subdivision of the two-prong cross section into various channels.

Most emphasis is given to determination of elastic-scattering cross section since it is relatively easy to separate elastic-scattering events from other two-prong events, but it is difficult to separate the remaining two-prong events into various reactions in a substantial number of cases. Let σ_p = cross section for a particular reaction:

σ_2 = total two-prong cross section,
σ = total K^+p cross section at 4.6 GeV/c,

$$\sigma_p = \sigma \times \frac{\sigma_2}{\sigma} \times \frac{\sigma_p}{\sigma_2} .$$

B. Determination of Total Cross Section

The total cross sections measured by counter experiments are much more accurate than total-cross-section estimates from this experiment. Comparison between total-cross-section estimates normalized from $K^+ \rightarrow \pi^+\pi^+\pi^-$ and the counter measurements provides a useful upper limit on π^+ contamination in the beam.

1. Estimate of Pion Contamination in Beam

From the number of three-prong events, N_τ, one can determine the K^+ path length by using the relation

$$\ell_K = \frac{P_K C \tau_K}{M_K B} N_\tau ,$$

where B is the three-prong decay branching ratio. For these quantities we use the values

$$P_K = 4.6 \text{ GeV/c},$$

$$M_K = 0.494 \text{ GeV},$$

$$C = 3.0 \times 10^{10} \text{ cm/sec},$$

$$\tau_K = 1.235 \times 10^{-8} \text{ sec},$$

$$N_\tau = 709.$$

The value of B poses a minor problem: the τ branching ratio is well known to be $5.57 \pm 0.04\%$. However, the $K_{\pi 2}$, K_{e3}, $K_{\mu 3}$, and τ' modes can, through Dalitz pair emission, simulate a three-prong decay. Occasionally such "fake" τ's are recognized by the scanner and are not recorded. To avoid uncertainty on this point we note that the probability of fake τ decay is 0.39%, and use for B the value $5.57 + 0.39/2 \pm 0.39/2 = 5.77 \pm 0.20\%$.

From the 709 three-prong events we determine a path length of $(4.24 \pm 0.21) \times 10^7$ cm, where the error includes both the uncertainty in B and the statistical error.

Finally we get the total K^+p cross section:

$$\sigma = \frac{A_H \times N_K}{\rho_H \times N_A \times \ell_K} ,$$

where

A_H = atomic weight of hydrogen = 1.008 g,

ρ_H = density = 0.0629 g/cm^3,

N_A = Avogadro's number = 6.02×10^{23},

N_K = number of K interactions = 27376.

From these numbers we find that $\sigma = 17.2 \pm 1.2$ mb, where we have included a $\pm 5\%$ uncertainty from the previously mentioned topological variations in scanning efficiency.

2. Evaluation of Total Cross Section from Other Experiments

A suitable average of values given in the literature[3] appears to be 17.2 ± 0.2 mb. The fortuitously good agreement between this value and and our measurement allows us to set some rough limits on pion contamination. Thus if σ_K, σ_π are true kaon and pion total cross sections and σ_{KM} is the measured kaon cross section normalized on τ decays and if x is the number of pions for each kaon in the beam, one easily shows that

$$x = \frac{\sigma_{KM} - \sigma_K}{\sigma_\pi} .$$

Substituting in $\sigma_{KM} = 17.2 \pm 1.2$ mb, $\sigma_K = 17.2 \pm 0.2$ mb, and $\sigma_\pi = 28$ mb,

$$x = 0 \pm 4\% .$$

C. Determination of the Ratio of Two-Prong Cross Section to the Total Cross Section

A listing obtained directly from the initial scan at scan tables for 90% of the film was used in this determination. The number of two-prong events with no V^0 found was 14,954. The total number of interactions found was 26,552. 709 three-prong decays were found. 824* events should be added to both the number of two-prong events and the total number of events to correct for losses of elastic-scattering events where the proton was so short that the event was not found by the scanner:

*This number differs from the estimate of the same correction in the next section since the sample of events used here is the set of events found on the initial scan, whereas the next section deals with accepted events. The assumption made is that the size of the correction scales with total number of two-prong events in the sample.

$$\frac{\sigma_2}{\sigma} = \frac{15778}{27376} = 0.576.$$

The errors are mostly from topological variation of scanning efficiency and misidentification of event types. We assume that the scanning efficiencies for the major topologies do not differ by more than ± 5%. This leads to an error in σ_2/σ of 0.025. The statistical error is 0.003, which is negligible. Thus we take $\sigma_2/\sigma = 0.576 \pm 0.03$, from which $\sigma_2 = 9.9 \pm 0.5$ mb. It should be emphasized here that σ_2 is the cross section for two-prong events not accompanied by a vee.

D. Subdivision of Two-Prong Cross Section into Various Channels

Table IVa gives the distribution of two-prong events into various subclasses. Events which were rejected as ambiguous or zero constraint (Table III) were included in Table IVa as events with two or more missing neutrals. All other rejects (Table III) were assumed to divide up into various categories in just the same manner as accepted events and were not included in the determination. 633 events are added to the number of elastic-scattering events to correct for losses of elastic-scattering events with short recoil protons.

1. Determination of Elastic-Scattering Cross Section σ_e

$$\frac{\sigma_e}{\sigma_2} = \frac{4670}{4670+7370} = 0.388 \pm 0.02.$$

The error comes from a conservative estimate of systematic errors such as possible biases in the rejected events or events which failed to be measured successfully and uncertainties in extrapolating the elastic-scattering distribution to small momentum transfer [less than 0.05 $(\mathrm{GeV}/c)^2$]. The elastic-scattering cross section σ_e is thus determined to be $\sigma_e = 0.576 \times 0.388 \times 17.2 = 3.85 \pm 0.25$ mb, where the error is estimated by assuming that the errors on all three factors are independent.

2. Determination of Cross Sections for Other Two-Prong Reactions

The biggest difficulty encountered in determining cross sections for inelastic two-prong reactions is the numerous events which are ambiguous between two or more reactions. Table XVb lists both the number of events accepted unambiguously and ambiguously as $K^+p\pi^0$, $K^0p\pi^+$, and $K^+\pi^+n$.

Because of ambiguities in the kinematic fits of the two-prong events, only rough estimates of the $K^+p\pi^0$ and $K^+n\pi^+$ cross sections can be given. If we assign to each of these final states the number of unambiguous fits plus one-half of the ambiguous fits with an error corresponding to one-half the ambiguous fits, we obtain, for the $K^+p\pi^0$ and $K^+n\pi^+$ cross sections, estimates of 0.8 ± 0.2 and 0.6 ± 0.3 mb respectively. These estimates are, if anything, likely to be on the high side since they do not correct for multi-neutral events ambiguous with the one-constraint fits.

The cross section for the $K^0p\pi^+$ final state was determined to be 1.06 ± 0.1 mb in collaboration with Chumin Fu, using the two-prong + vee topology.

The cross section for production of events with two prongs and multi-neutrals is 4.0 ± 0.5 mb, where the error is an estimate of systematic uncertainties.

IV. K + p ELASTIC SCATTERING

A. Angular Distribution

The complete center-of-mass angular distribution is shown in Fig. 2. An azimuthal correction has been applied which is explained in a footnote for Table V. The measured values of $d\sigma/dt$ as a function of $|t|$, the squared momentum transfer, are given in Table V and shown, for the forward angles, in Fig. 3. A satisfactory fit of the data between $|t| = 0.05$ and $|t| = 0.8$ $(\mathrm{GeV}/c)^2$ can be made to the form

$$\frac{d\sigma}{dt} = \left(\frac{d\sigma}{dt}\right)_0 e^{Bt} .$$

The result is $(d\sigma/dt)_0 = 16.0 \pm 1.3$ mb/$(\mathrm{GeV}/c)^2$, $B = 4.2 \pm 0.2$ $(\mathrm{GeV}/c)^{-2}$, where the errors include the systematic uncertainty due to possible pion contamination. The ratio of real to imaginary part of the forward scattering amplitude, α, with 17.2 mb taken as the total K^+p cross section, is

$$|\alpha| = \left|\frac{\mathrm{Rl}\, f(0)}{\mathrm{Im}\, f(0)}\right| = 0.25^{+0.14}_{-0.25} .$$

This result may be compared with the following theoretical expectations: (i) The Regge pole analysis by Dass, Michael, and Phillips[4] leads to a prediction of $\alpha = -0.4$ at our momentum. (ii) A variety of dispersion relation calculations has given values of α ranging from -0.1 to -0.4 (Ref. 5). It is clear that the errors of our experimental result are too large to permit differentiation between various predictions. It is worth noting, however, that this result appears somewhat smaller and perhaps in better agreement with theoretical expectations than the value $|\alpha| = 0.60 \pm 0.14$ at 7.3 GeV/c quoted by Chien et al.[6]

As is clear from the distribution shown in Fig. 2, there is a small amount of scattering in the backward direction. The cross section for scattering through c. m. angles greater than 90 deg is 13 ± 4 μb. The corresponding figures for 3.0, 3.5, and 5 GeV/c are 33 ± 10, 24 ± 6, and 8 ± 5 μb respectively.[6] Using only the events from $\cos\theta = -0.92$ to $\cos\theta = -1$, we estimate $d\sigma/d\Omega\,(180\text{ deg}) = 7^{+5}_{-3}$ μb/sr. A much more precise measurement has been done at 5.2 GeV/c by Baker et al.,[7] with the result $d\sigma/d\Omega\,(180\text{ deg}) = 10 \pm 3$ μb/sr. It is interesting to note that a recent analysis of K^-p scattering at 4.6 GeV/c reports no events at angles greater than 90 deg and sets an upper limit to the backward scattering cross section of 2 ± 1 μb.[8] The observed backward scattering in K^+p is

generally interpreted in terms of u-channel baryon exchange. Such exchange would, for K^-p, require S = + 1 baryons, for whose existence there is no clear evidence.

B. Discussion and Comparison with Other Data

We have studied the properties of the forward diffraction peak in K^+p scattering, using both our data and other published information. In order to have some reasonably precise quantities calculated uniforml for all the data, we have made fits at all the momenta to the form

$$\frac{d\sigma}{dt} = \left(\frac{d\sigma}{dt}\right)_0 e^{Bt}, \quad \text{with } 0 < |t| \leq 0.8\ (\mathrm{GeV}/c)^2 .$$

In Fig. 4 we plot the values of B for momenta between 1.2 and 14.8 GeV/c. It is clear that the points follow a smooth curve, and indeed are excellently fitted by the function

$$B = 6.8\ \beta^2\ (\mathrm{GeV}/c)^{-2} ,$$

where β is the c. m. velocity of the K^+p system. There are several interesting remarks to make here:

(a) The proportionality between B and β^2 also occurs in the other well-known case of substantial shrinkage of the diffraction peak with energy, namely proton-proton elastic scattering. Indeed, Krisch[9] has suggested $\beta^2 P_\perp^2$, where $P_\perp$ is the transverse momentum ($P_\perp^2 \approx |t|$ at high energy) as a universal variable in terms of which p-p angular distributions can be represented. In p-p scattering the coefficient of proportionality B/β^2 is larger, namely about 10 $(\mathrm{GeV}/c)^{-2}$ instead of 6.8 $(\mathrm{GeV}/c)^{-2}$. This similarity to the p-p interaction is but one of many including the absence of resonances and close resemblance in the momentum dependence of elastic and inelastic cross sections.

(b) The asymptotic value of B (assuming that this has meaning—that is, that the Pomeranchuk trajectory is flat) is 6.8 $(\mathrm{GeV}/c)^{-2}$. It should be noted that for K^-p the value of B changes very little with momentum and appears to have, when fitted over the same range of $|t|$ a value of 7.1 to 7.2 $(\mathrm{GeV}/c)^{-2}$. Thus the K^+ and K^- scattering in the diffraction peak do become nearly identical at high momentum, although very different at low momenta. This value of B is also in good agreement with the value obtained in pion elastic scattering, again almost independently of incident momentum.

(c) If we assume that asymptotically (i) the real part of the forward scattering amplitude goes to zero, (ii) the total cross section remains at 17.2 mb, (iii) the linear exponential remains a good representation of the angular distribution from $t = 0$ to at least $|t| \gtrsim 0.6\ (\mathrm{GeV}/c)^2$, the elastic cross section σ_e has the asymptotic value of 2.2 mb, and the ratio σ_e/σ_t has the limit 0.13. Both of these figures are substantially lower than those at the highest measured momentum of 14.8 GeV/c, $\sigma_e = 3.41 \pm 0.17$ mb, $\sigma_e/\sigma_t = 0.20$ (Ref. 11).* However, it is interesting to note that for K^-p at 10 GeV/c, with $\sigma_e = 3.20 \pm 0.14$ mb, $\sigma_t = 22.5 \pm 0.2$ mb, the value of σ_e/σ_t, namely 0.142 ± 0.006 (Ref. 10), is close to the above asymptotic limit.

We now consider briefly the phase of the forward K^+p amplitude. For all momenta at which measurements have been made, the forward cross section $(d\sigma/dt)_0$ always lies substantially higher than the optical value. In fact, as indicated earlier, both dispersion-relation calculations and Regge-model predictions lead one to expect a substantial ratio of real to imaginary forward amplitudes, decreasing in magnitude with increasing momentum. The experimental data do not exhibit any clear trend with changing momentum except the existence of a sizable real part for the forward amplitude. More precise data are clearly required to study this question, particular since the possible presence of a significant spin-flip term may make the usual extrapolations to $t = 0$ somewhat uncertain.

*This experiment found a substantial real part of the forward amplitude, which also indicates that 14.8 is far from asymptopia if assumption (i) is valid.

V. SINGLE-PION PRODUCTION

The list of reactions studied in this section is presented in Table VI. The data came from the two-prong topology and also, for reaction (1), from the two-prong + vee topology for which the data were obtained from Chumin Fu.

A. The $K\Delta(1236)$ Final State

The data for the study of this state come from topologies (i) and (ii) fitting the reaction (1) (Table VI). To avoid ambiguity problems for the two-prong events we confine ourselves to the region of momentum-transfer-squared between incident and outgoing K, $-t_K < 2\ (\mathrm{GeV}/c)^2$. The data from topology (ii) indicates that the Δ population at higher momentum transfers corresponds to a cross section of less than 15 μb, well within the uncertainties of the overall ΔK cross section. In Fig. 5 we show the $p\pi^+$ mass distribution for all $K^0 p\pi^+$ events of topologies (i) and (ii) with $-t_K < 2\ (\mathrm{GeV}/c)^2$, indicating also the ambiguous contribution. It is clear that for $p\pi^+$ masses below 1.8 GeV this contribution is negligible. A fit to the histogram in Fig. 5 for $M(p\pi^+) < 1.75$ GeV with a superposition of Δ and phase space leads to a cross section for Δ production in the reaction (1) of 0.42 ± 0.03 mb.

The form of Breit-Wigner used for the Δ was

$$\frac{\frac{\Gamma_0}{m}\left(\frac{q^3}{1+\frac{q^2}{m_\pi^2}}\right)\left(\frac{q_0^3}{1+\frac{q_0^2}{m_\pi^2}}\right)^{-1} p^*}{(m^2 - m_0^2)^2 + m_0^2\left(\frac{\Gamma_0 \frac{q^3}{1+q^2}}{\frac{q_0^3}{1+\frac{q_0^2}{m_p^2}}}\right)},$$

where

$$q = \sqrt{\left(\frac{m^2 + m_p^2 - m_{\pi^+}^2}{2m}\right)^2 - m_p^2}$$ = momentum of outgoing proton in $p\pi^+$ center of mass,

$$q_0 = \sqrt{\left(\frac{m_0^2 + m_p^2 - m_{\pi^2}}{2m}\right)^2 - m_p^2},$$

$$p^* = \sqrt{\left(\frac{E_0^{\,2} + m^2 - m_{K^0}^{\,2}}{2E_0}\right)^2 - m^2}$$ = momentum of K^0 is overall center of mass,

E_0 = total center of mass energy,
m = mass of $p\pi^+$ system,
m_{K^0} = K^0 mass,
m_p = proton mass,
m_π = π^+ mass,
m_0 = 1225 MeV,
Γ_0 = 105 MeV.

The amount of Δ^{++} production was determined from the integral of the Breit-Wigner over the fitting region. The overall $K\Delta$ production from K^+p interactions including all final channels is then, using the appropriate Clebsch-Gordan coefficients, 0.56 ± 0.04 mb. The t_K distribution and Δ decay density matrix elements are shown in Figs. 6 and 7. The momentum transfer distribution has a dip in the forward direction, but appears to be nearly exponential for $0.2 \leq t \leq 1$ $(\mathrm{GeV}/c)^2$. It has been fitted to an exponential of the form $(d\sigma/d\tau) \propto e^{Bt_K}$, $0.2 < -t_K < 1.0$ $(\mathrm{GeV}/c)^2$, where $B = 4.9 \pm 0.6$ $(\mathrm{GeV}/c)^{-2}$. Except at very low momentum transfers the density matrix elements are in fairly good agreement with the simple Stodolsky-Sakurai[12] predictions $\rho_{33} = 0.375$, $\mathrm{Re}\,\rho_{3,-1} = 0.21$, $\mathrm{Re}\,\rho_{31} = 0$. This behavior is known to hold over a range of incident momenta from essentially threshold to the highest momenta studied.

B. The $pK^*(891)$ Final State

For momentum-transfer-squared between initial and final proton $-t_p$ less than 1.2 $(\mathrm{GeV}/c)^2$, the final proton is recognizable by ionization. With this reaction, one-constraint fits to topology (i) are either unambiguous or have as their only ambiguity an interchange between the outgoing kaon and the outgoing pion. It follows that in this low-momentum-transfer region the $K^{*+}(891)$ produced in the reaction $K^+ + p \rightarrow p + K^{*+}(891)$ can be detected by plotting the $K\pi$ mass spectrum for all events in the various classes listed in Table VII.

For the ambiguous events (last row of Table VII) the choice of the $K^0\pi^+$ mass as the one plotted is arbitrary: since the proton is directly recognized and accurately measured, the $K\pi$ mass is essentially

independent of whether the $K^0\pi^+p$ or $K^+\pi^0p$ fit is the one chosen. The validity of this assertion has been verified experimentally by comparison of $K\pi$ masses in ambiguous events. The mass distribution, for $-t_p < 1.2$ $*\mathrm{GeV}/c)^2$, of the events chosen according to Table VII[7] is shown in Fig. 8. A large $K^{*+}(891)$ peak is evident and leads to a cross section in this region of momentum transfer of 0.57 ± 0.04 mb for the sum of the $K^0\pi^+$ and $K^+\pi^0$ final states.

For higher momentum transfers, $-t_p > 1.2$ $(\mathrm{GeV}/c)^2$, the ambiguity problems are somewhat worse in that the proton identification is no longer clear-cut. We show in Fig. 9 the $K\pi$ mass spectrum for such events which have at least one fit as $K^0p\pi^+$ or $K^+p\pi^0$. Every $K\pi$ mass combination corresponding to an acceptable fit with $-t_p > 1.2$ $(\mathrm{GeV}/c)^2$ is shown, except that where $K^0p\pi^+$ is ambiguous with $K^+p\pi^0$ with the <u>same</u> particle as proton, only the $K^0\pi^+$ mass is shown. The most significant feature in Fig. 9 is the contribution at 1420 MeV which will be discussed in the next section. There is also a small K^* signal near 891 MeV of 12^{+10}_{-5} events, corresponding to a cross section of 10^{+8}_{-4} μb. The overall pK^{*+} cross section for all momentum transfers is then $0.57 + 0.01 = 0.58 \pm 0.04$ mb. This cross section includes both final states $K^0p\pi^+$ and $K^+p\pi^0$, and presumably divides itself between them in the ratio 2:1 predicted by Clebsch-Gordan coefficients.

The momentum-transfer distribution from the sample of Table VII is shown in Fig. 10. It has been fitted to the form

$$\frac{d\sigma}{dt} \propto e^{Bt_p}, \quad 0.2 < -t_p < 1.0\ (\mathrm{GeV}/c)^2,$$

where $B = 3.6 \pm 0.4$ $(\mathrm{GeV}/c)^2$. It is perhaps of interest to note that the values of B for both the $K\Delta(1236)$ and the $K^*(891)p$ channels are quite similar to the value 4.2 ± 0.2 $(\mathrm{GeV}/c)^2$ found in elastic scattering at just the same momentum. It is <u>a priori</u> far from obvious that such a similarity should be expected in view of the importance of Pomeranchuk exchange in the elastic channel and its absence in the channels under discussion.

We now consider the $K^*(891)$ decay, angular distributions, and confine ourselves to $-t_p < 1.2$ $(\mathrm{GeV}/c)^2$. The events in the last row of Table VII pose a slight problem in that although the $K\pi$ mass and t_p

are essentially independent of whether the K^* decay is actually $K^+\pi^0$ or $K^0\pi^+$, the decay angles are sensitive to this choice. A revealing feature of the ambiguity problem is illustrated in Fig. 11, which shows the $K^0p\pi^+$ Dalitz plots for two-prong ambiguous and unambiguous events. It is clear from Fig. 11 that the low-$p\pi^+$-mass half of the $K^*(891)$ band has essentially no ambiguous events. If interference between K^* and either Δ or background is neglected, parity conservation in the K^* decay requires that for every K^* event in the low-$p\pi^+$-mass half of the Dalitz plot with Jackson decay angles α, ϕ there is an event in the high-$p\pi^+$-mass half with angles $\pi-\alpha$, $\phi+\pi$. Consequently, events in the unambiguous low-$p\pi^+$-mass half of the Dalitz plot give unbiased decay angular distributions provided that appropriate folding is done. This choice of events was thus made for both $K^0p\pi^+$ and $K^+p\pi^0$ two-prong topologies, retaining of course all K^* events for the unambiguous two-prong + vee topology.

A sample of 350 K^* events so selected gives the density matrix elements shown in Fig. 12. The usual pattern of vector exchange dominance ($\rho_{00} \sim 0$) is evident, with significant pion exchange contributions at momentum transfers below 0.1 $(GeV/c)^2$.

C. The $pK^*(1420)$ Final State

In Figs. 8 and 9 there are enhancements at 1420 MeV for momentum transfers below as well as above 1.2 $(GeV/c)^2$. The enhancements correspond to 80±22 events for $-t_p < 1.2\ (GeV/c)^2$ and 30 ± 12 events for $-t_p > 1.2\ (GeV/c)^2$. The corresponding cross sections are 0.065 ± 0.02 and 0.025 ± 0.010 mb respectively. Thus the total $K^{*+}(1420)p$ cross section is 0.09 ± 0.025 mb. It is interesting to note that whereas only about 2% of the $K^*(891)$ events have $-t_p > 1.2\ (GeV/c)^2$, about 25% of the $K^*(1420)$ are produced with such large momentum transfers.

Because of ambiguities between $K^0\pi^+$ and $K^+\pi^0$ decays of the $K^*(1420)$, limited statistics, and significant background, we have not attempted to study the $K^*(1420)$ decay behavior in this experiment.

D. Diffractive Dissociation

Evidence for a process which has been called diffractive dissociation has been observed in a number of reactions.[13] It is expected that the proton dissociates into $p\pi^0$ and $n\pi^+$. This process should produce an enhancement at low $|t_{K^+}|$ and at low $m_{p\pi^0}$ and $m_{n\pi^+}$ in the final states $K^+p\pi^0$ and $K^+n\pi^+$, but not $K^0p\pi^+$. The reaction $K^+n\pi^+$

suffers from a large ambiguity problem and is not studied here. To reduce the ambiguity problem for the reaction $K^+p\pi^0$ in the diffraction region, the fiducial volume was reduced by throwing out events from the downstream part of the chamber to ensure enough track length to make a good momentum measurement of the fast outgoing K^+. The reaction $K^+p\pi^0$ is compared with $K^0p\pi^+$; diffractive dissociation should be present in the former, but not the latter final state. In this section the contribution to the $K^0p\pi^+$ final state from the topology two-prong + vee has not been included.

Two selection criteria have been applied to the data to reduce the background from other processes:

1) $K^*(890)$ has been removed.

2) Events where the cosine of the angle between incident and outgoing proton in the $p\pi$ center of mass lies between 0.5 and 1 have also been removed.

The purpose of the second criterion is to reduce background from processes which favor very small momentum transfer to the proton and which can contribute to both final states $K^0p\pi^+$ and $K^+p\pi^0$.

Figure 13a and 13b are scatter plots of $m^2_{p\pi}$ vs. $\Delta^2_{p\pi}$ for events consistent with these cuts for $K^+p\pi^0$ and $K^0p\pi^+$ respectively. In both figures there is strong evidence for $\Delta(1238)$ production at low t_{K^+}. In the mass region above the Δ there is an excess of events at very low t_{K^+} in the reaction $K^+p\pi^0$, but not $K^0p\pi^+$. Figures 14a and 14b show a $|t_K|$ distribution for the final states $K^+p\pi^0$, $K^0p\pi^+$ respectively for events satisfying selection criteria (1) and (2) and with $m_{p\pi^0}$ or $m_{p\pi^+}$ 1350 - 1800 MeV. Figure 14a is consistent with an exponential distribution e^{At_K} in the region $-t_K < 0.8$ with the value A being the same as for K^+p elastic scattering at this momentum, whereas the distribution in Fig. 14b is quite different.

Figure 15 shows the mass spectrum of the $p\pi^0$ system in the final state $K^+p\pi^0$ for events satisfying selection criteria (1) and (2) and with momentum transfer $-t_K$ to the $p\pi^0$ system less than 0.4 $(GeV)^2$. There is evidence of Δ^+ production near 1.225 GeV, and a pedestal underneath the Δ^+ extending from threshold to about 1.8 GeV, falling off gradually as the $p\pi^0$ mass increases, which is presumably due to diffraction dissociation. Present statistics do not allow identification of specific $p\pi^0$ resonances.

VI. MISSING-MASS EVENTS

Many two-prong events at this momentum have more than one missing neutral. In this case an effective mass of all missing neutral particles combined can be calculated provided the masses of all charged particles are known. In many cases at least one track cannot be identified uniquely; thus there are many ambiguities. There was a total of 3535 accepted missing mass events with a maximum of four acceptable hypotheses; 673 events were rejected because there were more than four acceptable hypotheses. Because of the large frequency of ambiguous events, a detailed analysis of the missing-mass events will not be attempted here; however, evidence for the production of η, $K^*(890)$, and Δ^{++} resonances is presented.

A. The reaction $K^+p \rightarrow K^+p$ MM

The distribution of the missing mass in this reaction, shown in Fig. 16, shows evidence for $\eta(548)$ production. Since some η production may also have been lost in the 673 events rejected as too ambiguous, no attempt is made to estimate the cross section for $\eta(548)$ production.

B. The reaction $K^+p \rightarrow \pi^+p$ MM

Figure 17 is a scatter plot of the MM vs. $m_{p\pi^+}$ systems. Figures 18 and 19 are projections of the MM and $m_{p\pi^+}$ spectra respectively. There is clear evidence for $K^*(890)$ and $\Delta^{++}(1238)$ production. There is an especially large concentration of events in the region where the $K^*(890)$ and $\Delta^{++}(1238)$ bands cross.

VII. EXPERIMENTAL DETAILS IN THE π^+ EXPERIMENT

A. Source of film

The data came from a 200,000-picture exposure with an electrostatically separated π^+ beam of the Lawrence Radiation Laboratory 72-in. hydrogen bubble chamber. The exposure was made in the Fall of 1966 at the Bevatron. The data were taken at several average beam momenta ranging from 3.56 to 4.00 GeV/c. The beam momentum was near the upper limit of the operating range and as a consequence proton contamination in the beam was considerable.

B. Scanning

About 75,000 pictures were scanned for all interactions. The remaining pictures were scanned for all interactions except two-prong interactions without stopping protons. All pictures were in addition scanned for one-prong and three-prong decays. It is very difficult to see decays $\pi^+ \rightarrow \mu^+\nu$ at 3.7 GeV/c owing to the very small angle between π^+ and μ^+. Most of the one-prong events found are not $\pi^+ \rightarrow \mu^+\nu$. The one-prong events were included in the scanning instructions to improve the scanning efficiency for two-prong events with short recoil protons. The one-prong events were measured because some might have been interactions in which two charged particles were actually produced, but one was a proton which had a range too small to be visible in the bubble chamber.

A number of interactions were found which appear to violate charge conservation. There are a number of reasons why charged tracks may not be seen, giving rise to the apparent violation of charge conservation-protons with extremely small rnage, negative particles which charge exchange close to the primary interaction, electrons with momentum greater than 180 MeV/c which cannot be distinguished by bubble density from strongly interacting particles, secondary interactions so close to the primary interaction that there appears to be only one interaction, or possible contamination of the hydrogen in the chamber with deuterium helium, or other nuclei. These interactions were recorded since they constitute an uncertainty in cross-section determination. In addition the four three-prong events identified as $K^+ \rightarrow \pi^+\pi^+\pi^-$ provided an estimate of 0.1% for K^+ contamination in the beam.

In order to identify as many strange particles as possible — Λ^0, Σ^+, Σ^0, Σ^-, K^+, K^-, K^0, Ξ^-, Ξ^0 — all secondary decays were

measured: neutral decaying into positive and negative track (vee), charged track decaying into one charged track + neutral(s), and $K^{\pm} \rightarrow \pi^{\pm}\pi^{+}\pi^{-}$ (tau decay). Electron pairs, π decays in flight and the like were often interpreted by scanners as secondary decays; these events are listed in the initial scan as topologies with secondary decays, but as soon as a decay or "vee" was discovered not to be legitimate evidence of strange-particle production, the event was reclassified as a different topology. The measurement of secondary decays was used in kinematic fitting only for strange particles. Table VIII contains a list of numbers of events of each topology found at each momentum during the original scan.

C. Measurement

Scanning and initial road-making were carried out simultaneously. After the events were road-made, they were measured by the FSD. Events which were not measured satisfactorily were again road-made and remeasured by the FSD. Those events which were not yet measured satisfactorily were remeasured on a Franckenstein measuring projector connected to the COBWEB on-line computer-controlled system.

1. Bookkeeping

The results of the initial road-making were recorded on magnetic tape. A record of each event found on the initial scan was thus generated. The results of each subsequent measurement were matched by a computer program with the record generated during original scan, and a new record containing both scan and measurement result information was generated and stored on magnetic tape. The status of any given event at any time could thus be determined from a magnetic tape record.

2. Difficulties Avoided

The data-handling system for this experiment was designed to avoid many of the difficulties which had been encountered in the earlier K^+ experiment. All events which had been found during the original scan could be located at any desired time because at the time of the original scan a measurement of the position of the vertex of the event was made so that it was known exactly where to look for each event. As each measurement was made a check was made to ensure that the position of the vertex according to

that measurement agreed with the position from the original scan.

All topologies were processed at the same time so that changes in the topological classification of an event did not lead to loss of events. Also there was no difficulty of a differential normalization factor for different topologies.

D. Kinematic Fitting

1. Decision-Making

The results of FSD and Franckenstein measurements were analyzed by the kinematic fitting program SIOUX. The results of kinematic fitting for each event were either examined in conjunction with a visual inspection of the event or were analyzed by a computer program written to simulate this procedure as closely as possible.[14] About one-half of the events were processed by the human method; the other half were sent to the computer program. The computer program failed to reach a decision for about 20% of the events it recieved, and these events were also processed by the human method.

2. Remeasurement

If one or more tracks failed to reconstruct or if no satisfactory kinematic fit was obtained, the event was remeasured.

3. Rejects

If it was decided that the event should not be included in subsequent analysis, it was rejected.

Table IXa gives a list of reasons for rejecting events. Table IXb gives a list of numbers of two-prong events rejected for each reason. Reasons 1, 2, 3, 4, 5, 7, 11 are nonbiasing. There were only a very small number of events rejected for reasons 1, 4, 6, 9, 10, 11. The number of rejects for reasons 8 and 10 will be taken into account for cross-section calculations.

4. Reactions Considered

The following hypotheses were included in the kinematic fitting program and considered at this stage:

for two-prong events:	Number of constraints
$\pi^+p \rightarrow \pi^+p$	4
$\pi^+p \rightarrow \pi^+p\pi^0$	1
$\pi^+p \rightarrow \pi^+\pi^+n$	1

$\pi^+p \to \pi^+p$ + neutrals	0
$\pi^+p \to \pi^+\pi^+$ + neutrals	0

for four-prong events:

$\pi^+p \to K^+K^-p\pi^+$	4
$\pi^+p \to \pi^+\pi^-p\pi^+$	4
$pp \to pp\pi^+\pi^-$	4
$\pi^+p \to \pi^+\pi^-p\pi^+\pi^0$	1
$\pi^+p \to \pi^+\pi^-\pi^+\pi^+n$	1
$\pi^+p \to \pi^+\pi^-p\pi^+$ + neutrals	0
$\pi^+p \to \pi^+\pi^-\pi^+\pi^+$ + neutrals	0

for six prong events:

$\pi^+p \to \pi^+p\pi^+\pi^+\pi^-\pi^-$	4
$\pi^+p \to \pi^+p\pi^+\pi^+\pi^-\pi^-\pi^0$	1
$\pi^+p \to \pi^+\pi^+\pi^+\pi^+\pi^-\pi^-n$	1
$\pi^+p \to \pi^+p^+\pi^+\pi^+\pi^-\pi^-$ + neutrals	0
$\pi^+p \to \pi^+\pi^+\pi^+\pi^+\pi^-\pi^-$ + neutrals.	0

The strange-particle reactions are discussed elsewhere.[15]

An estimate of the ionization of each track was made either visually or from information obtained from FSD measurement.[16] All hypotheses inconsistent with ionization were discarded. Also all hypotheses which had a χ^2 greater than the cutoff value were discarded. The cutoff values were: 4-constraint, 24; 1-constraint, 6.7. Unconstrained fits which had effective mass of neutral particles too small to be consistent with at least two neutral hadrons were also discarded. The remaining hypotheses were considered potentially acceptable. All potentially acceptable four-constraint hypotheses were accepted. If there were no potentially acceptable four-constraint hypotheses, all potentially acceptable one-constraint hypotheses were accepted. If there were no potentially acceptable four-constraint or one-constraint hypotheses, all potentially acceptable missing-mass hypotheses were accepted. If there were no potentially acceptable hypotheses, the event was remeasured.

E. Proton Contamination

There was substantial proton contamination in the beam. In order to monitor beam contamination all four-prong events were fit to reactions

$$\pi^+p \to \pi^+p\pi^+\pi^-$$
$$pp \to pp\pi^+\pi^-.$$

A small fraction of the events fit both reactions. Let $N\pi^+$ be the number of unique fits to $\pi^+p \to \pi^+p\pi^+\pi^-$ and Np be the number of unique fits to $pp \to pp\pi^+\pi^-$. Figure 20 shows a graph of $(N_p/N_p + N_{\pi^+}) \times 100$ as a function of roll number. Figure 20 shows that the proton contamination varied considerably during the experiment. The largest contribution to the error in this measurement of proton contamination is due to those events caused by π's and which fit $pp \to \pi^+\pi^-pp$ but not $\pi^+p \to \pi^+p\pi^+\pi^-$. These events are presumably rare, but we cannot measure how likely they are to occur since we have no rolls known to be uncontaminated. About 1 000 pictures were taken with incident protons with presumably very small pion contamination. These pictures were scanned, measured and processed just as if the beam were incident pions. No successful fits to $\pi^+p \to \pi^+p\pi^+\pi^-$ were achieved in this section of film.

1. Correction for Proton Contamination

To correct for proton contamination the rolls of film were divided into three sets.

1) Heavy contamination—the proton component comparable to or larger than the π^+ component in the beam. 6300 frames fell in this set.

2) Moderate contamination—those rolls with the largest proton contamination exclusive of the rolls in set 1. 18 200 frames fell in this set.

3) Low contamination—those rolls which did not fall in set 1 or 2. 50 400 frames fell in this set.

There were 366 unique four-constraint fits to $pp \to pp\pi^+\pi^-$ in set 1. The remaining rolls were subdivided into sets 2 and 3 such that there were the same number of unique fits to $pp \to pp\pi^+\pi^-$ in set 3 as in set 1. Events from set 2 were not included in subsequent analysis. Events in set 1 were subtracted from events in set 3 in all subsequent distributions, which should remove the proton contamination.

Whenever two-dimensional plots were made, those events in set 3 which were nearest neighbors to events in set 1 were removed. There were two exceptions to the above procedure:

a) Only a subsample of set 3 was used for cross-section determination. A weighting factor was introduced to compensate for the different number of unique four-constraint fits to $pp \rightarrow pp\pi^+\pi^-$ in this subsample

b) Since $pp \rightarrow pp$ cannot simulate backeard elastic scattering $\pi^+p \rightarrow p\pi^+$, no proton removal was made for the appropriate part of the $\pi^+p \rightarrow \pi^+p$ angular distribution.

The average proton contamination in the beam for the rolls in set 3 was 7%.

VIII. CROSS SECTION DETERMINATION IN THE π^+p EXPERIMENT

A. Elastic-Scattering Cross Section

1. Selection of a Sample

A subsample of the data was selected for cross-section determination in accordance with the following criteria:

1) All events recorded during the initial scan.

2) Relatively low proton contamination.

3) Only a small percentage of the events unresolved after three measurements.

The cross-section subsample was further subdivided into beam momentum regions 3.56 and 3.67 GeV/c.

Since the cross-section subsample was somewhat smaller than that used for the remaining analysis, it had fewer unique four-constraints fits to $pp \rightarrow pp\pi^+\pi^-$. To correct for this an appropriate weighting factor, W, was introduced. Given a number, N, of events in a sample, we estimate the number of events, N_π, produced by incident π^+ as $N_\pi = N - WN_p$, where N_p is the number of events in the proton test sample. Obviously the only effect of subtracting the small number of pion events in the proton test sample is to increase slightly the statistical errors since the only important measured quantities are ratios of numbers of events.

2. Determination of W

The number of unambiguous four-constraint fits to the reaction $pp\pi^+\pi^-$ in a sample of film was assumed to be proportional to the number of proton beam tracks in the sample. For the 3.56-GeV/c cross-section sample, 75 such fits were found; at 3.67 GeV/c, 220 fits. The proton test sample was divided into two parts for subtraction from the 3.56- and 3.67-GeV/c samples respectively. The first part had a beam momentum of 3.56 GeV/c and 72 such fits; the second had some 3.67-GeV/c film and some 4-GeV/c film and 294 such fits. Thus for 3.56 GeV/c, $W = 1.04 \pm 0.17$ and for 3.67 GeV/c, $W = 0.75 \pm 0.07$, where the errors are statistical. There is a possible difficulty here, namely that sometimes a π^+ event could fit $pp \rightarrow pp\pi^+\pi^-$. This cannot be measured directly since we have no film without proton contamination, but it is probably small since in the pure proton film there were 119 unambiguous fits to $pp \rightarrow pp\pi^+\pi^-$ but no unambiguous fits to $\pi^+p \rightarrow \pi^+\pi^-p\pi^+$.

3. Difficulties in Cross-Section Determination

The following difficulties may lead to incorrect determination of the ratio of the number of elastic-scattering events to total events:

a) Events accepted as fits to an improper hypothesis
b) Events missed during scanning
c) Rejected events
d) Unresolved events.

We discuss now each of these difficulties in some detail.

a. Events accepted as fits to an improper hypothesis

The most likely confusion is between $\pi^+ p \to \pi^+ p$ and $\pi^+ p \to \pi^+ p \pi^0$. The most important selection criterion for separating these two reactions is identification of the proton track by ionization. Almost all elastic scattering events have small enough momentum transfer so that the proton is easily recognizable by ionization.

Elastic-scattering events misidentified as $\pi^+ p \pi^0$ usually produce a peak in the $\pi^+\pi^0$ mass spectrum near 400 MeV. We see no such peak, which indicates that the misidentification of events is small.

b. Events missed during scanning

(1) Correction for small-angle elastic scattering events

It is well-known that it is very difficult to find small-angle elastic-scattering events, and, due to the peripheral nature of the interaction, they are rather numerous. Since there was a large number of recoil protons in the bubble chamber most of which were unassociated with desired events, many scanners overlooked events with recoil protons of considerable length but with small angular deflection of the beam track. Only events with scattering angle, α, between incident and outgoing π^+ projected into the film plane greater than 3 deg and momentum transfer $-t > 0.05\ (\mathrm{GeV}/c)^2$ were used in the analysis. This cut removed events with very small momentum transfer and events where the scattering plane was nearly perpendicular to the film plane. The population in these regions was estimated by using an exponential extrapolation to $t = 0$ and by weighting events with $\alpha > 3$ deg with a weight determined by calculating for what fraction of the events the projected scattering angle at the given t would be greater than 3 deg provided the angular distribution between the film plane and scattering plane were uniform. The total number of elastic-scattering events estimated to be in various t regions at 3.56 and 3.67 GeV/c is given below:

$-t\ (\mathrm{GeV}/c)^2$	3.56 GeV/c	3.67 GeV/c
0.05-0.6	1918±63	3521±90
> 0.6	173.5±14	327±19

where the errors include the statistical errors with the appropriate corrections for weighting to remove the bias caused by the $\alpha > 3$ deg restriction and for proton contamination subtraction, but do not include the error in W.

Data for both momenta were combined and fit to the form e^{-bt} in the t region 0.05 - 0.6; b was found to be $6.85 \pm 0.20\ (\mathrm{GeV}/c)^{-2}$. If N_2 is the number of events from 0.05 to 0.6, N_1 the number of events from 0 to 0.05, N_3 the number > 0.6, and an exponential distribution e^{-bt} is assumed in the region 0.05 to 0.6,

$$N_1 = N_2 \frac{1-e^{-0.05b}}{e^{-0.05b} - e^{-0.6b}} .$$

Define:

$N^A_{e\pi}$ to be the number of accepted elastic-scattering events in the sample of relatively pure π^+ film,

N^A_{ep} to be the number of accepted elastic-scattering events in the sample of relatively pure proton film,

N^c_{eA} to be the total number of accepted elastic-scattering events after correction for small-angle scatters,

i.e., $N^c_{eA} = N_1 + N_2 + N_3$.

N_{XA} is the estimated number of events lost owing to difficulty of seeing small-angle elastic-scattering events:

$N_{XA} = N^c_{eA} - N^\pi_{eA} + W N^p_{eA}$.

Table XII gives values for N^π_{eA}, N^p_{eA}, W, N_{XA}, and $\Delta(N^c_{eA})$.

(2) Estimation of other effects of events not found during scanning

To estimate the scanning efficiency, about 10% of the film was scanned twice and the two scans compared. 5663 accepted events were found on both scans: 183 accepted events were found on scan 2 (but not scan 1) of which 73 were elastic-scattering events with projected angle less than 3 deg, and 212 accepted events were found on scan 1 (but not scan 2) of which 94 were elastic-scattering events with projected angle less than 3 deg. If it is assumed that all events are equally difficult to find, 98% of the events are found on a given scan, excluding elastic-

scattering events with projected angle less than 3 deg. For the remaining 2% of the events in the rescanned region it was found that the ratio of elastic-scattering events to total events was approximately the same as for accepted events, so no correction will be made. We assume a 2% contribution to the error on the elastic-scattering cross section from events missed on the original scan. This is equivalent to assuming that the fact that 2% is probably an underestimate of the number of events missed while scanning due to variation in degree of difficulty in finding various events is compensated by the fact that only the biases in the 2% missed cause an error in the elastic-scattering cross section.

C. Rejected events

There were two reasons for rejecting events that were biased

i) constraint dropped,

ii) track identification proved that event was really a reaction not included in the kinematic fitting program.

Reason i)—constraint dropped: If an elastic-scattering event dropped one, or in a few rare cases, two constraints, it was still accepted as a three- or two-constraint fit respectively. If, however, a one-constraint or missing-mass event dropped a constraint, it was classified as a zero-constraint reject. Therefore if the numbers of zero-constraint rejects N_z^π, N_z^p are added to the number of nonelastic accepted events, this difficulty is removed.

Reason ii)—track identification proved that event was really a reaction not included in the kinematic fitting program: In many cases fits which involved K^+ production were omitted from two-prong and four-prong event types; consequently, if ionization determination discovered a K^+, the event was rejected. N_w^π, N_w^p are the number of rejects of this type. If N_w^π, N_w^p are added to the number of nonelastic accepted events this difficulty is removed.

d. Unresolved events

Table XIII gives numbers of events in various categories of unresolved events. An event was unresolved if after three measurements it had been neither accepted nor rejected. There were two basic reasons for events falling in this category:

a) events which never passed geometric reconstruction,

b) events which passed geometric reconstruction but failed to make any of the fits listed in Table X.

Events unresolved for reason a) may be biased, and events unresolved for reason b) are certainly biased since it is much more likely that an elastic-scattering event will fail to achieve any fit than that a missing-mass event will fail to achieve any fit. In order to determine the number N_{ue}^π, N_{ue}^p of elastic scattering events and the number of events N_{uN}^π, N_{uN}^p which are not elastic scattering events among the unresolved events, all available measurements of unresolved events were examined. Table XIII gives the breakdown of the unresolved events into various categories. The small number of events which could not be classified as either elastic or inelastic fell into one of three groups:

i) event which should be rejected,

ii) there was insufficient measurement information to make a determination,

iii) it was difficult to make a decision on the basis of available information.

The numbers falling into each group are included in Table XIII.

To calculate N_{ue}^π, N_{ue}^p, N_{uN}^π, N_{uN}^p events in group i) were discarded, in group ii) divided into elastic and inelastic according to the ratios for accepted two-prong events and in group iii) were arbitrarily assumed to be one half elastics and one half inelastics. The resultant values for N_{ue}^π, N_{ue}^p, N_{uW}^π, and N_{uN}^p appear in Table XII.

The errors in N_{ue}^π, N_{ue}^p, N_{uN}^π, N_{uN}^p were assumed to have independent systematic and statistical contributions. A conservative estimate of the systematic error was made by setting it equal to one-half of the sum of the numbers of events in groups i), ii), and iii). The values of $\Delta(N_{ue}^\pi)$, $\Delta(N_{ue}^p)$, $\Delta(N_{uN}^\pi)$, $\Delta(N_{uN}^p)$ calculated in this manner appear in Table XII.

One more correction was made. N_{ue}^c events were added to the number of elastic-scattering events to correct for events missed while scanning which would have been unresolved if found. It was assumed that the percentage of events lost for this reason would be the same as for accepted events:

$$N_{ue}^c = \frac{N_{XA}}{N_{eA}^\pi - WN_{eA}^p} \left(N_{ue}^\pi - WN_{ue}^p\right).$$

This assumption was checked by comparing the momentum distributions of the recoil protons for accepted and unresolved elastic scattering events which showed very similar dips at small recoil momenta. Estimates of the error in N^c_{ue} appear in Table XII.

4. Results

The above considerations lead to the following formula for the elastic cross section σ_e:

$$\sigma_e = \sigma_{tot} \quad N^\pi_{eA} - WN^p_{eA} + N^\pi_{ue} - WN^p_{eu} + N_{XA} + \frac{N_{XA}}{N^\pi_{eA} - WN^p_{eA}} (N^\pi_{ue} - WN^p_{ue})$$

$$\div N^\pi_{tA} - WN^p_{tA} + N^\pi_z - WN^p_z + N^\pi_W - WN^p_W + N^\pi_{ue} - WN^p_{ue} + N^\pi_{uN} - WN^p_{uN} + N_{XA}$$

$$+ \frac{N_{XA}}{N^\pi_{eA} - WN^p_{eA}} \left(N^\pi_{ue} - WN^p_{ue}\right)$$

or

$$\sigma_e = \sigma_{tot} \frac{N^c_{eA} + N^\pi_{ue} - WN^p_{ue} + N^c_{ue}}{N^\pi_N - WN^p_N + N^c_{eA} + N^\pi_{ue} - WN^p_{ue} + N^\pi_{uN} - WN^p_{uN} + N^c_{ue}} .$$

Substituting in values from Table XII, σ_e = 6.93 mb at 3.56 GeV/c and 7.15 mb at 3.67 GeV/c.

5. Calculation of Errors

Assume the following independent contributions to the errors: a 2% error from scanning efficiency and independent contributions from $\Delta(N^c_{eA})$, $\Delta(N^\pi_{ue})$, $\Delta(N^p_{ue})$, $\Delta(N^c_{ue})$, $\Delta(N^\pi_N)$, $\Delta(N^p_N)$, $\Delta(N^\pi_{uN})$, $\Delta(N^p_{uN})$. The error in W makes a negligible contribution since the ratio of elastic-scattering events to total events is not much different for proton events from its value for π events. Substitution of numbers from Table XII leads to the following results with the total cross section taken as 28.15 mb:[17]

σ_e = 6.93 ± 0.24 mb at 3.56 GeV/c and 7.15 ± 0.21 mb at 3.67 GeV/c.

B. Determinations of Cross Sections for $\pi^+p \to \pi^+p\pi^+\pi^-$, $\pi^+p\pi^+\pi^-\pi^+\pi^-$

The same general principles apply as for cross-section determination $\pi^+p \to \pi^+p$. There are a considerable number of ambiguous events in the reaction $\pi^+p \to \pi^+p\pi^+\pi^-$. Only two types of ambiguities are frequent enough to be important here:

i) ambiguity as to which track is the proton,

ii) ambiguity between $\pi^+p \to p\pi^+\pi^+\pi^-$ and $pp \to pp\,\pi^+\pi^-$. Ambiguity 1 is not important since there is no confusion as to what the reaction actually was. Ambiguity ii) is corrected for by assigning all events of this type remaining after proton subtraction to $\pi^+p \to \pi^+p\pi^+\pi^-$.

The final difficulty was classification of unresolved events. It was assumed that the unresolved events were of two types.

a) No fit events with no missing neutrals. During the processing of SIOUX output, a record was made of all events which were apparently measured satisfactorily, achieved no fit, but seemed to have no missing neutral particles.

b) Measurement failure independent of reaction. Unresolved events of type a) were assumed to be all events of type π^+p, $\pi^+p\pi^+\pi^-$, or $\pi^+p\pi^+\pi^+\pi^-\pi^-$. Unresolved events of type b) were distributed among various reactions according to the numbers of accepted events. An error of 20% was assigned to this estimate. It was found to be consistent with the more careful estimate previously described for two-prong events.

Results: The cross section for $\pi^+p \to \pi^+p\pi^+\pi^-$ is 3.47 ± 0.12 at 3.65 GeV/c and 3.59 ± 0.14 at 3.55 GeV/c. The cross section for $\pi^+p \to \pi^+p\pi^+\pi^+\pi^-\pi^-$ is 0.22 ± 0.02 mb at 3.65 GeV/c and 0.20 ± 0.02 mb at 3.55 GeV/c.

C. Cross Sections for the Final States

$p\pi^+\pi^0$, $\pi^+\pi^+n$, $p\pi^+MM$, $\pi^+\pi^+MM$, $p\pi^+\pi^+\pi^-\pi^0$, $\pi^+\pi^+\pi^+\pi^-n$, $p\pi^+\pi^+\pi^-MM$, $\pi^+\pi^+\pi^+\pi^-MM$, $p\pi^+\pi^+\pi^+\pi^-\pi^-\pi^0$, $n\pi^+\pi^+\pi^+\pi^+\pi^-\pi^-$, $p\pi^+\pi^+\pi^+\pi^-\pi^-MM$, $\pi^+\pi^+\pi^+\pi^-\pi^-MM$

The biggest difficulty in measuring the cross sections for these final states is reliability in identification of the reaction. In particular, two difficulties arise:

i) Separation of final states containing a proton from those which do not (events ambiguous within the same constraint class)

ii) Contamination from events which should have been assigned to a different constraint class.

Events in final states which do not contain a proton are more likely to be ambiguous than in the final states which do, since if an event is peripheral to the proton, the slow proton will lead to an unambiguous identification as a final state which contains a proton, whereas a slow neutron does not help solve the identification problem. Thus we set the following as upper and lower limits on the distribution of the ambiguous events:

i) All ambiguous events do not contain an outgoing proton.

ii) The ambiguous events are divided between the two channels in the same proportion as the unambiguous events.

The cross section for each channel was determined from the number of unambiguous events in each channel plus a number of ambiguous events halfway between the two extremes. The error was estimated from two contributions

i) statistical error,

ii) half the difference between the two extremes.

Table XIV lists the cross sections for various final states.

IX. ELASTIC SCATTERING

A. Angular Distribution

The momentum transfer, t, distribution from 0.05 $(\mathrm{GeV}/c)^2$ to the kinematic maximum is shown in Fig. 21 and listed in Table XV in the form $d\sigma/dt$. The t region from 0.05 to 0.6 contains corrections for losses from scatters with α less than 3 deg. The region $t > 2.1$ contains no correction for proton beam contamination since $pp \rightarrow pp$ in not ambiguous with $\pi p \rightarrow \pi p$ in this angular region. The measured values of $d\sigma/dt$ as a function of $|t|$ are shown, for forward angles, in Fig. 22 and listed in Table XVI. A satisfactory fit of the data between $|t| = 0.05$ and $|t| = 0.6$ $(\mathrm{GeV}/c)^2$ can be made to the form

$$\frac{d\sigma}{dt} = \left(\frac{d\sigma}{dt}\right)_0 e^{Bt} .$$

The result is $(d\sigma/dt)_0 = 46.5 \pm 1.8$ mb/$(\mathrm{GeV}/c)^2$, $B = 6.85 \pm 0.20$ $(\mathrm{GeV}/c)^{-2}$. The ratio of real to imaginary part of the forward scattering amplitude, α, with 28.15 mb taken as the total π^+p cross section,[17] is

$$|\alpha| = 0.39 \pm 0.06 .$$

The $d\sigma/du$ distribution for events in the backward hemisphere is shown in Fig. 23.

X. THE REACTIONS $p\pi^+\pi^0$ AND $n\pi^+\pi^+$

For study of these final states, proton contamination was subtracted in the manner described in Section VII.E.1. When producing scatter plots for each event in set 1 (heavily contaminated with protons) on the scatter plot, the point in set 3 (low proton contamination) lying closest to the point in set 1 in question was deleted. Only the remaining points in set 3 were plotted.

A. General Features

The Dalitz plots for the final states $p\pi^+\pi^0$ and $n\pi^+\pi^+$ are shown in Fig. 24a and 24b respectively. In Fig. 24a there is clear evidence for ρ^+ and Δ^{++} production and a general increase of population at low $p\pi^0$ mass. Figure 25a, b, c, d, e are plots of $\Delta p\pi^{+2}$ vs. $m^2 p\pi^+$, $\Delta^2 p\pi^0$ vs. $m^2 p\pi^0$, $\Delta^2\pi^+\pi^0$ vs. $m^2\pi^+\pi^0$, $\Delta^2 n\pi^+$ vs. $m^2 n\pi^+$, $\Delta^2\pi^+\pi^+$ vs. $m^2\pi^+\pi^+$, respectively. The most striking features in these plots are concentrations of events at low momentum transfer in the Δ^{++} region in Fig. 25a, a broad enhancement at low $p\pi^0$ mass in Fig. 25b, in the ρ^+ region in Fig. 25c, and a broad enhancement at low $n\pi^+$ mass in Fig. 25d. All of these effects will be discussed in more detail.

B. The $\pi\Delta(1236)$ Final State

In Fig. 26 we show the $p\pi^+$ mass distribution for the channel $p\pi^+\pi^0$. A fit to the histogram for $m(p\pi^+) < 1.75$ GeV with a superposition of Δ^{++} and a phase space background weighted by an empirical weighting factor equal to $1 + b\,m_{p\pi^+}^2$ of 0.43 ± 0.03 mb. The overall $\pi\Delta$ cross section from π^+p interactions including all final channels is thus, using appropriate Clebach-Gordan coefficients, 0.72 ± 0.05 mb. The t_{π^0} distribution was determined by fitting $m(p\pi^+)$ spectra for a series of t_{π^0} regions to a superposition of Δ^{++} and phase space. The Breit-Wigner for the Δ^{++} had the same form as used for $K^+p \to \Delta^{++}K^0$ (Section V.A). The fitted amount of Δ^{++} production for each t_{π^0} region was assumed to represent the amount of Δ^{++} production in that t_{π^0} region. For $t_{\pi^0} < 0.4$ GeV^2 only the backward region of $\cos\alpha$ was used and the results multiplied by 2 in order to reduce the background from processes having preferentially low momentum transfer to the proton, notably ρ^+ production. The resultant $d\sigma/dt$ distribution is shown in Fig. 27. There is a striking dip near $t = -0.5$ (GeV/c)^2. As described in the Regge pole description with exchange of the ρ trajectory the helicity

flip amplitudes for $\pi^+p \to \pi^0\Delta^{++}$ go as

$$g(\alpha)\, F(s-u, \alpha)\beta(t)\, \frac{1-e^{-i\pi\alpha}}{\Gamma(\alpha+1)\sin\pi\alpha},$$

where $g(\alpha) \to 0$ as $\alpha \to 0$.[18-20] For a ρ trajectory of $\alpha(t) = 0.5 + t$, a zero is expected at -0.5. Since the spin density matrix elements indicate a large spin-flip contribution, these arguments lead to expectation of a dip near $t = -0.5$, which is in fact observed. The spin density matrix elements, shown in Fig. 28, were determined with only a mass band selection $[1.12 \le m_{p\pi^+} \le 1.32$ GeV$]$, but for $t_{\pi^0} < 0.4$ (GeV/c)^2 only the backward $\cos\alpha$ region was used.

C. Diffractive Dissociation of the Proton into $n\pi^+$ and $p\pi^0$

In Fig. 25b and 25d there is a large excess of events at small momentum transfer and at fairly low mass. The enhancement certainly contains some Δ^+ production, but it is too broad and contains too many events to be explained entirely by Δ^+ production. The combination $\sigma_{1/2} = \sigma_{p\pi^0} + \sigma_{n\pi^+} - (2/3)\sigma_{p\pi^+}$ isolates the isospin-1/2 nucleon pion component by subtracting the isospin-3/2 component and the interference between isospin 3/2 and 1/2. $\sigma_{n\pi^+}$ in the region in question is less than a factor of 2 larger than $\sigma_{p\pi^0}$, which indicates appreciable interference between the isospin 1/2 and 3/2 amplitudes, since the isospin-3/2 amplitude is quite small except in the region of the Δ^{++}. Taking the states $p\pi^+\pi^0$, $n\pi^+\pi^+$ as $N\pi_1\pi_2$, Fig. 29 is an $N\pi_1$ mass spectrum of the isospin-1/2 component, using the above formula. For $\sigma_{p\pi^+}$, $\pi_1 = \pi^+$; for $\sigma_{p\pi^0}$, $\pi_1 = \pi^0$; for $\sigma_{n\pi^+}$, both π^+'s are tried as π_1. The events plotted in Fig. 29 have the following restrictions:

i) The cosine of the angle between N and π_2 in the $N\pi_1$ center of mass is limited to the range -0.5 to +1 to eliminate effects of ρ^+ production.

ii) The momentum transfer to the $N\pi_1$ combination is restricted to 0 - 0.4 (GeV/c)^2.

The shaded events have momentum transfer less than 0.1 (GeV/c)^2.

Figure 30 presents the momentum-transfer distribution to the $N\pi_1$ combination for: a) $m_{N\pi_1} < 1.8$ GeV, b) $m_{N\pi_1} < 1.3$ GeV, c) $m_{N\pi_1}$ from 1.3 to 1.5 GeV, d) $m_{N\pi_1}$ from 1.5 to 1.8 GeV with condition i) also satisfied.

Figure 29 presents evidence that there is considerable peaking in the isospin-1/2 component of the N_{π_1} mass spectrum at masses considerably lower than the lowest-lying N^* resonance according to phase shift analysis as pointed out by the Anglo-German collaboration.[21] Figure 30b), c), d) shows that the momentum-transfer distribution is more peaked for the smaller-mass part of the diffractive enhancement than for the larger-mass part. This effect was reported by the Anglo-German collaboration.[21]

D. ρ^+ Production

The study of ρ^+ production is complicated by background problems, including interference. The most serious problems are caused by Δ^{++} production and diffraction dissociation. Figure 31 a-j shows plots of t'_p, momentum transfer to the outgoing proton minus the kinematical minimum, vs. $m_{\pi^+\pi^0}$ for various regions of $\cos\alpha$, the cosine of the angle between the incident and outgoing π^+ in the π-π center of mass. The plots show considerable ρ^+ production for all values of $\cos\alpha$. Of special interest is the relatively large amount of background under the ρ^+ near $\cos\alpha = -1$ and $+1$ at small t'_p which is connected with the Δ^{++} and diffractive dissociation. Also noteworthy is the relatively large signal-to-noise ratio for ρ^+ production at small t'_p near $\cos\alpha = 0$. $\cos\alpha$ is the cosine of the angle between incident and outgoing π^+ in the π-π center of mass. ϕ is the Treiman-Yang angle in the π-π center of mass.

1. Determination of the Mass and Width of the ρ^+

The form of the Breit-Wigner used was

$$B_w = \frac{\Gamma_p^*}{(m^2-m_0^2)^2 + \Gamma^2 m_0^2}, \qquad (1)$$

where

$$\Gamma = \Gamma_0 \frac{q^3}{q_0^3} \frac{\left(1+\frac{q_0^2}{m_\pi^2}\right)}{1+\frac{q^2}{m_\pi^2}},$$

$$p^* = \sqrt{\left(\frac{E_{c.m.}^2 + M_p^2 - m^2}{2E_{c.m.}}\right)^2 - m_p^2},$$

p^* is the momentum of the outgoing proton in the overall center of mass,

$$q = \sqrt{\frac{m^2 - 4m_\pi^2}{4}},$$

$$q_0 \sqrt{\frac{m_0^2 - 4m_\pi^2}{4}},$$

q is the momentum of an outgoing π in the π-π center of mass,
m is the effective mass of the π-π system,
m_π is the mass of a π,
m_p is the mass of a proton,
$E_{c.m.}$ is the total center of mass energy,
m_0, Γ_0 were left as free parameters.

The sample of data selected was $t_p < 0.5\ (\mathrm{GeV}/c)^2$, $|\cos\alpha| < 0.5$ since this sample had a good signal-to-noise ratio. The background was parametrized as

$$\sum_{k=0}^{C} A_k m^k \times PS, \qquad (2)$$

where PS stands for phase space (including effect of t_p cut), A_k's were arbitrary coefficients, and C is a cutoff value. Fits were tried for various values of cutoff value C.

The π-π mass spectrum fit is shown in Fig. 32. The curve shown was obtained with C = 2. The χ^2 was 28 with 24 bins; the fitting region was 0.28 - 1.6 GeV. The results of the fit were $m_0 = 765 \pm 8$, $\Gamma_0 = 170 \pm 30$ MeV, where the errors come primarily from an estimate of uncertainty in the shape of the background obtained by comparing the results for various cutoff values C. The resolution was checked and the approximate formulas of Coyne et al.[22] showed that it was good enough to have negligible effect on the width measurement.

2. ρ^+ - Diffraction Interference

a. Evidence for the Effect

Figure 33 is a plot of $\cos\alpha$ vs. m for $t_p < 0.5\ (\mathrm{GeV}/c)^2$. There appears to be a significant upward shift of the ρ^+ peak near $\cos = +1$. This shift was made quantitative by the procedure described below.

The data was divided into ten separate regions of $\cos\alpha$ each of width 0.2. Each region was fit by using the Breit-Wigner of Eq. (1) and the background of Eq. (2). Γ_0 was fixed at 170 MeV, but m_0 was left free. In all cases reasonably good fits to the π-π mass spectra were obtained from threshold to a region considerably above the ρ^+. Figure 34 shows the results of the fitted values of m_0 as a function of $\cos\alpha$. There is indeed a large (~ 50 MeV) upward mass shift near $\cos\alpha = +1$.

b. Fit to the Region $\cos\alpha > 0$

An attempt was made to fit the π-π mass spectra for the five separate $\cos\alpha$ regions each of width 0.2 for $\cos\alpha > 0$ with $t_p < 0.5\ (\mathrm{GeV}/c)^2$ with completely coherent ρ^+ and diffraction amplitudes. The ρ^+ amplitude, T_{ρ^+}, was parametrized by

$$T_{\rho^+} = N_R \frac{\sqrt{\Gamma p^*}}{(m^2 - m_0^2) - i\, m_0\Gamma} R(\alpha,\phi) . \qquad (3)$$

N_R is a normalization factor, and $R(\alpha, \phi)$ describes the decay of the ρ and is taken to be

$$R(\alpha,\phi) = \sqrt{\frac{3}{4\pi}}\ [a \cos\alpha + b \sin\alpha e^{i\phi} + b \sin\alpha^{-i\phi}], \qquad (4)$$

where $a = \sqrt{\rho_{00}}$.

The diffraction amplitude was assumed to be

$$T_D = N_D \sqrt{mpq}\ e^{-\gamma t_{\pi^+}/2}\ e^{-i\delta}, \qquad (5)$$

where $p = \dfrac{(E_0^2 - m^2 - mp^2) - 4mp^2m^2}{4m^2}$ = momentum of outgoing proton in π-π center of mass,

$\sqrt{mpq}$ leads to π-π phase space upon squaring,

γ is the slope of the exponential diffractive momentum transfer dependence,

E_0 is the total energy,

N_D is a normalization factor,

δ is an arbitrary phase factor.

It should be pointed out that this amplitude is meant to describe approximately the t_{π^+} characteristics of the experimental data, but is not sensitive to the actual $m(p\pi^0)$ distribution of the experimental data. This amplitude, nominally a "diffractive" amplitude, contains a substantial contribution from $\Delta^+ \to p\pi^0$, but is dominated by the isospin-1/2 contribution. Diffraction and Δ^+ production have similar t_{π^+} distributions.

Closely connected with the lack of consideration of the experimental $m_{p\pi}$ distribution, T_D is independent of ϕ which causes all terms from (4) involving $\sin\alpha$ to drop out upon integration with respect to ϕ except a term proportional to $\rho_{11} \sin^2\alpha$. γ was estimated empirically to be 5.5 $(\mathrm{GeV}/c)^{-2}$ from Fig. 30a. t_{π^+} was expressed in terms of m and $\cos\alpha$ by using the relation

$$t_{\pi^+} = A - B \cos\alpha,$$

where

$$A = 2\left(\frac{t_p + m_{\pi^2} + m^2}{2m}\right)\left(\frac{m^2 + m_{\pi^+}^2 - m_{\pi^0}^2}{2m}\right) - 2m_\pi^2 , \qquad (6)$$

$$B = 2\sqrt{\left(\frac{t_p + m_\pi^2 + m^2}{2m}\right) - m_{\pi^+}^2} \times \sqrt{\left(\frac{m^2 + m_{\pi^+}^2 - m_{\pi^0}^2}{2m}\right)^2 - m_\pi^2} ,$$

t_p was set to 0.2 $(\mathrm{GeV}/c)^2$.

$$T = T_{\rho^+} + T_D,$$

$$\text{Rate} = |T|^2 .$$

Before integration over $\cos\alpha$,

$$|T|^2 = \frac{N_R^2 \Gamma p^*}{[(m^2 - m_0^2)^2 + m_0^2\Gamma^2]^2} (\rho_{00} \cos^2\alpha + \rho_{11} \sin^2\alpha)$$

$$(m^2 - m_0^2) + m_0^2\Gamma^2) + N_D^2 mpq\, B e^{-\gamma A}\ e^{\gamma B \cos\alpha}$$

$$+ \frac{2 N_R \sqrt{\Gamma p^*}}{(m^2 - m_0^2)^2 + m_0^2\Gamma^2} (\sqrt{\rho_{00}} \cos\alpha) \sqrt{N_D^2 mpq\, B e^{-\gamma A}}$$

$$\times\ e^{\gamma B \cos\alpha/2} [\cos\delta\, (m^2 - m_0^2) + \sin\delta\, m_0\Gamma).$$

After integrating over $\cos\alpha$ from X_L to X_U, where X_L and X_U are the lower and upper limits on $\cos\alpha$,

$$|T|^2 = \frac{N_R^2\,\Gamma p^*}{[(m^2 - m_0^2)^2 + m_0^2\Gamma^2]^2}\left[\frac{\rho_{00}}{3}(X_U^3 - X_L^3)\right.$$

$$\left. + \rho_{11}\left(X_U - X_L - \frac{1}{3}X_U^3 + \frac{1}{3}X_L^3\right)\right]\left[(m^2 - m_0^2)^2 + m_0^2)^2 + m_0^2\Gamma^2\right]$$

$$+ N_D^2\, mpq\, Be^{-\gamma A}\,\frac{1}{\gamma B}\left[e^{\gamma BX_0} - e^{\gamma BX_L}\right]$$

$$+ \frac{2N_R\sqrt{\Gamma}\,*\,\sqrt{\rho_{00}}}{(m^2 - m_0^2)^2 + m_0^2\Gamma^2}\sqrt{N_D^2\, mpq\, Be^{-\gamma A}}$$

$$\times\left[\cos\delta\,(m^2 - m_0^2) + \sin\delta\, m_0\Gamma\right] I,$$

where

$$I = \frac{2}{\gamma B}\left(X_U e(\gamma BX_U/2) - X_L\, e(\gamma BX_L/2) - \frac{2}{\gamma B}\, e(\gamma BX_U/2)\right.$$

$$\left. + \frac{2}{\gamma B}\, e(\gamma BX_L/2)\right).$$

Calculation of N_R, ρ_{00}, ρ_{11}: Fits were made to the π-π mass spectra for $t_p < 0.5\ (\mathrm{GeV}/c)^2$ for $\cos\alpha$ regions -1-0.6 and -0.6+0.6, using the ρ^+ form in Eq. (1) and the background of Eq. (2). m_0 and Γ_0 were fixed at 765 MeV and 170 MeV respectively. The results of the fit were: $N_R = 3180$, $\rho_{00} = 0.46$, $\rho_{11} = 0.27$. The region -1 to -0.6 has a large overlap with Δ^{++} production. This estimate of ρ_{00} ignores interference between Δ^{++} and ρ^+ production. As pointed out in Section X.D.5., this interference effect appears to be quite small.

Five separate mass spectra—Fig. 35a-e with $\cos\alpha$ 0.8-1, 0.6-0.8, 0.4-0.6, 0.2-0.4 and 0-0.2 respectively—were fit simultaneously by varying the value of δ. For each value of δ, N_D was calculated such as to make the sum of all events in the fitting regions of all five spectra equal to the total number predicted. δ was found to be 10 ± 6 deg where the error is statistical. A χ^2 of 61 was obtained with 52 bins. The fits are shown as curves on Fig. 35 a-e. It is remarkable that such a simple amplitude with complete coherence should fit the data so well over such a large range.

It should be pointed out that ρ^+ production interfering with a constant π-π S-wave background cannot reproduce the observed features of the data. There is present, in Fig. 34, a substantial upward mass shift of the ρ^+ near $\cos\alpha = 1$, but no evidence for a downward shift near $\cos\alpha = -1$. A slowly varying S-wave interference which produces an upward shift near $\cos\alpha = +1$ also produces a downward shift near $\cos\alpha = -1$.

A calculation was made to see how large a mass shift could be obtained from such a ρ^+ - S wave interference. The final state $\pi^+\pi^+n$ was used to obtain an upper limit on a possible T = 2 π-π S-wave. From the number of events with $-t_n < 0.5\ (\mathrm{GeV}/c)^2$ and $|\cos\alpha| < 0.5$, the upper limit (obtained by assuming all events in this region represented π-π S-wave) for the S-wave intensity is 8 events/0.02 GeV. Clebsch-Gordan coefficients then yield an upper limit of 2 events/0.02 GeV for the $p\pi^+\pi^0$ final state.

The S-wave amplitude was thus written as $T_s = \sqrt{2}\,e^{-i\delta}$, with δ an arbitrary parameter. The total amplitude was then written as $T = T_{\rho^+} + T_S$, where T_{ρ^+} is the amplitude for the ρ^+ used in the ρ^+-diffraction interference calculation. The intensity was calculated as $|T|^2$. The largest mass shift obtained for any value of δ was 15 MeV, a shift much smaller than observed experimentally. Furthermore, since ρ^+-diffraction interference has a strong effect on quantities such as the forward-backward asymmetry of the ρ^+ decay, attempts to measure π-π S-wave should use extreme caution to insure that all effects of ρ^+- diffraction interference have been properly taken into account.

3. Momentum Transfer Dependence of ρ^+ Production

In order to separate ρ^+ production from background, the following procedure was adopted. The data were divided into several regions

of t'_p. For each region the π-π mass spectrum was plotted and fit with a ρ^+ intensity of form (1) and a background intensity of form (2). m_0 was set to 0.765 GeV, Γ_0 to 0.17 GeV. Fits were tried with c = 0, 1,2. The basic assumption underlying this method is that the ρ^+ production does not interfere with background. It has already been shown that the ρ^+ production does interfere with diffraction, so for the t'_p region $t'_p < 0.6\ (\mathrm{GeV}/c)^2$ only events with $\cos\alpha < 0$ were used, and it was assumed that the amounts of ρ^+ production with $\cos\alpha < 0$ and $\cos\alpha > 0$ are equal.

This method of fitting works much better for a t'_p distribution than for a t_p distribution, because t'_p cuts distort the background much less than t_p cuts. It is important in this fitting procedure that the background have a much slower π-π mass variation than the ρ^+. The reflection of the Δ^{++} production satisfies this condition even with various t' cuts, as can be seen in Fig. 31 a-b. This is no longer true if a t_p cut is used instead.

Figure 36 shows $d\sigma/dt$ for ρ^+ production. The ordinates come from converting the fitted amounts of ρ^+ production in each t'_p region to cross sections. The total cross section for $\pi^+p \to \rho^+p$ was determined to be 0.79 ± 0.07 mb from a fit according to the procedure described above to a $\pi^+\pi^0$ mass spectrum with no t' cut. There is some evidence for a dip at $t'_p \approx 0.5\ (\mathrm{GeV}/c)^2$. There appears to be some ρ^+ production at all values of t'_p. Figure 37 a and b show the $\pi^+\pi^0$ mass spectra for t'_p 2-4 and $> 4\ (\mathrm{GeV}/c)^2$ respectively. The dashed curves are the fitted background levels. The solid curves are the fitted amounts of ρ^+ + background. The difference is the fitted amount of ρ^+ production.

4. Spin Density Matrix Elements

A very similar procedure was used to determine the spin density matrix elements of ρ^+ decay as was used in the determination of $d\sigma/dt$. For each spin density matrix element the data were divided into two appropriate angular regions and the π-π mass spectrum for each region was fit to ρ^+ + background as described in the preceding section. In certain cases the diffraction region was eliminated. Table XVII lists the angular regions used in each fit. The spin density matrix element in question was calculated from the fitted number of ρ^+'s in each region. To determine the spin density matrix elements

as a function of t'_p, the data were further subdivided into various t'_p regions and the same process was repeated.

The results for the spin density matrix elements integrated over all t' were: Jackson frame: ρ_{00}, 0.33 ± 0.09; ρ_{1-1}, 0.15 ± 0.10; $\mathrm{Re}\rho_{10}$ -0.04 ± 0.06; helicity frame: ρ_{00}, 0.33 ± 0.08; ρ_{1-1}, 0.18 ± 0.06; $\mathrm{Re}\rho_{10}$, 0.08 ± 0.05. The corresponding results obtained with identification of the ρ^+ as $m_{\pi\pi}$ 660-860 were: Jackson frame: ρ_{00} 0.37 ± 0.04; ρ_{1-1}, 0.05 ± 0.04; $\mathrm{Re}\rho_{10}$, -0.08 ± 0.03, helicity frame: ρ_{00}, 0.45 ± 0.04 ρ_{1-1}, 0.13 ± 0.04; $\mathrm{Re}\rho_{10}$, 0.11 ± 0.03. The primary effect of the background correction was to correct for Δ^{++} production and a phase-space like background. The Δ^{++} production is the dominant effect. In the Jackson frame its removal decreases ρ_{00}, increases ρ_{1-1} and decreases $\mathrm{Re}\rho_{10}$. (The diffraction region was not used in this determination.)

Figure 38 a, b and 39 a, b present the spin density matrix elements in the Jackson and helicity frames respectively averaged over various t'_p regions. The results were obtained by the fitting procedure described above. The difference between Fig. 28 a and b and between Fig. 39 a and b is the size of the t'_p regions selected. The dashed crosses in Fig. 38 a and Fig. 39 a show the results obtained if the ρ^+ is defined by mass band selection only ($0.66 \le m \le 0.86$ GeV). The influence of the Δ^{++} is particularly strong in Fig. 38a in the region t'_p from 0.08 to 0.5, where its removal causes a decrease in ρ_{00}, an increase in ρ_{1-1}, and a decrease in $\mathrm{Re}\rho_{10}$.

5. Δ^{++}-ρ^+ Interference Model

We have used the empirical interference model of Bland et al.:[23]

$$\frac{d^2\sigma}{dM_K{}^2\pi dM^2{}_{N\pi}} = a + bI_\rho + cI_\Delta + 2d\,(bcI_\rho I_\Delta)^{1/2}$$

$$\cos(\phi_\Delta - \phi_\rho + \phi_0)$$

where

$$I_\rho = BW_\rho\,(1 - A_{\pi\pi}\cos^2\lambda_{\pi\pi}),$$

$$I_\Delta = BW_\Delta\,(1 + A_{N\pi}\cos^2\lambda_{N\pi}),$$

$$BW = \frac{1}{\sqrt{\pi}} \frac{\Gamma(p_0/p)m_0}{(m^2 - m_0^2)^2 + (\Gamma m_0)^2},$$

$$\Gamma = \Gamma_0 \left(\frac{p^2}{p^2 + m_\pi^2} \Big/ \frac{p_0^2}{p_0^2 + m_\pi^2} \right) \left(\frac{p}{p_0} \right).$$

ϕ_Δ, ϕ_ρ are the phases of the Breit-Wigner amplitudes of the Δ and and ρ respectively which are proportional to

$$\frac{1}{(m_0^2 - m^2) - m_0 \frac{\Gamma_q}{q_0} i}.$$

$A_{\pi\pi}$, $A_{N\pi}$ are empirical constants added to allow for the decay distribution of the ρ^+ and Δ^{++} respectively. d is a coherence factor which ranges from 0 to 1. If d is zero, the model reduces to an incoherent superposition of ρ^+ and Δ^{++}.

The model was applied to fitting various Dalitz plots in the region far removed from diffractive dissociation. Four Dalitz plots were fit: no t'_p cut, $t'_p = 0\text{-}0.5$ $(GeV/c)^2$, $t'_p = 0\text{-}0.08$ $(GeV/c)^2$, $t'_p = 0.08\text{-}0.5$ $(GeV/c)^2$. Figure 40 a, b, c shows Dalitz plots with no t'_p cut, $t'_p = 0\text{-}0.08$, $t'_p = .08 - 0.5$ respectively. It should be noted in particular for $t'_p < 0.08$ that there appears to be little production of anything besides ρ^+, Δ^{++}, and diffraction.

$A_{N\pi}$ was determined from the population of the Δ^{++} band in the half of the Dalitz plot which does not include the overlap region with the ρ^+. This assumes that the t'_p cuts do not introduce asymmetries in the Δ^{++} decay, which is consistent with Fig. 31 a and b.

A noncoherent fit was tried by setting d to 0 and varying a, b, c, and $A_{\pi\pi}$. A fit with interference was also tried by varying d and ϕ_0 as well.

The results of the fits are tabulated in Table XVIII. There is some very weak evidence of interference though clearly more data are needed to establish the effect. Within the context of this model even if there is interference, the ρ_{00} spin density matrix element in the helicity frame is not appreciably affected.

6. Difficulties of Determination of π-π Phase Shifts

In Fig. 36a and b there is evidence of an increase in ρ_{00} at very small values of t'_p. The increase is rapid enough so that only $t'_p <\sim 0.04$ $(GeV/c)^2$ is useful for extrapolation. However, in the t'_p region 0 - 0.08 $(GeV/c)^2$ there are a number of difficulties with the π-exchange model:

i) $\rho^+ - \Delta^{++}$ interference may cause the rise in ρ_{00}. This would require a different interference model than presented in the preceding section. If this is the case, extrapolation is not valid.

ii) ρ_{00} is not consistent with 1 in this region. It is rising rapidly, but is still far from 1 so that a considerable extrapolation is necessary.

iii) Δ^{++} and diffraction are still important in this region. Evidence for ii) can be seen in Fig. 31 d-g. Evidence for iii) can be seen in Fig. 38b where in addition to ρ^+ production the Dalitz plot appears dominated by Δ^{++} production and diffraction even for $t'_p < 0.08$ $(GeV/c)^2$. It should be pointed out that Δ^{++} production introduces significant partial waves up to $\ell \approx 9$ into the cos λ distribution of the π-π system due to the Breit-Wigner mass dependence. By the Wigner-Eckhart theorem these higher partial-wave contributions must be present in the Jackson frame as well.

Present data do not permit a check on an extrapolation procedure to see whether or not it extrapolates out correctly the higher partial-wave background.

E. $N^*(1688)$

Figures 41 and 42 show the $n\pi^+$ and $p\pi^0$ mass spectra for the final states $n\pi^+\pi^+$ and $p\pi^+\pi^0$. The shaded events are t_{π^+} greater than 0.5 $(GeV/c)^2$. There is evidence for $N^*(1688)$ formation at large momentum transfer. This effect can also be seen in Fig. 25b and d.

F. Other Peaks in Mass Spectra

1. $\pi^+\pi^+$ Spectrum

Figure 43 shows the $\pi^+\pi^+$ mass spectrum for events with $t_n < 0.5$ $(GeV/c)^2$. There is an apparent excess of events near 730 MeV. Further investigation of this region shows that there are several possible explanations for the effect and that it is difficult to determine the relative contributions of each possibility.

Since the excess of events occurs in a mass spectrum composed of two positively charged particles, the resonance most likely to reflect into this spectrum is the Δ^{++}. In order for this to happen, one of the particles which has been called a π^+ must be a proton. During the process of selection of events, a track which had momentum less than 1.45 GeV/c could be identified as a proton or π^+ by ionization, but for tracks faster than this cutoff value the proton mass hypothesis could not be distinguished from the π^+ mass hypothesis by ionization. The effective masses of the two charged particles were calculated by assuming that each track was a proton and the other track a π^+. Significant Δ^{++} production was found only for the case of events which had one and only one track with momentum greater than 1.45 GeV/c, with the faster track being the proton.

Figure 44 shows the correlation between the $p\pi^+$ mass calculated by assuming the faster track is a proton for events with one and only one track with momentum greater than 1.45 GeV/c, events with unique possibility of misidentification, and the $\pi^+\pi^+$ mass for a) events in set 1 of Section VII. E. 1—beam highly contaminated with protons—and b) events in set 3 of Section VII.E.1—low proton contamination in beam. Figure 44 shows that the $\pi^+\pi^+$ event excess is correlated with Δ^{++} production, and Fig. 44a shows that the proton contamination in the beam leads to a large amount of Δ^{++} production which is confused with the final state $\pi^+\pi^+n$. Figure 45 is a plot of the $p\pi^+$ spectrum for events with unique possibility of misidentification. For this figure proton subtraction has already been made as usual. There is some Δ^{++} production, but also a large number of events in the Δ^{++} region which are not Δ^{++}. In order to determine the source of the Δ^{++} production, Fig. 46 shows the missing-mass spectrum for events in Fig. 45 having $p\pi^+$ mass 1.14 - 1.3 GeV based on the following mass assumptions:

i) $\pi^+p \to \pi^+\pi^+$ MM,

ii) $\pi^+p \to \pi^+p$ MM,

iii) $pp \to pp$ MM.

All events used in this study were accepted as $\pi^+p \to \pi^+\pi^+n$. Unfortunately Fig. 46 contributes little information. All the missing-mass spectra contain peaks near the neutron mass which is basically a kinematic effect due to the requirement of a kinematic fit to

$\pi^+p \to \pi^+\pi^+n$. Figure 46b eliminates the reaction $\pi^+p \to \Delta^{++}\pi^0$ as a possible source of the Δ^{++} production. The neutron peaks in Fig. 46 can have contributions from three sources:

i) $\pi^+p \to \pi^+\pi^+n$, where the calculated "p" π^+ mass happens to lie in the Δ^{++} region,

ii) $\pi^+p \to \Delta^{++}$ MM, where the proton is too fast to be identified by ionization and the missing mass happens to lie near the neutron mass,

iii) $pp \to \Delta^{++}n$, which has not been properly accounted for by the proton subtraction.

If possibility ii) contributes, a depletion of events would be expected in the Δ^{++} region and missing-mass region near the neutron mass for events which have a fast proton. Figure 47 is a scatter plot of the $p\pi^+$ mass vs. the missing mass for the final state $p\pi^+$MM for a) $t_p < 1.5\ (\mathrm{GeV}/c)^2$ and b) $t_p > 1.5\ (\mathrm{GeV}/c)^2$. Figure 47b is consistent with a depletion of events in the region expected. There is some evidence of Δ^{++} production in this plot. The much larger general population in this plot at high missing-mass values is probably due to contamination from the final state $\pi^+\pi^+$MM. Summarizing, the structure in Fig. 43 can have contributions from:

i) $\pi^+p \to \Delta^{++}$MM,

ii) $pp \to \Delta^{++}n$ with improper subtraction,

iii) statistical fluctuations,

iv) structure in the $\pi^+\pi^+$ system.

We conclude that it is difficult to separate these possible interpretations.

It would be interesting to obtain information on the behavior of the diffractive dissociation process in the low π-π mass region from the final state $\pi^+\pi^+n$ where there is no ρ^+ production, but the four possible background contributions listed above make such an analysis extremely difficul

2. <u>$\pi^+\pi^0$ Spectrum</u>

Figure 48 shows the $\pi^+\pi^0$ mass spectrum for t_p from 2.2 to 4.4 $(\mathrm{GeV}/c)^2$. There is some evidence for a fairly broad enhancement near 1.37 GeV. In this momentum-transfer region the proton cannot be distinguished from a π^+. In fact there is considerable ambiguity between $\pi^+p\pi^0$ and $\pi^+\pi^+n$. Figure 49 is a scatter plot of $\pi^+\pi^0$ mass vs. $n\pi^+$ mass for events ambiguous between $\pi^+\pi^+n$ and only one of the two possible $\pi^+p\pi^0$ hypotheses and with t_p from 2.2 to 4.4. For the

final state $\pi^+\pi^+n$, that π^+ is combined with the neutron to form the $n\pi^+$ mass that was combined with the π^0 for the $p\pi^+\pi^0$ hypothesis to form the $\pi^+\pi^0$ mass. Figure 49 shows production of $N^*(1688)$ in the $n\pi^+$ combination and, further, a very strong correlation between the $N^*(1688)$ and the 1.37-GeV enhancement. We conclude that the 1.37-GeV enhancement is a reflection of $N^*(1688)$ production.

XI. MISSING-MASS EVENTS

A. The Final State π^+pMM

Figure 50 shows the missing-mass spectrum in this final state. There is clear evidence of η production, evidence of ω production, and some evidence for $\eta'(960)$ production. Figure 51 shows the $p\pi^+$ mass spectrum; there is a large amount of $\Delta^{++}(1238)$ production. A comparison of Fig. 47a and 47b shows that it is produced preferentially at small momentum transfer; Fig. 47a further shows clustering in the Δ^{++} band at the masses of the η and ω. The cluster in the Δ^{++} band near 320 MeV is highly suspicious as will be shown later on. Figure 52a and 52b shows the missing-mass spectra for events with $p\pi^+$ mass of 1.14 - 1.3 GeV for t_{MM} arbitrary and less than 0.6 $(GeV/c)^2$ respectively. Figure 52 shows evidence for $\Delta^{++}\eta$ and $\Delta^{++}\omega$ production, which is especially strong at small t_{MM}. The peak near 330 MeV in Fig. 52 is highly dubious since it is a small remnant of a large proton subtraction, as can be seen by contrasting Fig. 52b and Fig. 53. (The latter is the same as Fig. 52b except that no proton subtraction was done.) The source of the peak is $pp \to \Delta^{++}n$, where the missing mass is shifted from the neutron mass to ~ 300 MeV by changing from $pp \to \pi^+pMM$ to $\pi^+p \to \pi^+p$ MM.

Figure 54 shows the π^+MM spectrum for a) all t_p and b) $t_p < 1.2$ GeV. There is evidence of A_2 production, especially at small t_p.

B. The Final State $\pi^+\pi^+MM$

Figure 55 is the missing-mass spectrum for this final state. The spectrum shows little structure, but there is some evidence for $\Delta^0(1238)$ production.

ACKNOWLEDGMENTS

First of all I wish to express my sincere gratitude to Professor George H. Trilling, teacher and research director, whose guidance and encouragement from the initial stimulus of an excellent course in nuclear physics and then constantly throughout many years to a final careful reading of this manuscript have provided the inspiration for the completion of this project. I wish to thank Professor Gerson Goldhaber and the late Dr. Sulamith Goldhaber for their support throughout many years.

I wish particularly to thank my colleagues, Dr. Don Coyne and Dr. Ralph Butler, for advice, assistance, many discussions, support, encouragement, and endurance throughout the course of many years experimental work.

I wish to thank the United States government for its interest in this form of basic research, expressed by supplying the considerable funds for this project through the Atomic Energy Commission.

Special thanks are due my colleague, Dr. Chumin Fu, for collaboration on the K^+ experiment and for many discussions of the $\pi^+ p \pi^0$ final state. I wish to thank Dr. Roger Bland, Dr. Benjamin Shen, and Dr. Allan Hirata for much assistance in orientation to the Trilling-Goldhaber group in the early days.

I wish to express my sincere gratitude to the support staff of the Trilling-Goldhaber group: the experiment coordination department under Frank Sieh and Willie Lacy, the computing staff under Emmett Burns, and to the scanning and measuring staff for their conscientious and devoted perservance which overcame the almost insurmountable amount of tedious picture analysis that provided the data upon which this study is based and for enduring a graduate student who was most eager to obtain data.

Thanks are due the accelerator, bubble chamber, and computing center staffs without whose efforts this work would have been impossible. I am especially grateful to Howard White and the data handling group for their indispensible efforts in processing measurements with the FSD. I also wish to thank Tamara and Paul Elischer for assistance with magnetic tape and printed computer output.

Finally I wish to thank my mother for typing the manuscript and drawing the figures and Charles Pezzotti for editing the manuscript and figures.

REFERENCES

1. Ian Skillicorn, and Medford S. Webster, Status Report on a High Energy Separated Beam for the 80" Chamber, Brookhaven Internal Report H-10, March 21, 1962.

2. D. C. Rahm, Tuning and Running Separated Beam #3, Brookhaven Internal Report H-17, July 15, 1965.

3. D. V. Bugg et al. [Phys. Rev. 168, 1466 (1968)] give $\sigma_t = 17.25 \pm 0.12$ mb at 2.47 GeV/c, whereas W. Galbraith et al. [Phys. Rev. 138, B913 (1965)] find an essentially constant value of σ_t of 17.25 ± 0.1 mb above 6 GeV/c. We conclude that 17.2 ± 0.2 mb is an appropriate interpolated value at 4.6 GeV/c and is compatible with other measurements of much poorer accuracy near this momentum.

4. G. V. Dass, C. Michael, and R. J. N. Phillips, Nucl. Phys. B9, 549 (1966).

5. M. Lusignoli, M. Restignoli, G. Violini, and G. A. Snow, Nuovo Cimento 45A, 792 (1966); A. D. Martin and F. Poole, Nucl. Phys. B4, 467 (1968); N. M. Queen, Nucl. Phys. B1, 207 (1967).

6. 1.45 GeV/c: A. Bettini et al., Phys. Letters 16, 83 (1965).
1.96 GeV/c: W. Chinowsky, G. Goldhaber, S. Goldhaber, T. O'Halloran, and B. Schwarzschild, Phys. Rev. 139B, 1411 (1965).
3.0 GeV/c: J. Debaisieux et al., Nuovo Cimento 43A, 142 (1966).
3.5 and 5.0 GeV/c: W. De Baere et al., Nuovo Cimento 45A, 885 (1966)
7.3 GeV/c: C. Y. Chien, E. Malamud, D. J. Mellema, P. E. Schlein, W. E. Slater, D H. Stork, and H. K. Ticho, Phys. Letters 28B, 615 (1969).

7. G. S. Abrams, L. Eisenstein, J. Kim, T. A. O'Halloran, Jr., W. Shufeldt, and J. Whitmore, University of Illinois Preprint COO-1195-156 (1969); A. S. Carroll et al., Phys. Rev. Letters 21, 1282 (1968); G. S. Abrams, L. Eisenstein, T. A. O'Halloran, Jr., W. Shufeldt, and J. Whitmore, Phys. Rev. Letters 21, 1407 (1968); D. Cline, C. Moore, and D. Reeder, Phys. Rev. Letters 19, 675 (1967); J. Banaigs et al., Phys. Letters 24B, 317 (1967); and W. F. Baker et al., Phys. Letters 28B, 291 (1968).

8. L. S. Schroeder, R. A. Leacock, R. L. Wagstaff, and W. J. Kernan, Phys. Rev. 176, 1648 (1968).

9. A. D. Krisch, Lectures on High Energy Proton-Proton Interactions Argonne National Laboratory Report ANL/HEP 6808.

10. M. Aderholz et al., Phys. Letters 24B, 434 (1967).
11. K. J. Foley, S. S. Lindenbaum, W. A. Love, S. Ozaki, J. J. Russell, and L. C. L. Yan, Phys. Rev. Letters 11, 503 (1963).
12. L. Stodolsky and J. J. Sakurai, Phys. Rev. Letters 11, 90 (1963).
13. Review talks by Chan Hong-Mo and O. Czyzewski in Proceedings of the 14th International Conference on High-Energy Physics, Vienna 28 August - 5 September, 1968 (CERN, 1968).
14. J. MacNaughton, Trilling-Goldhaber Internal Report # 177 (1969).
15. W. R. Butler, Strange Particle Production in π^+p Interactions Near 3.7 GeV/c (Ph. D. thesis), UCRL-19845 (1970), unpublished.
16. J. MacNaughton, Trilling-Goldhaber Internal Report # 174 (1969).
17. A. Citron, W. Galbraith, T. F. Kycia, B. A. Leontic, R. H. Phillips, A. Rousset, and P. H. Sharp, Phys. Rev. 144, 1101 (1966).
18. G. Gidal, G. Borreani, D. Grether, F. Lott, and R. W. Birge, Phys. Rev. Letters 23, 994 (1969).
19. Ling-Lie Wang, Phys. Rev. 153, 1664 (1967).
20. Krammer and U. Maor, Nuovo Cimento 50A, 963 (1967).
21. K. Bösebeck, H. Grassler, G. Kraus, R. Schulte, H. Böttcher, J. Kaltwasser, H. Kaufmann, S. Nowak, K. Böckmann, J. G. Bossen, H. Drevermann, W. Johnssen, M. Rost, K. Sternberger, U. Stöcker, A. Angelopoulos, J. R. Campbell, V. T. Cocconi, J. D. Hansen, W. Kittel, S. Matsumoto, D. R. O. Morrison, R. Stroynowski, J. B. Whittaker and J. Loskiewicz, Nucl. Phys. B28, 381 (1971).
22. D. Coyne, W. Butler, G. Fang-Landau, and J. MacNaughton, UCRL-20088 (1970), to be published in Nuclear Physics B.
23. R. W. Bland, M. G. Bowler, J. L. Brown, J. A. Kadyk, G. Goldhaber, S Goldhaber, V. H. Seeger, and G. H. Trilling, Nucl. Phys. B13, 595 (1969).

Table I. Correspondence between topology and event type code.

Event type code	Topology
10	One-prong
12	One positive outgoing track with decay
14	One positive outgoing track with decay + vee
17	One prong + vee
19	Two-prong with two positive decays
20	Two-prong
21	Two-prong with positive tau decay
22	Two-prong with positive decay
24	Two-prong with positive decay + vee
26	Two-prong with positive decay + 2 vees
27	Two-prong + vee
28	Two-prong + 2 vees
29	Two-prong + 3 vees
30	Two positive, one negative prong
31	Three positive prongs
32	Two positive, one negative track, 1 positive decay
33	Four-prong, positive tau decay
35	Four-prong, negative tau decay
36	Four-prong, two positive, one negative decay
37	Two positive, one negative prong + vee
38	Four-prong, one positive, one negative decay
39	Four-prong, two positive decays
40	Four-prong
41	Four-prong, negative decay
42	Four-prong, positive decay
43	Four-prong, negative decay + vee
44	Four-prong, positive decay + vee
45	Four-prong, negative decay + 2 vees
46	Four-prong, positive decay + 2 vees
47	Four-prong + vee
48	Four-prong + 2 vees
50	Three positive, 2 negative tracks
51	Four-positive, one negative tracks

60	Six-prong
61	Six-prong, one negative decay
62	Six-prong, one positive decay
63	Six-prong, one negative decay + vee
64	Six-prong, one positive decay + vee
67	Six-prong + vee
68	Six-prong + 2 vees
80	Eight-prong

Table II. Numbers of events of various topologies found in scanning the 4.6-GeV film on scan tables.

Event type code (explained in Table I)	Number of events
20	14750
22	204
24	53
26	2
27	2592
28	47
30	709
40	7621
41	28
42	224
43	3
44	6
47	620
48	8
60	371
61	2
62	6
67	15

Table III. Number of events rejected for various reasons.

1.	Not beam track	2224
2.	Outside fiducial volume	353
3.	Zero constraint	128
4.	Ambiguous	673
5.	Not to be measured	465
6.	No event	27

Table IVa. Distribution of accepted two-prong events.

Elastic scattering events with four constraints	3957
Elastic scattering events with three constraints	80
Events with one missing neutral	3034
Events with two or more missing neutrals	4208
Inelastic events in which a constraint is dropped	128
Total	11,407

Table IVa.

	Unambiguous	Ambiguous
$K^0 p \pi^+$	931	591
$K^+ p \pi^0$	666	501
$K^+ \pi^+ n$	434	700

Table V. Angular distribution for K^+p elastic scattering.

$\lvert t\rvert$ $(GeV/c)^2$	Average value of cos θ	$\left[\frac{d\sigma/dt}{(GeV/c)^2}\right]$ mb	N_{corr} [a]	$\lvert t\rvert$ $(GeV/c)^2$	Average value of cos θ	$\left[\frac{d\sigma/dt}{(GeV/c)^2}\right]$ mb	N_{corr}
0.050-0.075	0.9835	13.20±1.08	400	0.725-0.750	0.8059	0.56±0.14	17
0.075-0.100	0.9770	11.91±1.00	361	0.750-0.775	0.7993	0.56±0.14	17
0.100-0.125	0.9704	9.50±0.83	288	0.775-0.800	0.7927	0.46±0.13	14
0.125-0.150	0.9638	8.38±0.76	254	0.800-0.825	0.7861	0.56±0.14	17
0.150-0.175	0.9572	8.05±0.73	244	0.825-0.850	0.7795	0.66±0.15	20
0.175-0.200	0.9506	6.30±0.61	191	0.850-0.875	0.7730	0.36±0.11	11
0.200-0.225	0.9441	6.83±0.65	207	0.875-0.900	0.7664	0.46±0.13	14
0.225-0.250	0.9375	6.57±0.63	199	0.900-0.925	0.7598	0.26±0.09	8
0.250-0.275	0.9311	5.71±0.57	173	0.925-0.950	0.7532	0.36±0.11	11
0.275-0.300	0.9243	5.02±0.52	152	0.950-0.975	0.7466	0.20±0.08	6
0.300-0.325	0.9177	3.80±0.43	115	0.975-1.000	0.7401	0.40±0.12	12
0.325-0.350	0.9112	3.50±0.41	106	1.0-1.1	0.7236	0.27±0.05	33
0.350-0.375	0.9046	3.14±0.38	95	1.1-1.2	0.6973	0.17±0.04	20
0.375-0.400	0.8980	3.37±0.40	102	1.2-1.3	0.6710	0.11±0.03	13
0.400-0.425	0.8914	2.90±0.36	88	1.3-1.4	0.6446	0.033±0.02	4
0.425-0.450	0.8848	2.51±0.33	76	1.4-1.5	0.6183	0.041±0.02	5
0.450-0.475	0.8783	2.48±0.33	75	1.5-1.6	0.5920	0.033±0.02	4
0.475-0.500	0.8717	2.18±0.30	66	1.6-1.7	0.5657	0.016±0.01	2
0.500-0.525	0.8651	1.95±0.28	59	1.7-1.8	0.5394	0.024±0.01	3
0.525-0.550	0.8585	1.75±0.27	53	1.8-1.9	0.5130	0.008±0.01	1
0.550-0.575	0.8519	1.39±0.23	42	1.9-2.0	0.4867	0.008±0.01	1
0.575-0.600	0.8454	1.19±0.21	36	2.0-3.0	0.3419	0.002±0.001	2
0.600-0.625	0.8388	1.29±0.22	39	3.0-4.0	0.0787	0.002±0.001	3
0.625-0.650	0.8322	1.09±0.20	33	4.0-5.0	-0.1845	0.001±0.001	1
0.650-0.675	0.8256	0.83±0.17	25	5.0-6.0	-0.4477	0.002±0.001	3
0.675-0.700	0.8190	1.02±0.20	31	6.0-7.0	-0.7110	0.005±0.002	6
0.700-0.725	0.8126	0.96±0.19	29	7.0-7.6	-0.9213	0.007±0.003	5

[a] N_{corr} is the number of events except for the first three values of $\lvert t\rvert$ where a correction was added to the numbers of events to correct for a dip in the azimuthal angular distribution of events around the beam due to reduced scanning efficiency for events with short recoil protons which were travelling nearly toward or away from the camera. The errors were increased accordingly in these three cases.

Table VI. List of reactions studied in regard to single-pion production in the K^+p experiment.

Topology
i) two-prong
ii) two-prong with vee
iii) three-prong (τ decay)

Reactions	
$K^+p \rightarrow K^0 + p + \pi^+$	(1)
$\rightarrow K^+ + p + \pi^0$	(2)
$\rightarrow K^+ + n + \pi^+$	(3)
$K^+ \rightarrow \pi^+ + \pi^+ + \pi^-$	(4)

Table VII. Classes of events used in study of pK^* final state.

Topology	Reaction	Fit used
(ii)	Unambiguous $K^0 p\pi^+$	$K^0 p\pi^+$
(i)	Unambiguous $K^0 p\pi^+$	$K^0 p\pi^+$
(i)	Unambiguous $K^+ p\pi^0$	$K^+ p\pi^0$
(i)	Ambiguous $K^0 p\pi^+$ or $K^+ p\pi^0$	$K^0 p\pi^+$

Table VIII. Number of events of each topology found during the original scan—π^+ experiment (does not contain the 1000 frames of film with a pure proton beam).

	All measured				All measured except two-prong events without stopping protons						
Beam momentum (MeV/c) ⟶	3559.5	3676.4	3996.9	Sum	3676.4	3728.1	3750.6	3819.7	3996.9	Sum	Total
Event type code (Table I)											
10	30	168	13	211	64	39	3	115	55	276	487
12		1		1					1	1	2
14		1		1				1		1	2
17		1		1	1			1		2	3
19	1	16	1	18	8	2	1	6	5	22	40
20	12,704	41,415	2574	56,693	3172	1985	218	5116	2380	12,871	69,564
21		1		1	1			2	3	6	7
22	189	556	27	772	158	107	20	344	149	778	1550
24	27	99	2	128	44	35	4	88	28	199	327
26	2	2	1	5		3		1	2	6	11
27	304	1052	27	1383	389	235	34	644	321	1623	3006
28	26	84	3	113	40	17	3	68	31	159	272
29		1		1							1
30	8	66	2	76	11	14	4	49	26	104	180
31		6		6		2		2		4	10
32					1			1		2	2
33											
35								1		1	1
36											
37											
38	1	4		5	8	3		4	1	16	21
39		5		5	4	5		10	2	21	26
40	5963	21,372	874	28,209	9683	6112	763	15,965	8222	40,745	68,954
41	25	110	6	141	43	23	3	90	40	199	340
42	93	353	9	455	135	106	24	306	161	732	1187
43	3	2		5	4	6		19	1	30	35
44	2	19	3	24	3	1		11	3	18	42
45								2	2	4	4
46					1					1	1
47	50	136	3	189	63	33	4	78	55	233	422
48	1	3		4	1		1	1		3	7
50	1	10		11	3	5		7	5	20	31
51	5	9		14	4	2		12	2	20	34
60	266	990	34	1290	430	310	29	852	501	2122	3412
61	4	7		11	2	1		4	3	10	21
62	5	12	2	19	5	1	1	17	11	35	54
63								1	1	2	2
64											
67		2		2	3	1		1	1	6	8
68											
80	1	2		3	3	2	1	4	6	16	19
Other	22	60	2	84	32	10	4	58	35	139	223
Total	19,733	66,565	3583	89,881	14,316	9060	1117	23,881	12,053	60,427	150,308

Table IXa. List of reasons for rejecting events.

Reason number	Reason
1	Too many tracks—more than 30 beam tracks in the picture
2	outside fiducial volume—a fiducial volume was chosen to exclude events whose vertices were near the edge of the chamber.
3	No event—event cannot be located, but chance configuration of tracks simulates events or event is secondary and primary is outside fiducial volume.
4	Immeasureable—film is defective (torn, warped, double-exposed, missing) or event is covered by flare.
5	Nonbeam track.
6	Baryon going backward in lab frame.
7	Two-prong event without stopping proton on roll where two-prong events without stopping proton were not measured.
8	Zero constraint—a track was so short owing to secondary interaction or decay that its momentum could not be measured to better than 30%, leading to loss of a constraint. No fit with no missing neutral particles was achieved.
9	No fit—event was very far from any fit, even as a "missing mass" event.
10	Wrong type—K^+ recognizeable by ionization in a two-, four-, or six-prong topology without vee decay, and fits in the SIOUX program having the proper track assigned to be K^+, if any, had too large a χ^2.
11	Two recognizeable baryons in the final state.

Table IXb. Numbers of two-prong events rejected for various reasons.

	All measured				All measured except two-prong events without stopping protons						
Beam momentum (MeV/c) ⟶	β559.5	3676.4	3996.9	Sum	3676.4	3728.1	3750.6	3819.7	3996.9	Sum	Total
Reason number (Table IXa)											
1		1		1						0	1
2	2057	5037	265	7359	328	181	22	4	200	735	8094
3	47	168	9	224	18	6		449	8	481	705
4	11	29	1	41		1		32		33	74
5	719	1502	83	2304	113	44	6	134	56	353	2657
6		3	2	5	1	2		4	1	8	13
7				0	152	104	4	315	115	690	690
8	108	431	26	565	4	8		10	8	30	595
9				0						0	0
10	7	24		31	1					0	31
11	4	20		30					1	2	32

Table X. Numbers of accepted events of various final states from π^+p interactions.

Final state	3.56 GeV/c	Sample for subtraction of proton contamination 3.56 GeV/c	3.67 GeV/c	Sample for subtraction of proton contamination 3.67 GeV/c
Ambiguous between π^+p and $p\pi^+$	1	0	0	0
Unambiguous π^+p	2761	351	5137	1324
Unambiguous $\pi^+p\pi^0$	1133	130	1944	410
Ambiguous between $\pi^+p\pi^0$ and $p\pi^+\pi^0$	37	8	73	16
Ambiguous between $\pi^+p\pi^0$, $p\pi^+\pi^0$ and $\pi^+\pi^+n$	3	0	23	3
Ambiguous between $\pi^+p\pi^0$ and $\pi^+\pi^+n$	108	7	277	35
Unambiguous $\pi^+\pi^+n$	686	121	1347	360
Unambiguous π^+pMM	1668	315	2963	805
Ambiguous between π^+pMM and $p\pi^+MM$	4	1	1	3
Ambiguous between π^+pMM, $p\pi^+MM$ and $\pi^+\pi^+MM$	11	3	42	15
Ambiguous between $p\pi MM$ and $\pi^+\pi^+MM$	769	127	1445	320
Unambiguous $\pi^+\pi^+MM$	775	47	1258	177
Total two prong	7956	1100	14510	3468
Unambiguous $K^+K^-\pi^+p$	27[a]	1[a]	54[a]	2[a]
Ambiguous between $K^+K^+\pi^+p$ and $pp\pi^+\pi^-$	0	0	5	11
Ambiguous between $K^+K^-p\pi^+$ and $K^+K^-\pi^+p$	0	0	2	0
Unambiguous $\pi^+p\pi^+\pi^-$	1454	61	2451	117
Ambiguous between $\pi^+p\pi^+\pi^-$ and $pp\pi^+\pi^-$	34	4	103	39
Ambiguous between $\pi^+p\pi^+\pi^-$ and $p\pi^+\pi^+\pi^-$	10	1	46	1
Unambiguous $pp\pi^+\pi^-$	78	75	230	302
Unambiguous $pp\pi^+\pi^-$, four-constraint fit	75[b]	72[b]	220[b]	294[b]
Unambiguous $\pi^+\pi^+\pi^+\pi^-n$	222	5	427	43
Unambiguous $p\pi^+\pi^+\pi^-\pi^0$	1398	81	2548	181
Ambiguous between $p\pi^+\pi^+\pi^-\pi^0$ and $\pi^+\pi^+\pi^+\pi^-n$	19	1	51	4
Ambiguous between $p\pi^+\pi^+\pi^-\pi^0$ and $\pi^+p\pi^+\pi^-\pi^0$	16	0	38	8
Unambiguous $\pi^+\pi^+\pi^+\pi^-MM$	197	9	336	21
Ambiguous between $\pi^+\pi^+\pi^+\pi^-MM$ and $p\pi^+\pi^+\pi^-MM$	45	9	124	29
Unambiguous $p\pi^+\pi^+\pi^-MM$	511	53	831	172
Ambiguous between $p\pi^+\pi^+\pi^-MM$ and $\pi^+p\pi^+\pi^-MM$	1	1	1	5
Unambiguous $p\pi^+\pi^+\pi^-\pi^-\pi^+$	75	7	146	12
Unambiguous $\pi^+\pi^+\pi^+\pi^+\pi^-\pi^-n$	6	0	12	0
Unambiguous $p\pi^+\pi^+\pi^+\pi^-\pi^-\pi^0$	65	2	124	10
Unambiguous $p\pi^+\pi^+\pi^+\pi^-\pi^-MM$	6	0	14	0
Unambiguous $\pi^+\pi^+\pi^+\pi^+\pi^-\pi^-MM$	1	0	1	0
Strange particles	301	9	560	57
Total	12422	1429	22614	4483

[a]Does not include contributions from strange-particle topologies.
[b]Subset of preceding category.

Table XI. Definitions of symbols used in cross-section determination.

N^{π}_{eA}	number of accepted elastic-scattering events in a cross-section sample
N^{p}_{eA}	number of accepted elastic-scattering events in a proton test sample
N^{π}_{tA}	total number of accepted events in a cross-section sample (includes $pp \rightarrow pp\pi^+\pi^-$)
N^{p}_{tA}	total number of accepted events in a proton test sample (included $pp \rightarrow pp\pi^+\pi^-$)
N^{π}_{z}	number of zero-constraint rejects in a cross-section sample
N^{p}_{z}	number of zero-constraint rejects in a proton test sample
N^{π}_{w}	number of wrong-type rejects in a cross-section sample
N^{p}_{w}	number of wrong-type rejects in a proton test sample
W	Weighting factor for proton subtraction
N^{π}_{ue}	number of unresolved events which are elastic-scattering events in cross-section sample
N^{p}_{ue}	number of unresolved events which are elastic-scattering events in proton test sample
N^{π}_{uN}	number of unresolved events which are not elastic-scattering events in cross-section sample
N^{p}_{uN}	number of unresolved events which are not elastic-scattering events in proton test sample
N_{XA}	number of accepted events lost owing to difficulty of finding small-angle elastic scatters after correction for proton contamination
N^{c}_{eA}	$= N^{\pi}_{eA} - WN^{p}_{eA} + N_{XA}$
N^{c}_{ue}	$= \dfrac{N_{XA}}{N^{\pi}_{eA} - WN^{p}_{eA}} \left(N^{\pi}_{ue} - WN^{p}_{ue}\right)$
N^{π}_{N}	$= N^{\pi}_{tA} - N^{\pi}_{eA} + N^{\pi}_{2} + N^{\pi}_{w}$
N^{p}_{N}	$= N^{p}_{tA} - N^{p}_{eA} + N^{p}_{2} + N^{p}_{w}$

N^{π}_{4c}	number of unambiguous fits to $\pi^+p \rightarrow \pi^+p\pi^+\pi^-$ in a cross-section sample
N^{p}_{4c}	number of unambiguous fits to $\pi^+p \rightarrow \pi^+p\,\pi^+\pi^-$ in a proton test sample
N^{π}_{4cA}	number of ambiguous fits to $\pi^+p \rightarrow \pi^+p\pi^+\pi^-$ in a cross-section sample
N^{p}_{4cA}	number of ambiguous fits to $\pi^+p \rightarrow \pi^+p\pi^+\pi^-$ in a proton test sample
N^{π}_{4cu}	number of unresolved events estimated to be $\pi^+p \rightarrow \pi^+p\pi^+\pi^-$ in a cross-section sample
N^{p}_{4cu}	number of unresolved events estimated to be $\pi^+p \rightarrow \pi^+p\pi^+\pi^-$ in a proton test sample
N^{π}_{60-4c}	number of fits to $\pi^+p \rightarrow \pi^+p\pi^+\pi^+\pi^-\pi^-$ in a cross-section sample
N^{p}_{60-4c}	number of fits to $\pi^+p \rightarrow \pi^+p\pi^+\pi^+\pi^-\pi^-$ in a proton test sample
N^{π}_{60-4cu}	number of unresolved events estimated to be $\pi^+p \rightarrow \pi^+p\pi^+\pi^+\pi^-\pi^-$ in a cross-section sample
N^{p}_{60-4cu}	number of unresolved events estimated to be $\pi^+p \rightarrow \pi^+p\pi^+\pi^+\pi^-\pi^-$ in a proton test sample.

Table XII. Values of quantities need to determine elastic cross section.

Quantity	3.56 GeV/c	3.67 GeV/c	Quantity	3.56 GeV/c	3.67 GeV/c
N^{π}_{eA}	2762	5137	N^{π}_{4c}	1464	2497
N^{p}_{eA}	351	1324	N^{p}_{4c}	62	118
N^{π}_{tA}	12422	22614	N^{π}_{4cA}	34	103
N^{p}_{tA}	1429	4483	N^{p}_{4cA}	4	39
N^{π}_{z}	178	370	N^{π}_{4cu}	113.9	194.5
N^{p}_{z}	20	62	N^{p}_{4cu}	3.8	19.5
N^{π}_{w}	39	40	N^{π}_{60-4c}	75	146
N^{p}_{w}	4	5	N^{p}_{60-4c}	7	12
W	1.04	0.75	N^{π}_{60-4cu}	17.8	32.3
N^{π}_{ue}	138	229.7	N^{p}_{60-4cu}	0	3.6
N^{p}_{ue}	59.8	83	$\Delta(N^{\pi}_{4c})$	38.26	49.97
N^{π}_{uN}	404	711.3	$\Delta(N^{p}_{4c})$	7.87	10.86
N^{p}_{uN}	41.2	92	$\Delta(N^{\pi}_{4cA})$	5.83	10.15
N_{XA}	481.3	1130.6	$\Delta(N^{p}_{4cA})$	2	6.24
$\Delta(N_{eA})$	91.1	128.9	$\Delta(N^{\pi}_{4cu})$	22.8	38.9
$\Delta(N^{\pi}_{ue})$	19.1	42.8	$\Delta(N^{p}_{4cu})$	0.76	3.9
$\Delta(N^{p}_{ue})$	9.2	13.5			
$\Delta(W)$	0.17	0.07			
$\Delta(N^{c}_{ue})$	10	20			
$\Delta(N^{\pi})$	99.4	133.7			
$\Delta(N^{p})$	33.2	56.8			
$\Delta(N^{\pi}_{uN})$	25.1	48.1			
$\Delta(N^{p}_{uN})$	8.1	13.9			

Table XIII. Assignment of unresolved events.

	3.56 GeV/c	Sample for proton subtraction at 3.56 GeV/c	3.67 GeV/c	Sample for proton subtraction at 3.67 GeV/c
Events which were elastic scatters	129	57	204	75
2-prong events which were not elastic	83	16	136	26
Non-2-prong events	308	19	538	53
2-prong events which should have been rejected	10	0	18	4
2-prong events with insufficient measurement information	13	9	40	21
2-prong events—borderline cases	9	0	23	0

Table XIV. Cross sections for various final states.

Final state	Cross section (mb)	
Beam momentum ⟶	3.56 GeV/c	3.67 GeV/c
$p\pi^+$	6.93±0.23	7.15±0.21
$p\pi^+\pi^+\pi^-$	3.59±0.14	3.47±0.12
$p\pi^+\pi^+\pi^+\pi^-\pi^-$	0.20±0.02	0.22±0.02
$p\pi^+\pi^0$	2.51±0.2	2.36±0.2
$n\pi^+\pi^+$	1.50±0.2	1.68±0.3
$p\pi^+\pi^+\pi^-\pi^0$	3.22±0.1	3.32±0.1
$n\pi^+\pi^+\pi^-\pi^+$	0.55±0.03	0.57±0.04
$p\pi^+\pi^+\pi^-\pi^+\pi^-\pi^0$	0.17±0.02	0.165±0.02
$n\pi^+\pi^+\pi^+\pi^+\pi^-\pi^-$	0.016±0.03	0.017±0.02
$p\pi^+$MM	3.68±0.65	3.76±0.7
$\pi^+\pi^+$MM	2.76±1.2	2.50±1.3
$p\pi^+\pi^+\pi^-$MM	1.13±0.07	0.99±0.1
$\pi^+\pi^+\pi^+\pi^-$MM	0.51±0.07	0.52±0.1
$p\pi^+\pi^+\pi^-\pi^-\pi^+$MM	0.016±0.007	0.019±0.006
$\pi^+\pi^+\pi^+\pi^+\pi^-\pi^-$MM	0.003	0.001

Table XV. Differential cross section, $d\sigma/dt$, for π^+p elastic scattering.[a]

t interval $(GeV/c)^2$	$\frac{d\sigma}{dt}$ $\left[\frac{mb}{(GeV/c)^2}\right]$
0.05 - 0.1	27.76 ±1.05
0.1 - 0.15	18.78 ±0.75
0.15 - 0.2	14.62 ±0.61
0.2 - 0.25	9.23 ±0.42
0.25 - 0.3	7.56 ±0.42
0.3 - 0.35	5.45 ±0.35
0.35 - 0.4	3.57 ±0.28
0.4 - 0.45	2.78 ±0.23
0.45 - 0.5	1.81 ±0.20
0.5 - 0.55	1.68 ±0.17
0.55 - 0.6	0.91 ±0.13
0.6 - 0.7	0.89 ±0.08
0.7 - 0.8	0.46 ±0.06
0.8 - 0.9	0.376±0.052
0.9 - 1	0.302±0.048
0.1 - 1.1	0.181±0.38
1.1 - 1.2	0.289±0.047
1.2 - 1.3	0.235±0.041
1.3 - 1.4	0.154±0.032
1.4 - 1.5	0.168±0.038
1.5 - 1.6	0.148±0.036
1.6 - 1.7	0.121±0.030
1.7 - 1.8	0.060±0.020
1.8 - 1.9	0.047±0.018
1.9 - 2.0	0.060±0.020
2.0 - 2.1	0.054±0.019
2.1 - 2.4	$0.0200^{+0.006}_{-0.005}$
2.4 - 2.7	$0.0123^{+0.005}_{-0.004}$
2.7 - 3.0	$0.00615^{+0.004}_{-0.002}$
3.0 - 3.3	$0.00308^{+0.0030}_{-0.0015}$

Table XV. (contd.)

t interval $(GeV/c)^2$	$\frac{d\sigma}{dt}$ $\left[\frac{mb}{(GeV/c)^2}\right]$
3.3 - 3.6	$0.00461^{+0.0035}_{-0.0020}$
3.6 - 3.9	$0.00923^{+0.0046}_{-0.0031}$
3.9 - 4.2	$0.0123^{+0.0052}_{-0.0036}$
4.2 - 4.5	$0.0108^{+0.0049}_{-0.0034}$
4.5 - 4.8	$0.0154^{+0.0057}_{-0.0042}$
4.8 - 5.1	$0.0354^{+0.0082}_{-0.0066}$
5.1 - 5.4	$0.0277^{+0.0073}_{-0.0058}$
5.4 - 5.7	$0.0338^{+0.0080}_{-0.0065}$
5.7 - 6.0	$0.0185^{+0.0062}_{-0.0046}$
> 6.0	$0.0923\pm^{+0.034}_{-0.025}$

[a] An azimuthal correction was made for t from 0.05 to 0.6 $(GeV/c)^2$ but not for $t > 0.6$. The proton subtraction was made for t from 0.05 to 2.1, but not for $t > 2.1$.

Table XVI. Differential cross section, $d\sigma/dt$, for π^+p elastic scattering for the region t = 0.05-0.8.[a]

t interval $(GeV/c)^2$	$\frac{d\sigma}{dt}$ $\left[\frac{mb}{(GeV/c)^2}\right]$
0.05-0.06	32.87±2.85
0.06-0.07	31.66±2.61
0.07-0.08	28.55±2.31
0.08-0.09	28.66±2.16
0.09-0.10	21.20±1.91
0.10-0.11	20.25±1.82
0.11-0.12	17.92±1.72
0.12-0.13	19.85±1.64
0.13-0.14	17.94±1.59
0.14-0.15	18.10±1.58
0.15-0.16	17.14±1.50
0.16-0.17	15.13±1.35
0.17-0.18	14.32±1.37
0.18-0.19	12.18±1.32
0.19-0.20	12.71±1.25
0.20-0.21	12.19±1.24
0.21-0.22	9.15±1.15
0.22-0.23	8.97±1.12
0.23-0.24	8.27±1.02
0.24-0.25	7.25±0.99
0.25-0.26	10.05±1.07
0.26-0.27	7.09±0.90
0.27-0.28	7.05±0.90
0.28-0.29	7.70±0.94
0.29-0.30	4.72±0.82
0.30-0.31	8.23±0.89
0.31-0.32	4.16±0.72
0.32-0.33	6.61±0.85
0.33-0.34	5.22±0.80
0.34-0.35	3.95±0.67
0.35-0.36	3.60±0.68

Table XVI. (contd.)

t interval $(GeV/c)^2$	$\frac{d\sigma}{dt}$ $\left[\frac{mb}{(GeV/c)^2}\right]$
0.36-0.37	3.50±0.64
0.37-0.38	3.15±0.59
0.38-0.39	3.90±0.64
0.39-0.40	3.30±0.65
0.40-0.41	2.89±0.52
0.41-0.42	3.36±0.57
0.42-0.43	2.29±0.52
0.43-0.44	2.84±0.55
0.44-0.45	2.03±0.48
0.45-0.46	2.11±0.46
0.46-0.47	1.62±0.43
0.47-0.48	1.77±0.43
0.48-0.49	2.17±0.48
0.49-0.50	1.60±0.41
0.50-0.51	1.60±0.38
0.51-0.52	1.85±0.38
0.52-0.53	1.51±0.43
0.53-0.54	1.52±0.37
0.54-0.55	0.95±0.32
0.55-0.56	0.63±0.32
0.56-0.57	1.34±0.38
0.57-0.58	0.71±0.31
0.58-0.59	0.79±0.25
0.59-0.60	0.87±0.26
0.60-0.61	0.95±0.27
0.61-0.62	1.25±0.33
0.62-0.63	1.18±0.30
0.63-0.64	0.86±0.26
0.64-0.65	0.79±0.27
0.65-0.66	0.79±0.25
0.66-0.67	0.70±0.23

Table XVI. (contd.)

t interval $(GeV/c)^2$	$\frac{d\sigma}{dt}$ $\left[\frac{mb}{(GeV/c)^2}\right]$
0.67-0.68	0.70±0.23
0.68-0.69	1.09±0.29
0.69-0.70	0.46±0.22
0.70-0.71	0.70±0.26
0.71-0.72	1.01±0.30
0.72-0.73	0.39±0.21
0.73-0.74	0.15±0.15
0.74-0.75	0.46±0.19
0.75-0.76	0.54±0.20
0.76-0.77	0.69±0.23
0.77-0.78	0.38±0.23
0.78-0.79	0.23±0.13
0.79-0.80	0.23±0.13

[a]An azimuthal correction was made for t from 0.05 to 0.6 $(GeV/c)^2$, but not for $t > 0.6$.

Table XVII. Angular regions used for fits to determine spin-density matrix elements for ρ^+ production. (Each reference frame has a polar angle P and an azimuthal angle η. In order to avoid interference with diffraction in certain t'_p regions, the forward region of cos P was avoided.)

t'_p region	Forward region of cos P avoided
0-0.05	Yes
0.05-0.1	Yes
0.1-0.2	Yes
0.6-0.8	No
0.8-1	No
1.0-2.0	No
0-0.08	Yes
0.08-0.5	Yes
0.5-2.2	No
all t'_p	Yes

Regions used for spin-density matrix element determination in those cases where the forward region of cos P was avoided

Spin density matrix element	Region 1	Region 2
ρ_{00}	cos P-1-0.5	cos P -0.5+0.5
ρ_{1-1}	cos P < 0 η0-45, 135-225, 315-360	cos P < 0 η 45-135, 225-315
Re ρ_{10}	cos P< 0 η0-90, 270-360	cos P < 0 η 90-270

Regions used for spin density matrix element determination in those cases where the forward region of cos P was not avoided

Spin density matrix element	Region 1	Region 2
ρ_{00}	|cos P| > 0.5	|cos P| < 0.5
ρ_{1-1}	η 0-45, 135-225, 315-360	η 45-135, 225-315
Re ρ_{10}	cos P -1-0, η0-90, 270-360; cos P0 1 η 90-270	cos P-1 0 η 90-270; cos P0 1 η 0-90, 270-360

Table XVIII. Δ^{++}-ρ^{+} interference fit results.

t' region	Number of bins	No interference χ^2	No interference $A_{\pi\pi}$	Interference χ^2	Interference $A_{\pi\pi}$	d	ϕ_0
All t'	48	56.5	0.1 ±0.3	51.3	0.3 ±0.3	0.3 ±0.15	124±23
t' 0-0.5	40	64.5	0.35±0.35	61.3	0.45±0.4	0.2 ±0.15	97±33
t' 0-0.08	25	15.1	1.75±1	14.2	2.1 ±1	0.2 ±0.2	164±62
t' 0.08-0.5	31	34.1	-0.35±0.3	30.1	-0.1 ±0.35	0.35±0.2	170±27

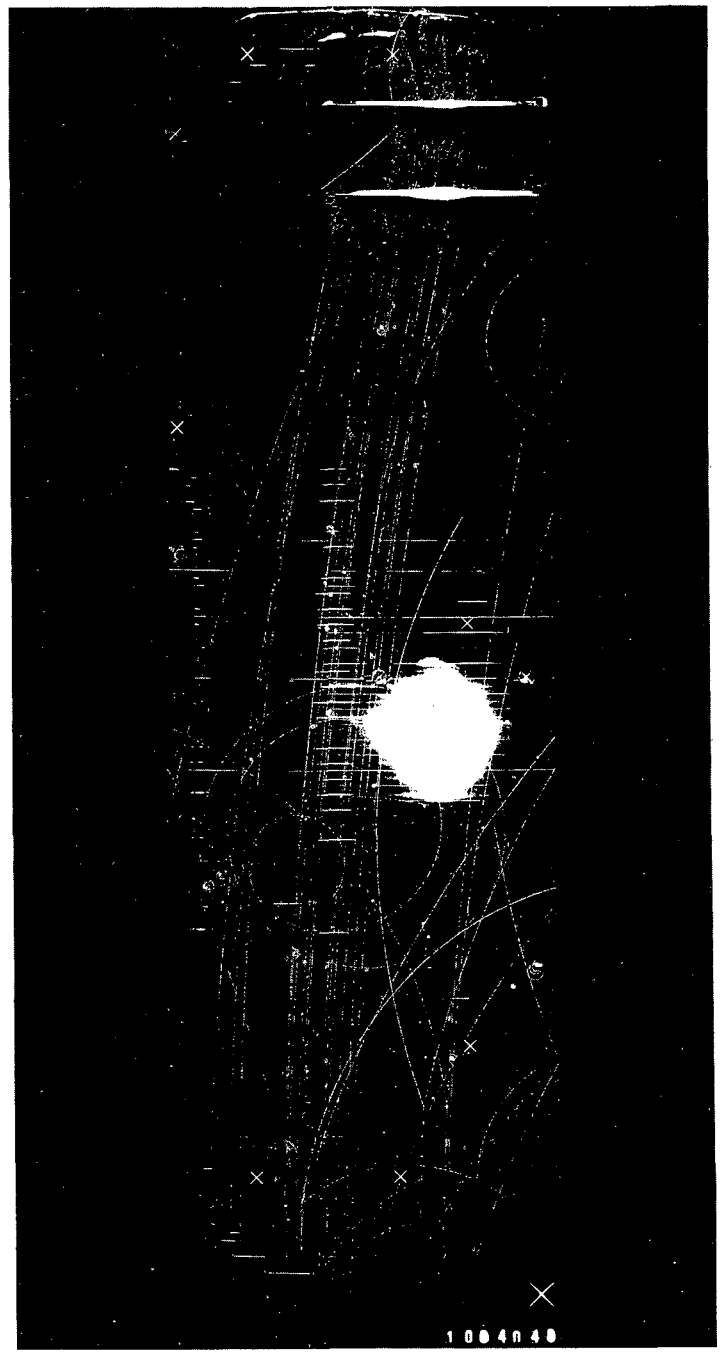

Fig. 1. A typical frame of film. There is a two-prong and a four-prong event. (XBB 711-42)

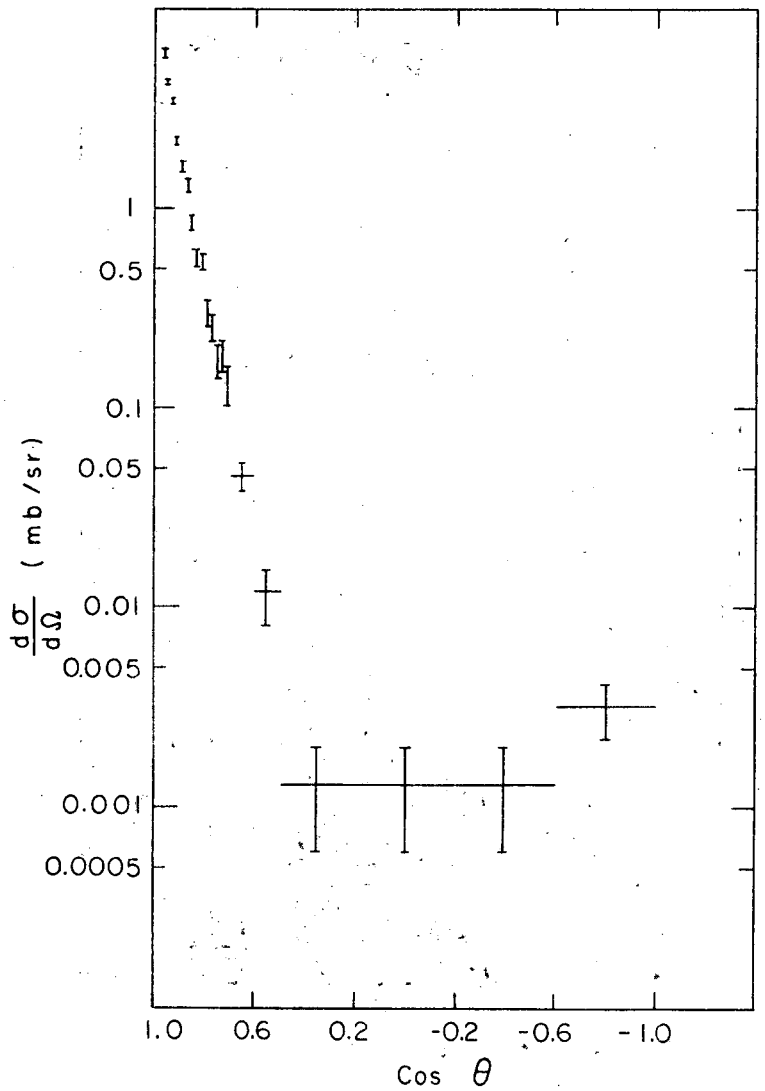

XBL696-3147

Fig. 2. Differential cross section, $d\sigma/d\Omega$, for K^+p elastic scattering at 4.6 GeV/c.

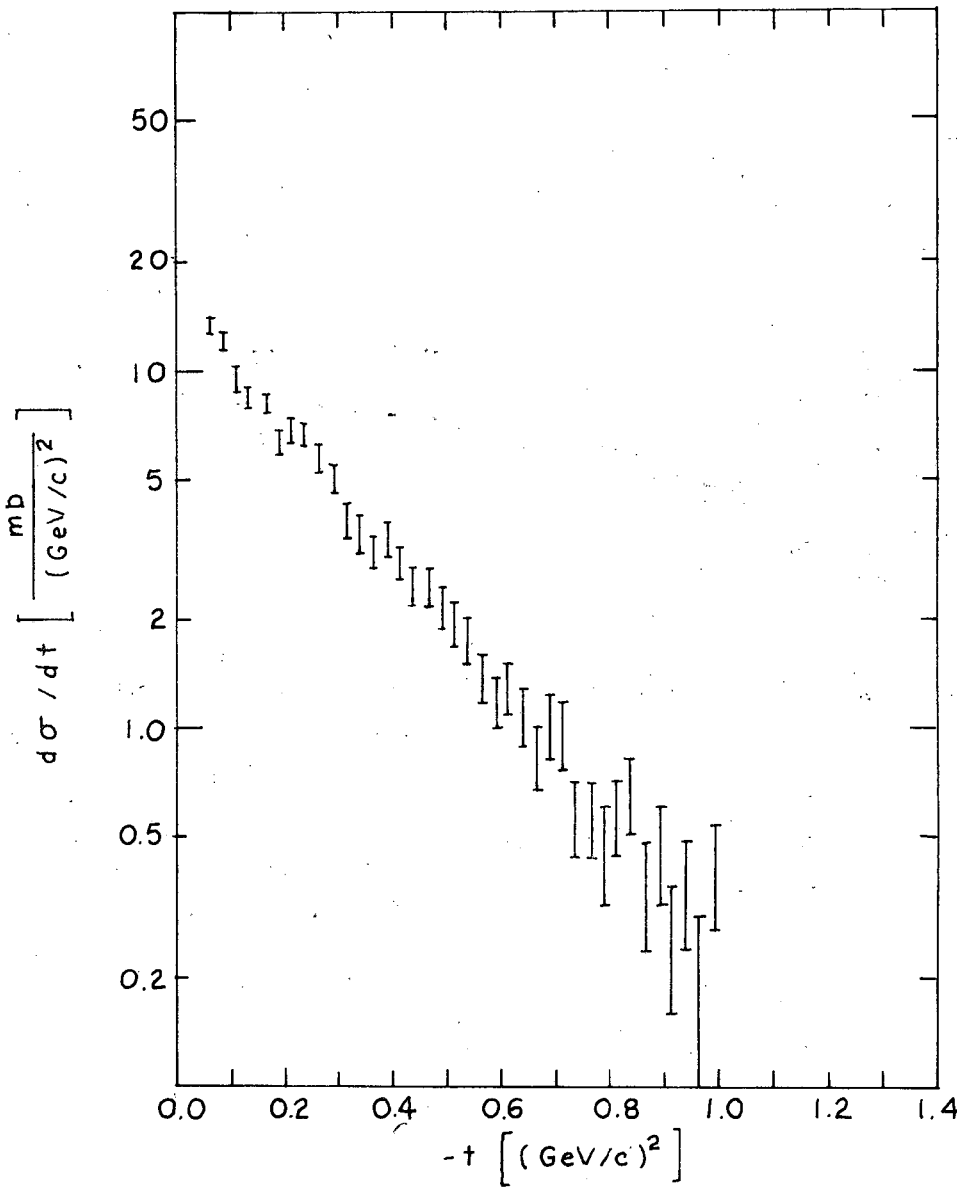

XBL696-3149A

Fig. 3. Differential cross section in terms of momentum transfer squared for forward angles.

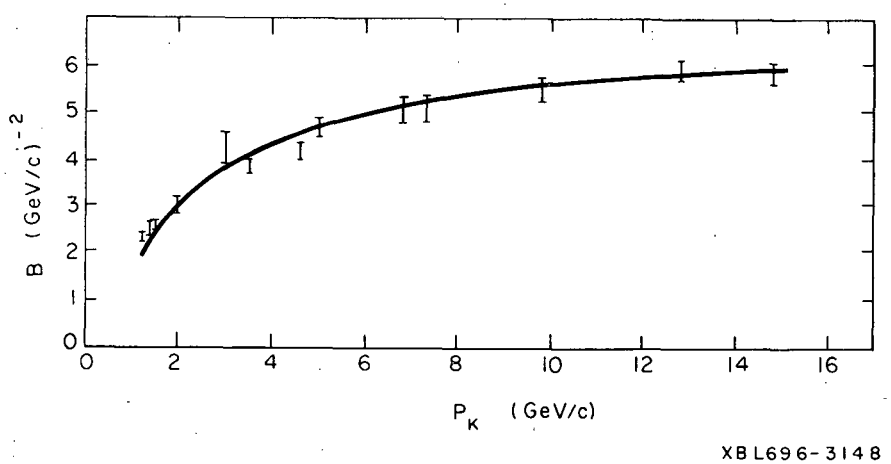

Fig. 4. Momentum dependence of the parameter B in the fit to the diffraction region of the form e^{Bt}. The solid curve is the function $6.8\ \beta^2\ (\mathrm{GeV}/c)^{-2}$.

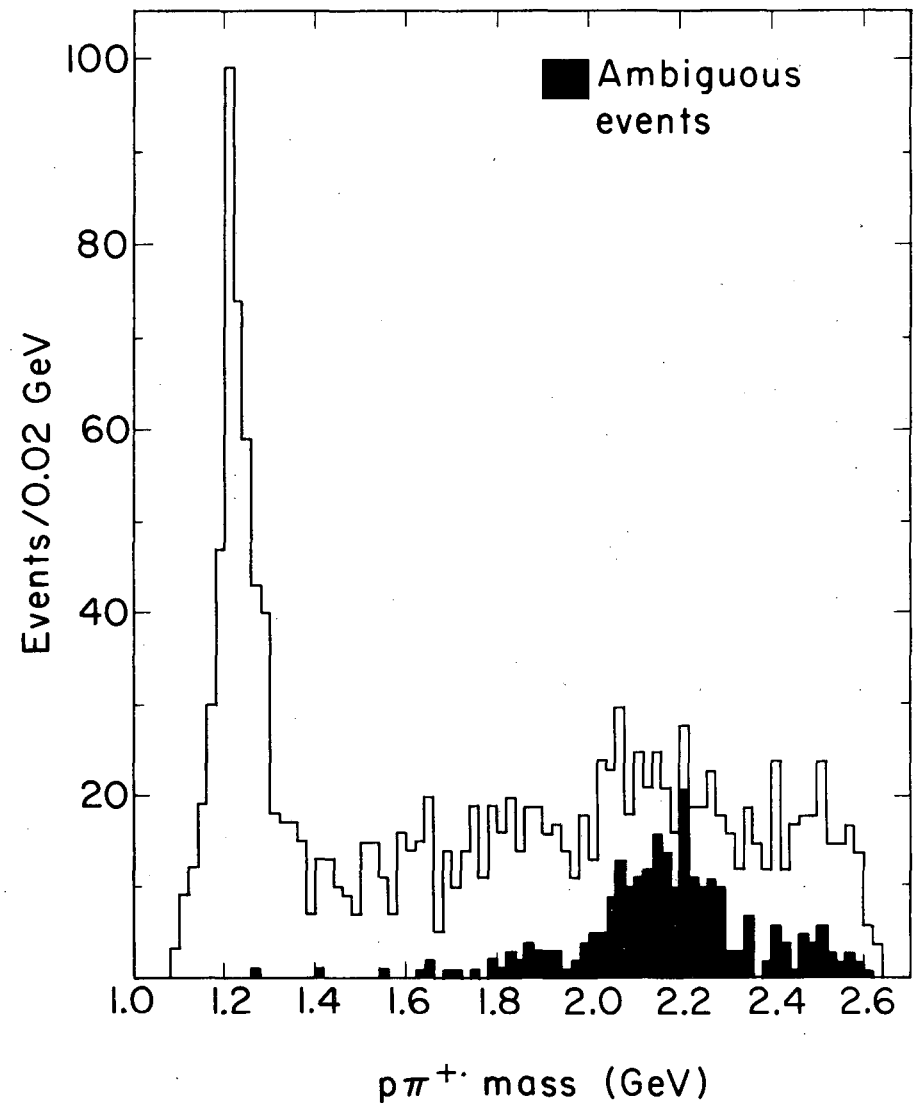

Fig. 5. $p\pi^+$ mass spectrum in the $K^0p\pi^+$ final state with $-t_K < 2(\mathrm{GeV}/c)^2$. All topologies are included, and ambiguous events are shaded.

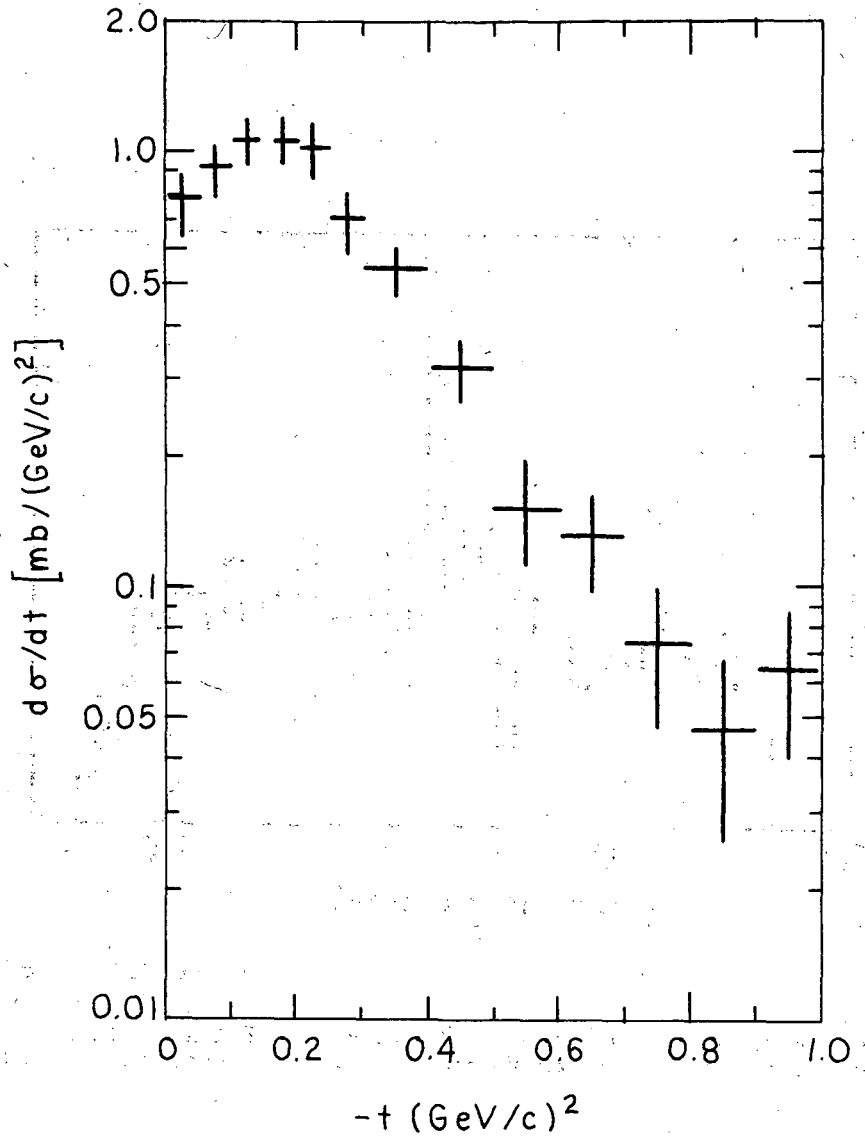

XBL706-3145A

Fig. 6. Momentum-transfer distribution in the reaction $K^+p \rightarrow K^0\ \Delta^{++} \rightarrow K^0 p\pi^+$.

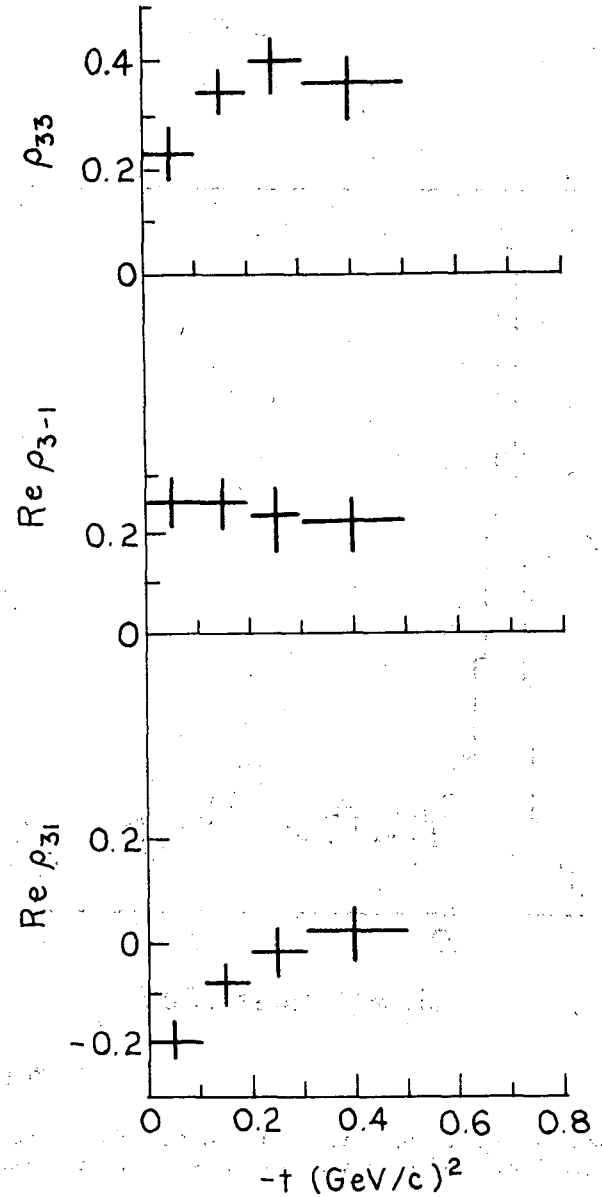

XBL-706-3144A

Fig. 7. Density matrix elements for the Δ from the reaction $K^+p \rightarrow K^0\ \Delta^{++}$.

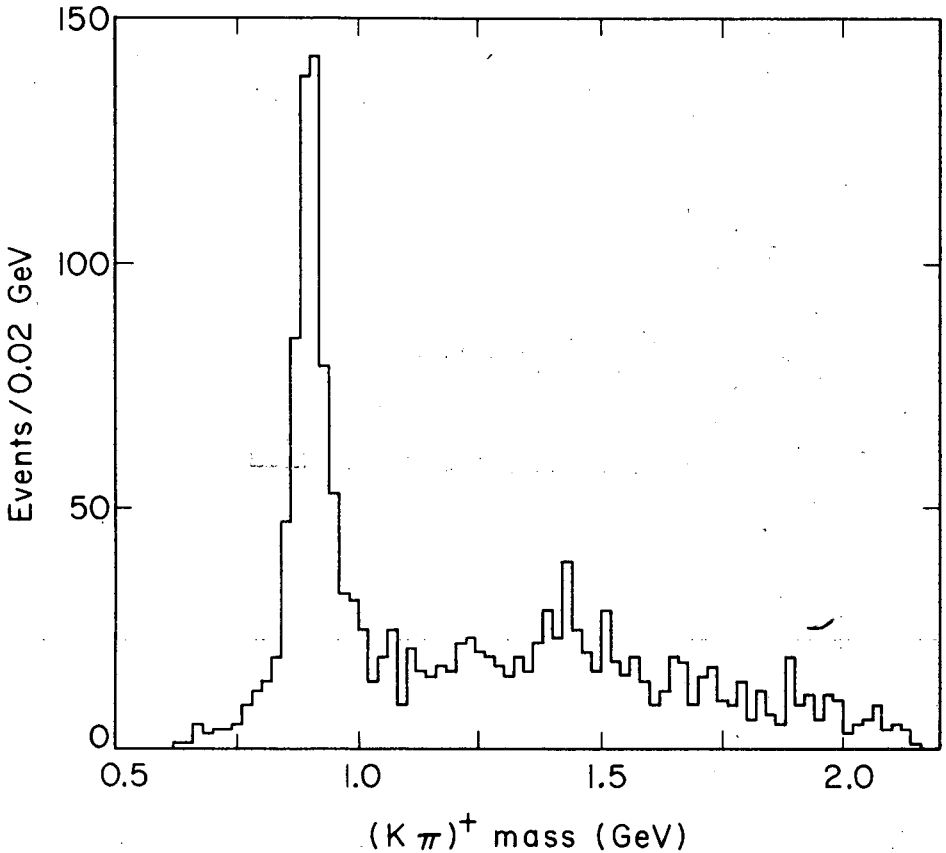

XBL706-3143

Fig. 8. Kπ mass spectrum for the event classes chosen as in Table VII, with $-t_p < 1.2$ $(GeV/c)^2$ and removal of events in the Δ^{++} band.

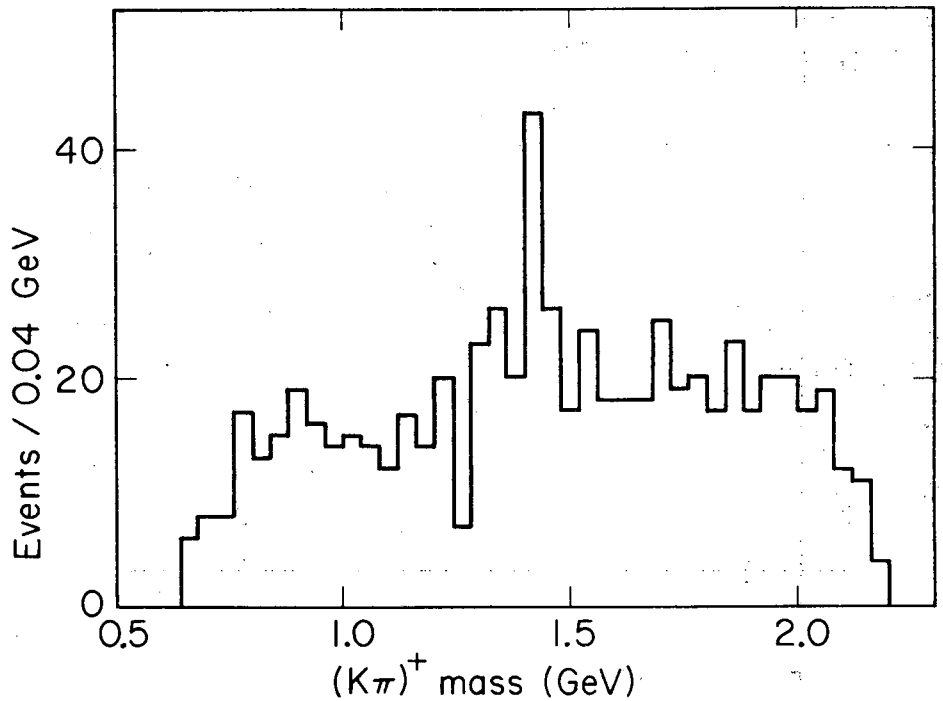

XBL709-3788

Fig. 9. Kπ mass spectrum for $-t_p > 1.2$ $(GeV/c)^2$. Events in the Δ^{++} band have been removed and ambiguities treated as discussed in the text.

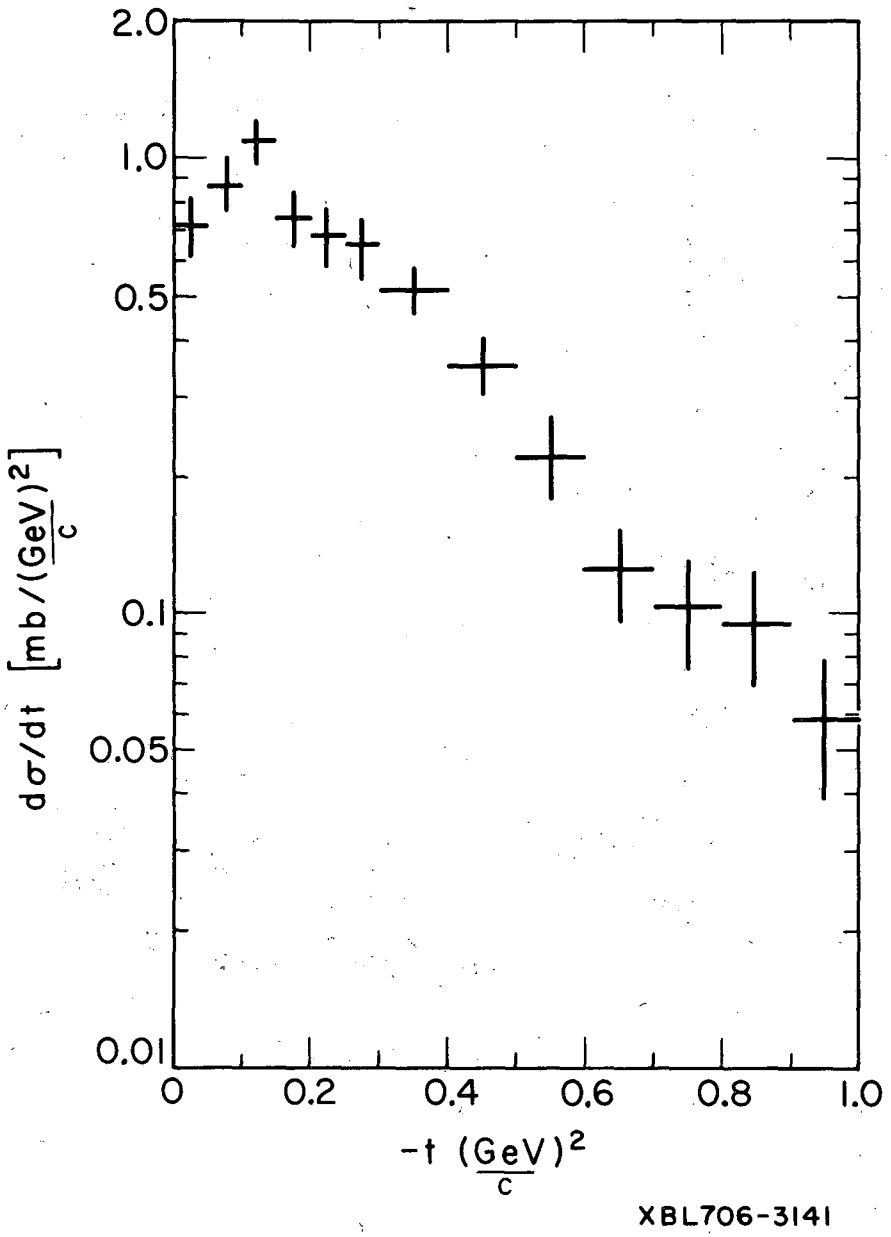

Fig. 10. Momentum-transfer distribution in the reaction $K^+p \rightarrow K^{*+}(891)p \rightarrow K^0\pi^+p$. Events have been selected just as for Fig. 5 and normalized to the cross section of 0.38 mb for the $K^0\pi^+p$ final state.

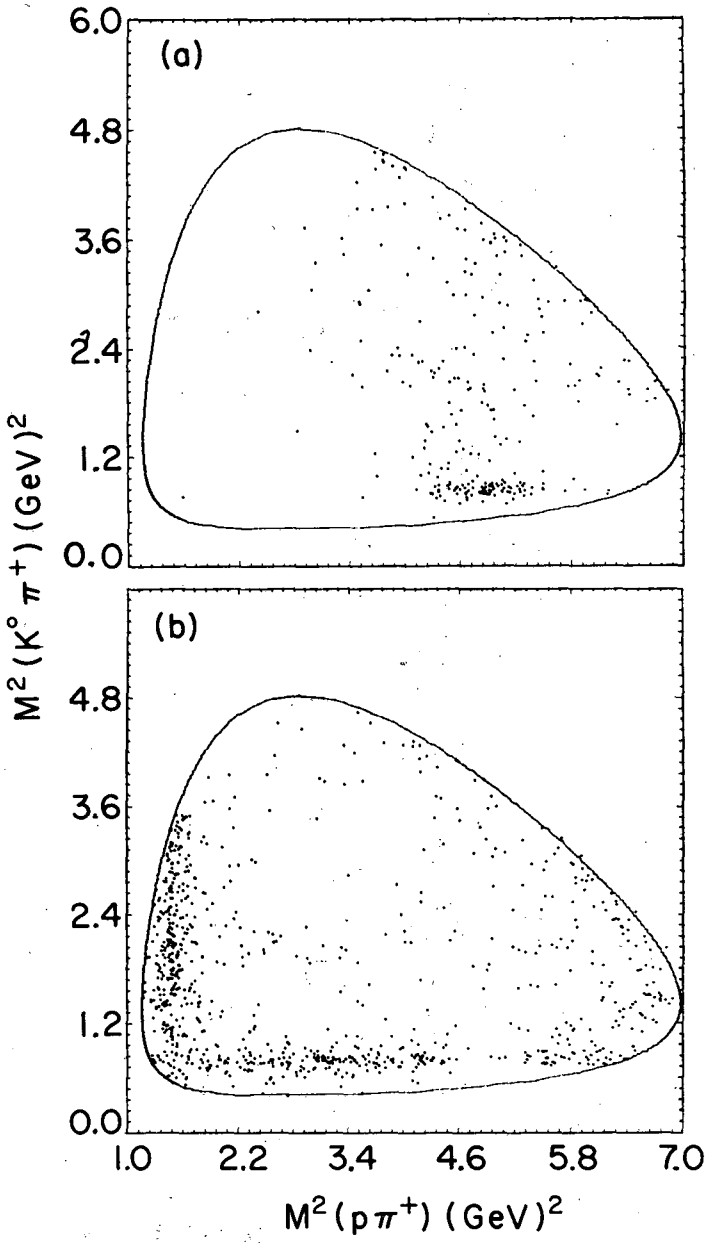

Fig. 11. Dalitz plots for a) ambiguous and b) unambiguous fits to the $K^0p\pi^+$ state. Only the two-prong events are plotted.

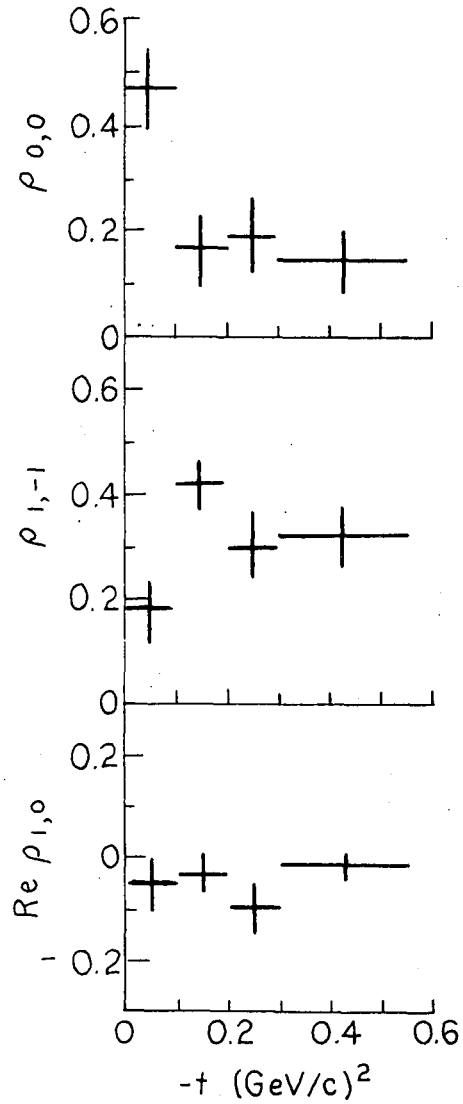

XBL706-3188A

Fig. 12. Density matrix elements for the $K^*(891)$ from the reaction $K^+p \rightarrow K^{*+}p$.

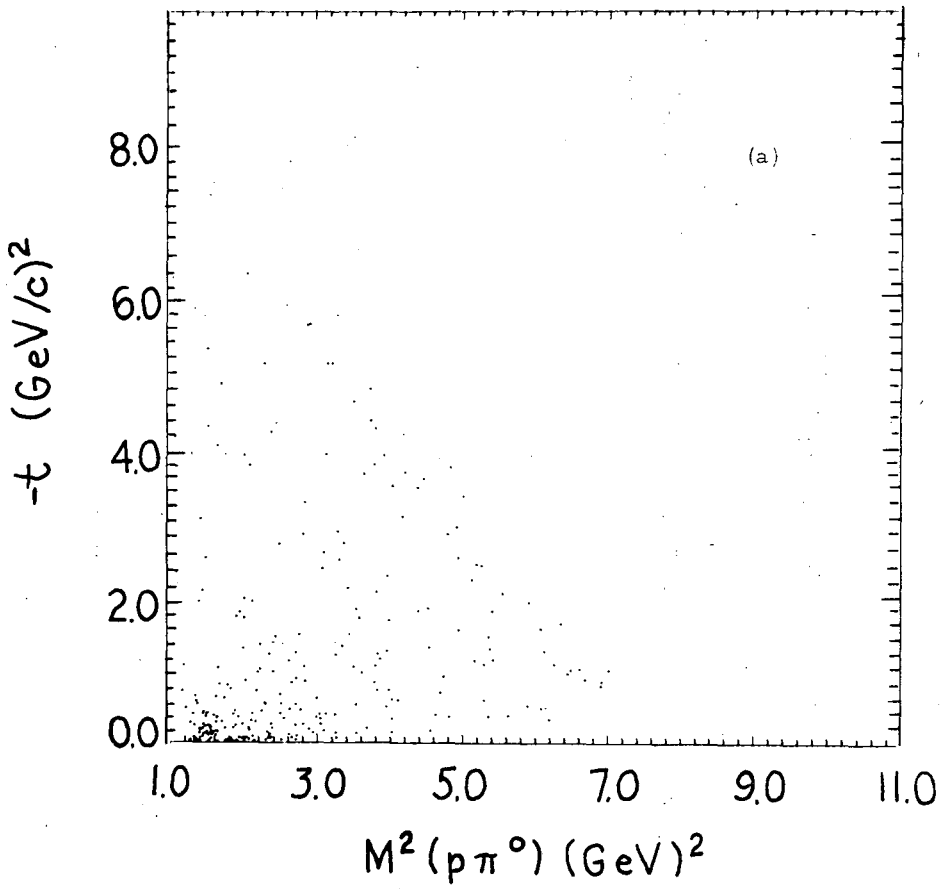

XBL 711-133

Fig. 13. Plot of $t_{p\pi}$ vs $m^2_{p\pi}$ for a) $K^+p\pi^0$ and b) $K^0p\pi^+$ final states.

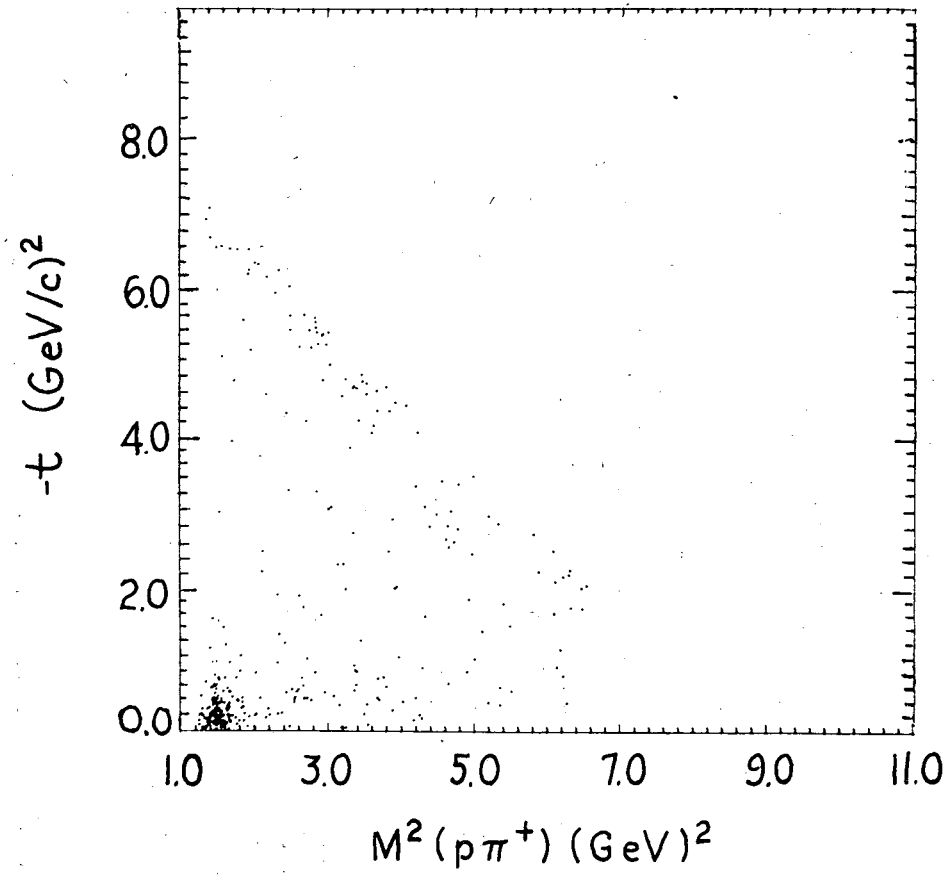

XBL 711-132

Fig. 13b.

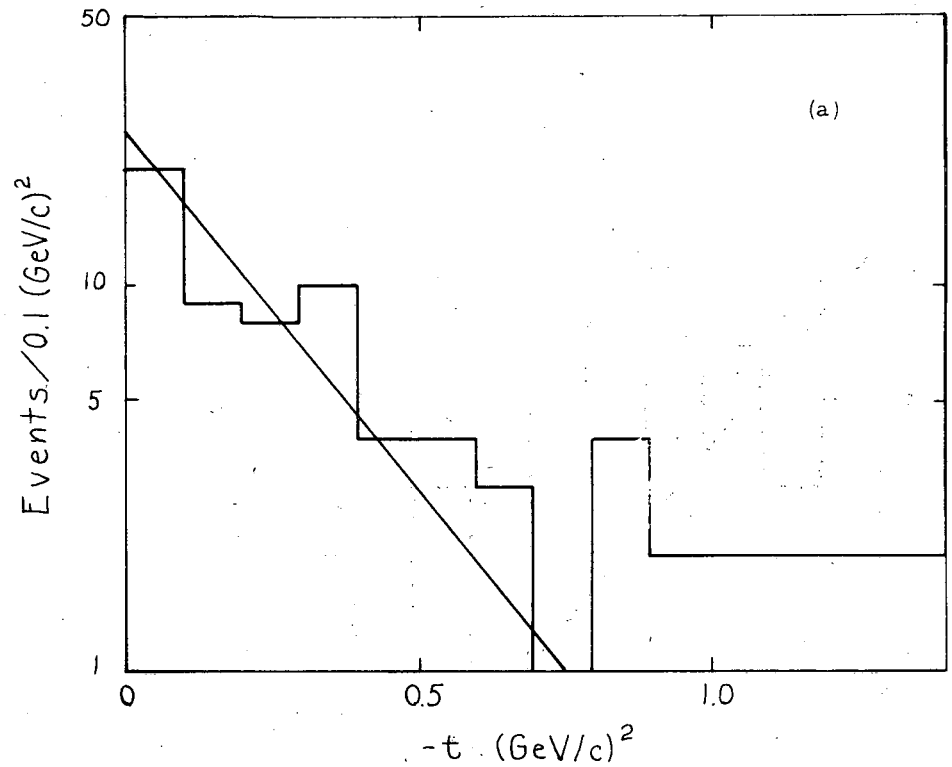

XBL 711-135

Fig. 14. t_K distribution for events satisfying conditions discussed in the text for a) $K^+p\pi^0$ and b) $K^0 p\pi^+$ final states. The straight line has the slope corresponding to $e^{-4.2t}$ which was the result for K^+p elastic scattering and is normalized to the number of events from $t = 0$ to $0.5\ (GeV/c)^2$.

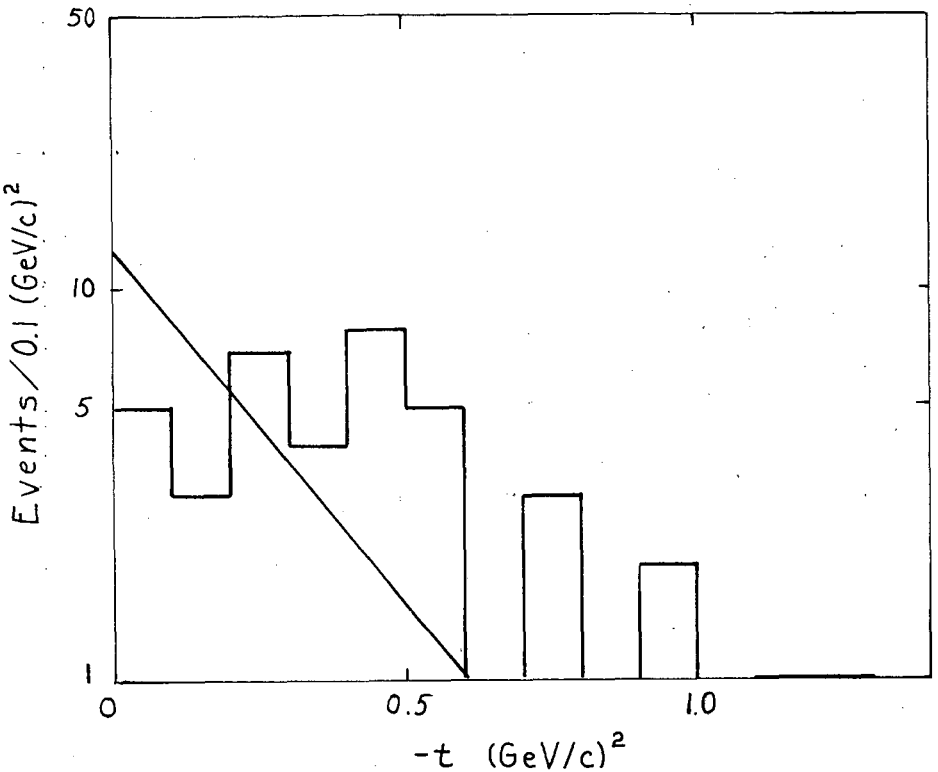

Fig. 14b

XBL 711-134

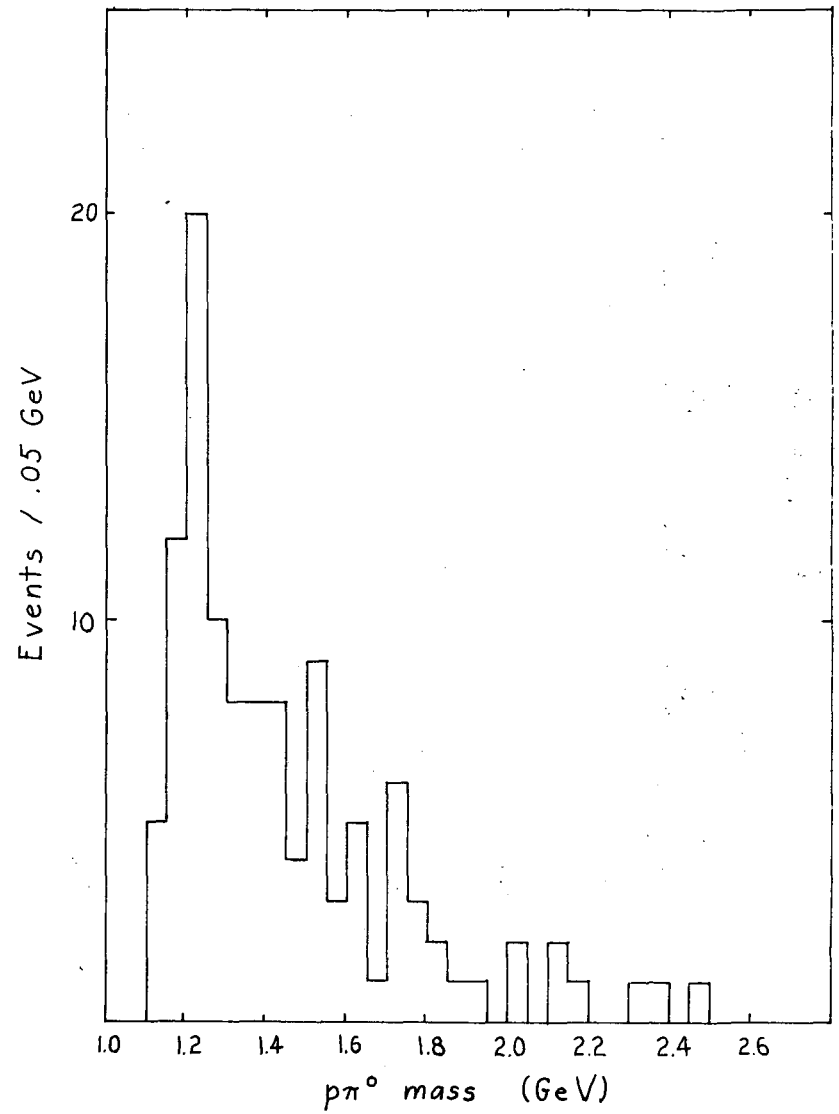

XBL 711-138

Fig. 15. $p\pi^0$ mass spectrum for the $K^+p\pi^0$ final state satisfying selection criteria discussed in the text.

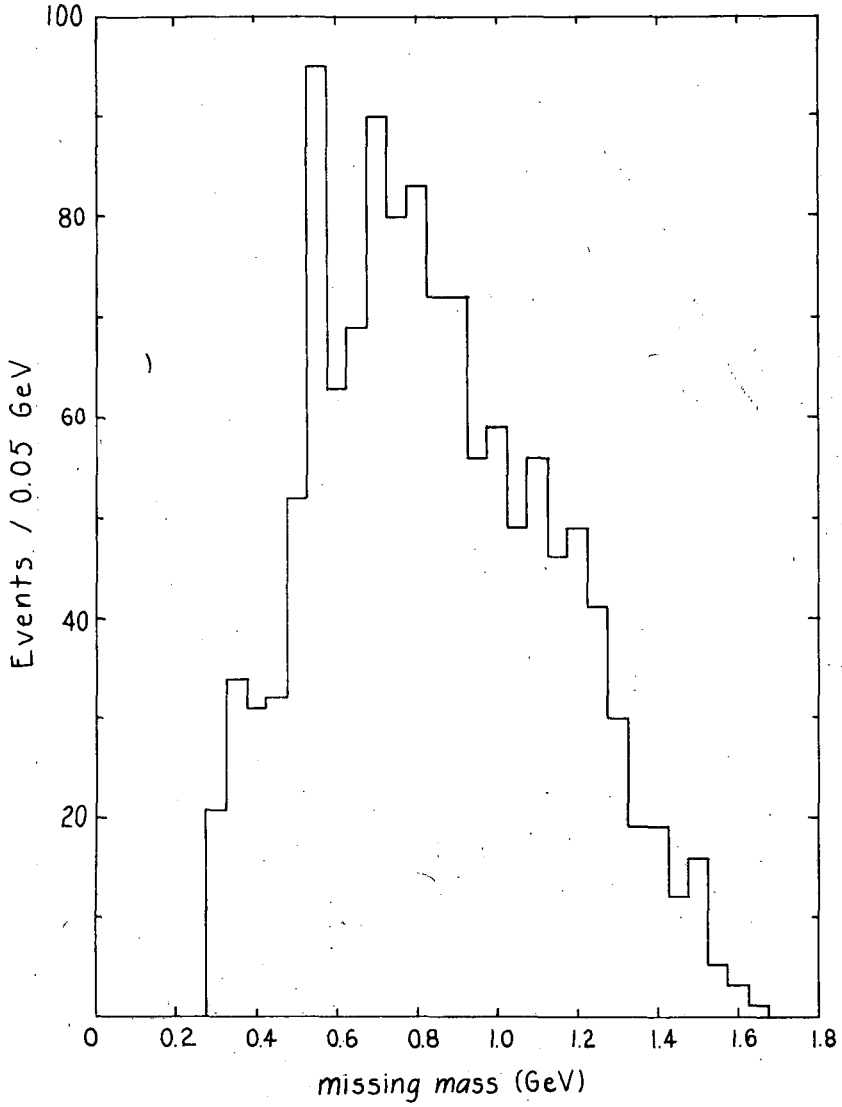

XBL 711-137

Fig. 16. Missing-mass spectrum for the final state K^+pMM.

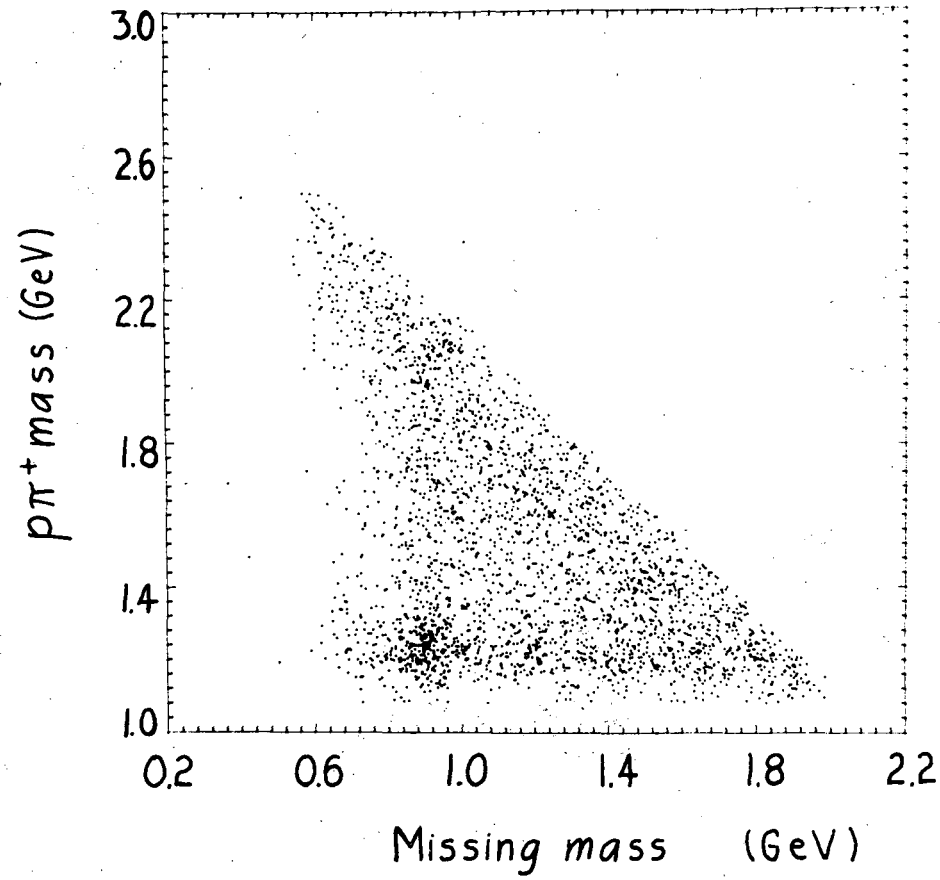

XBL 711-131

Fig. 17. Scatter plot of $p\pi^+$ mass vs. missing mass for the final state π^+pMM.

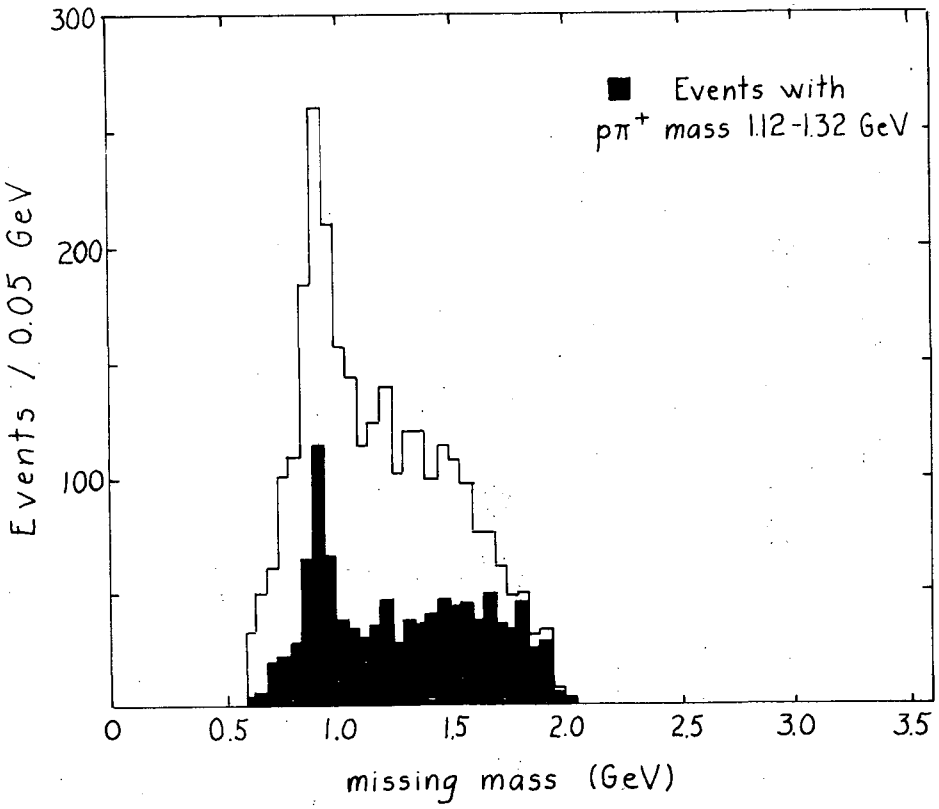

XBL 711-136

Fig. 18. Missing-mass spectrum for the final state π^+pMM. The shaded events have $p\pi^+$ mass 1.12-1.32 GeV.

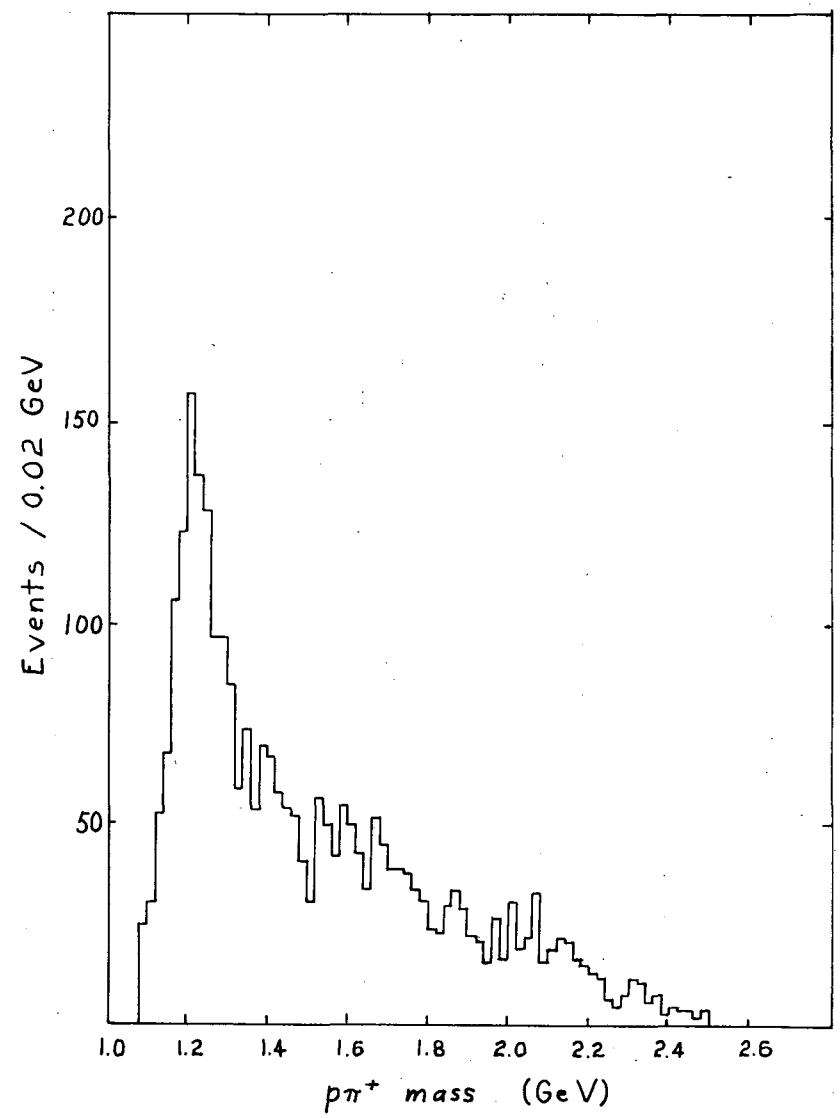

XBL 711-140

Fig. 19. $p\pi^+$ mass spectrum for the final state $p\pi^+$MM.

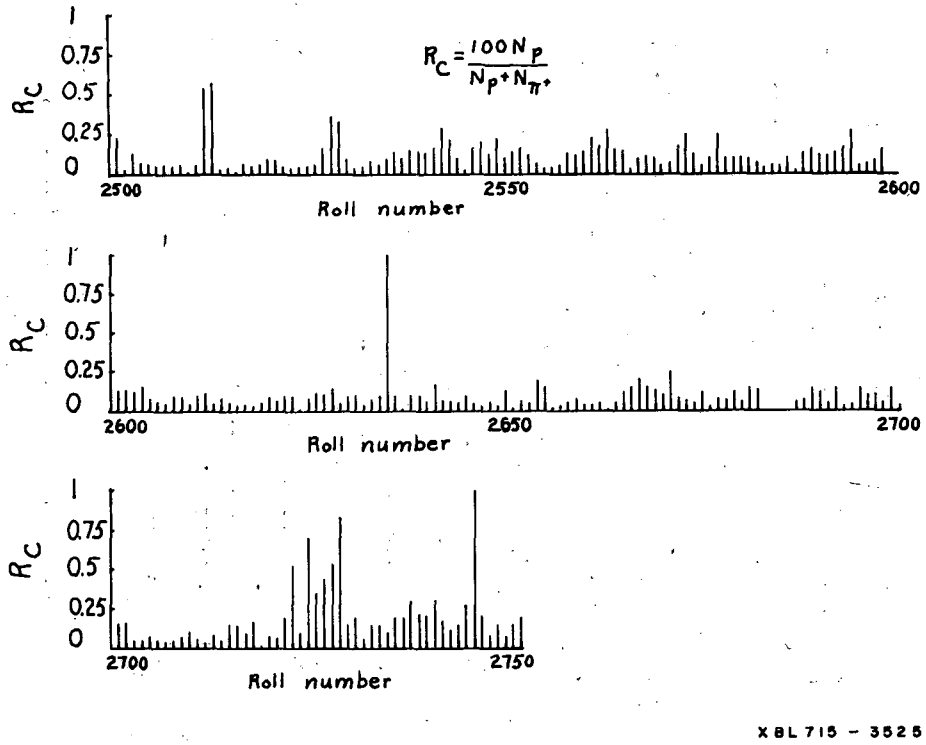

Fig. 20. Plot of $\frac{100N_p}{N_\pi + N_p}$ vs. roll number.

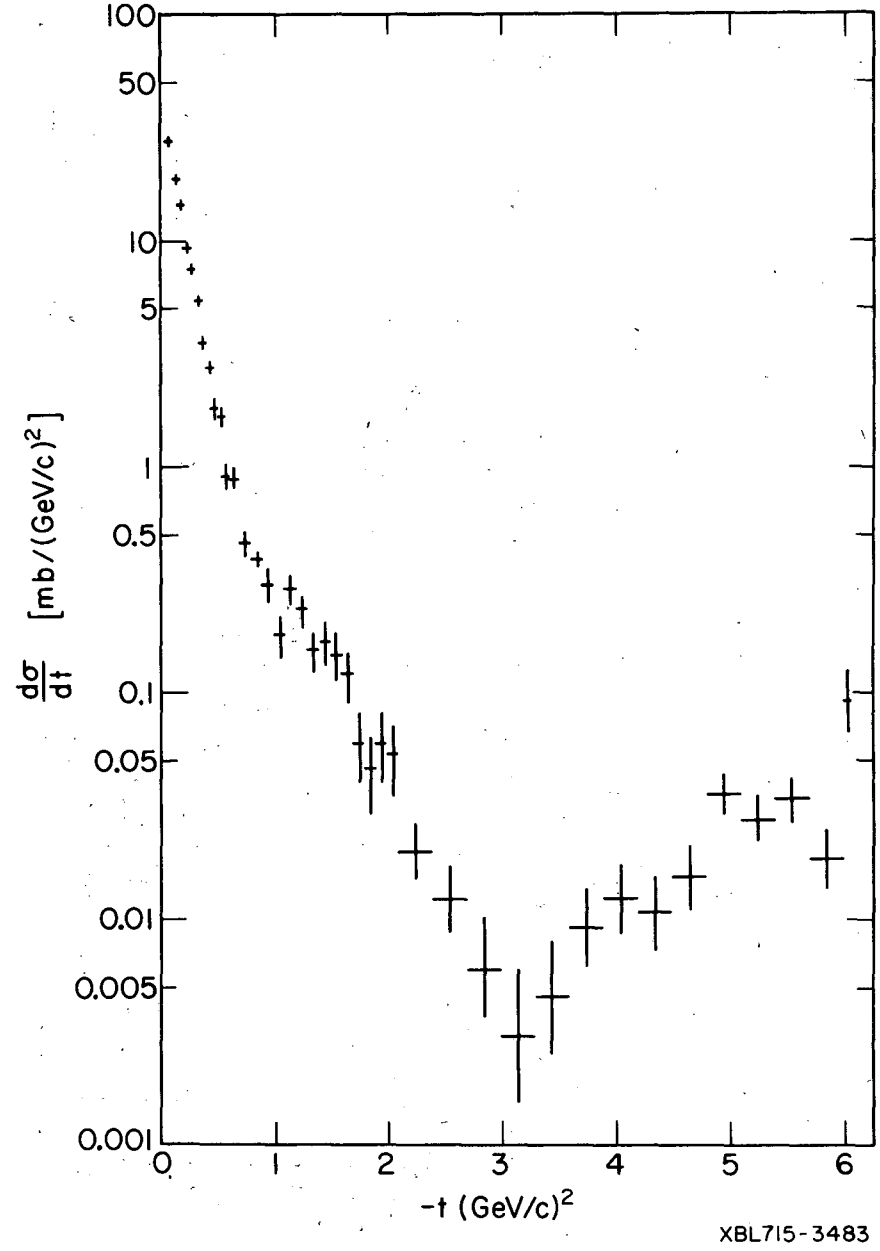

Fig. 21. Differential cross section, $\frac{d\sigma}{dt}$, for π^+p elastic scattering at 3.6 GeV/c for $t > 0.05$ (GeV/c)^2.

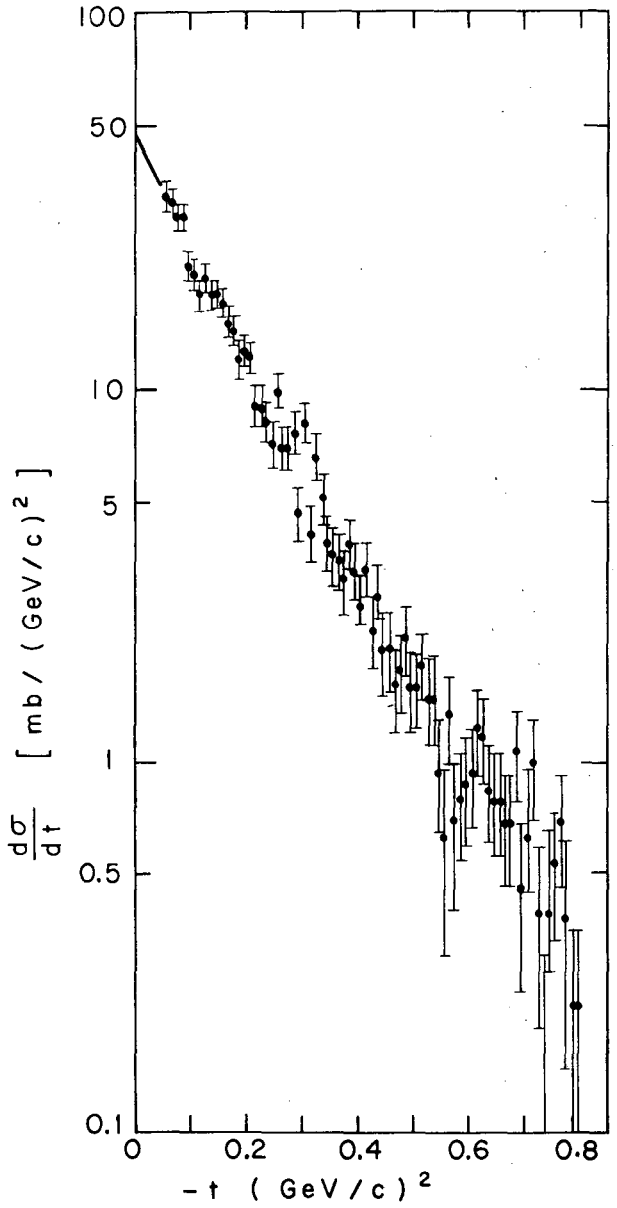

XBL715 - 3443

Fig. 22. Elastic-scattering differential cross section in terms of momentum transfer squared for forward angles. The solid line is a linear extrapolation to t = 0.

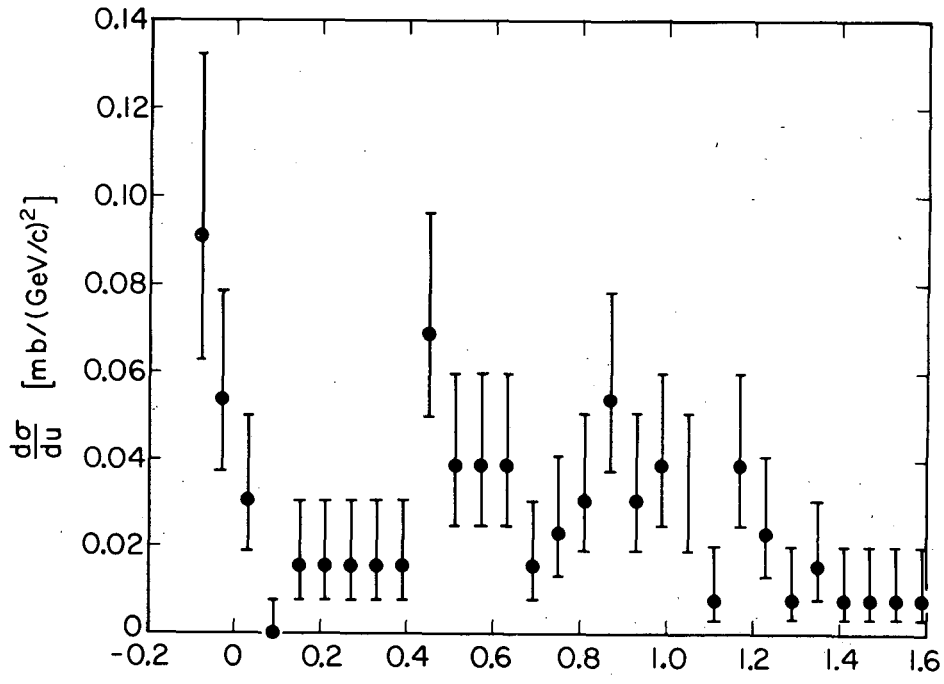

XBL715-3482

Fig. 23. Elastic-scattering differential cross section in terms of baryon exchange momentum transfer squared for backward angles.

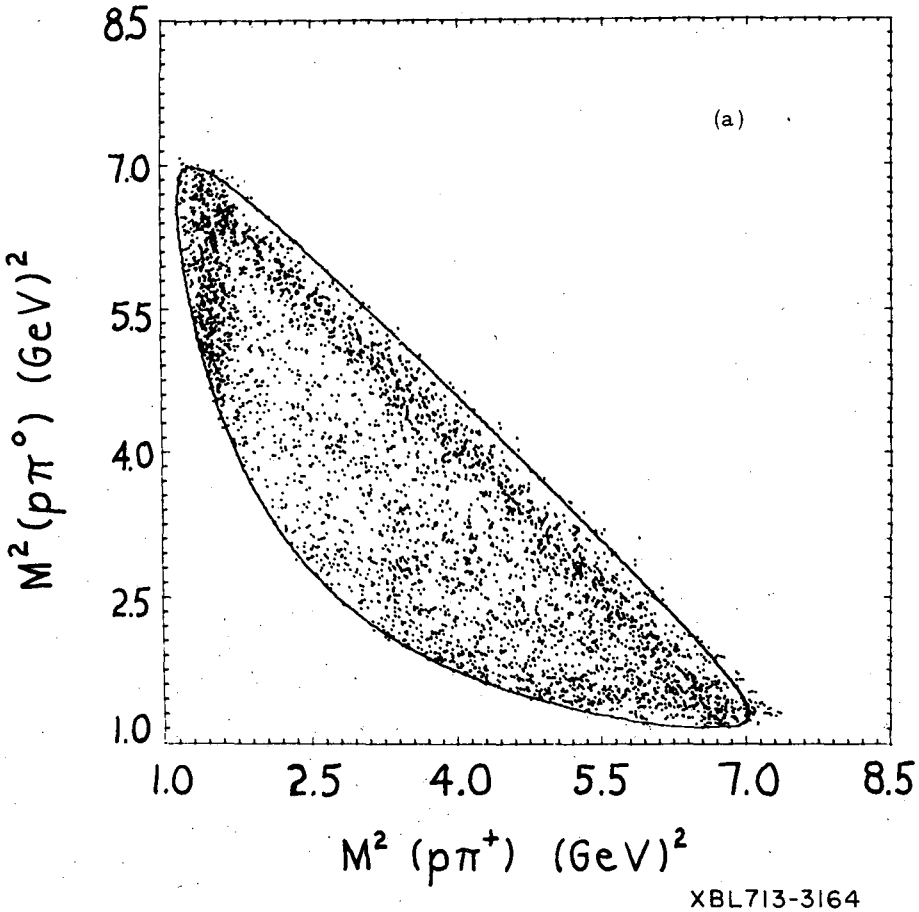

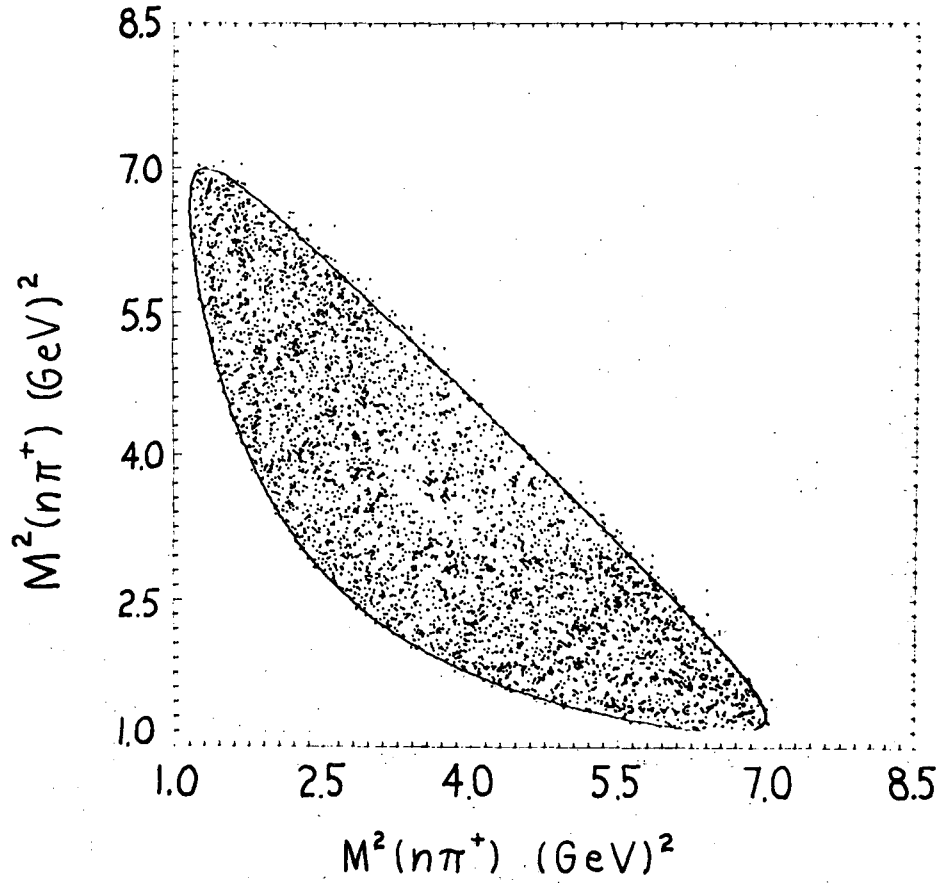

Fig. 24b

Fig. 24. Dalitz plots for final states a) $p\pi^+\pi^0$ and b) $n\pi^+\pi^+$.

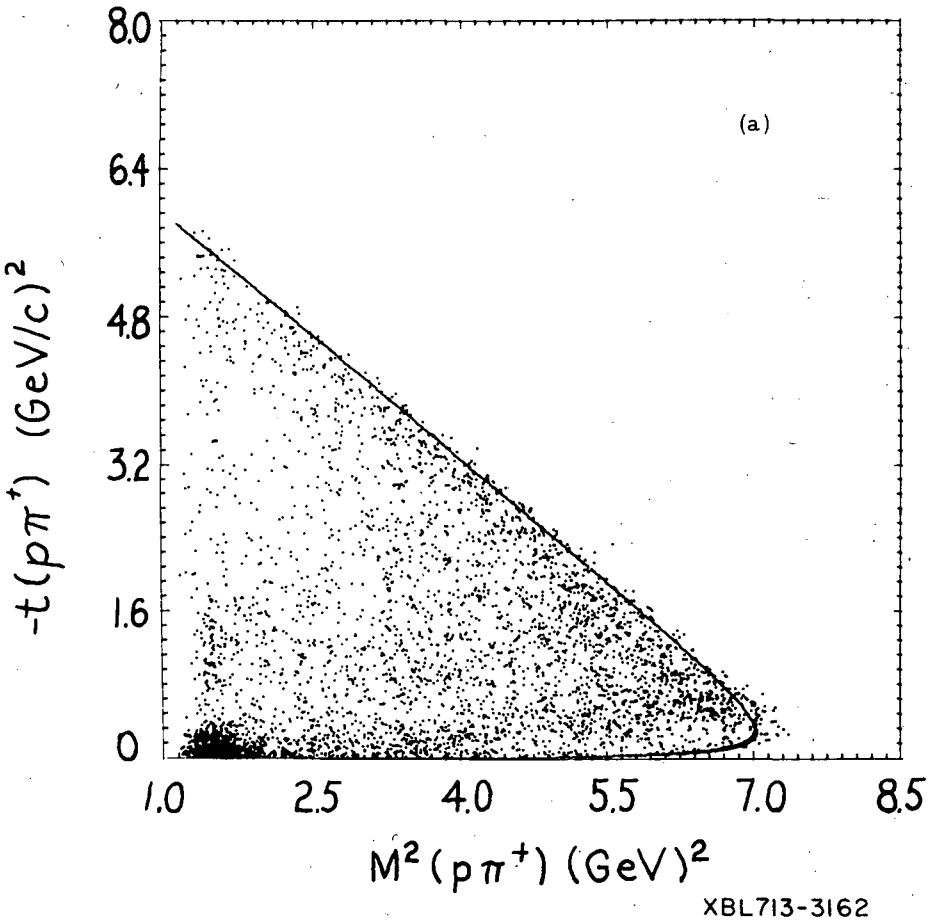

Fig. 25. Scatter plot of momentum transfer squared vs. effective mass squared for a) $p\pi^+$, b) $p\pi^0$, c) $\pi^+\pi^0$, d) $n\pi^+$, and e) $\pi^+\pi^+$.

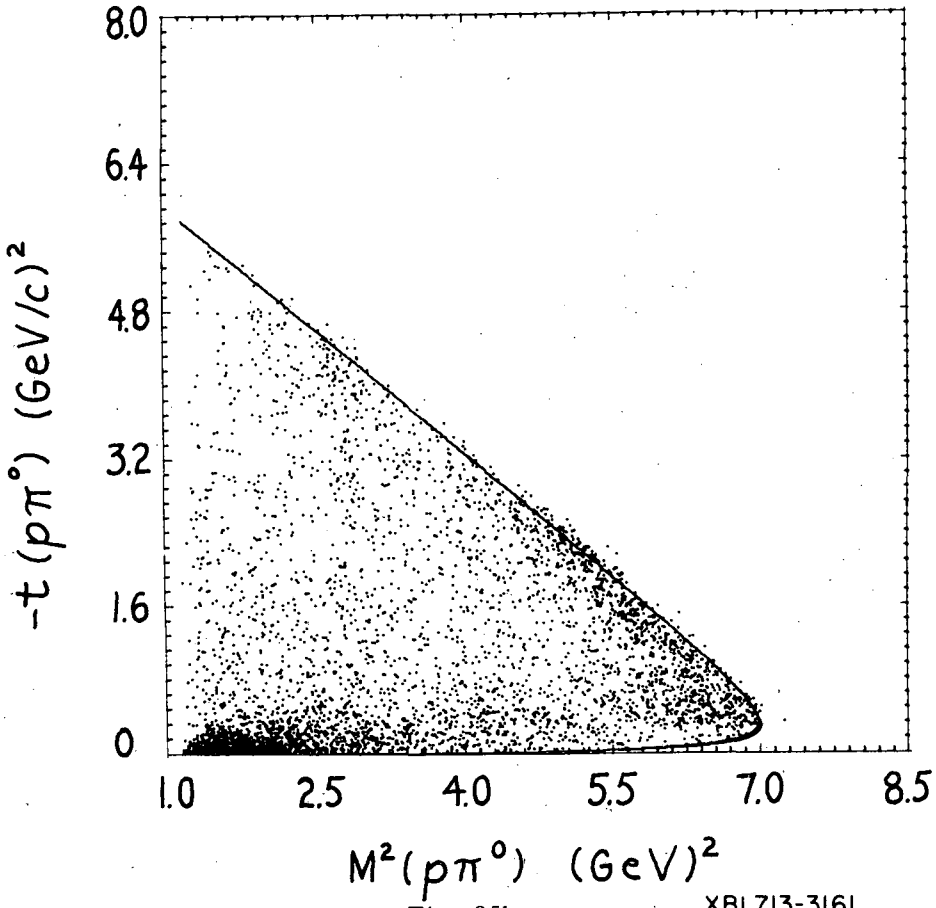

Fig. 25b.

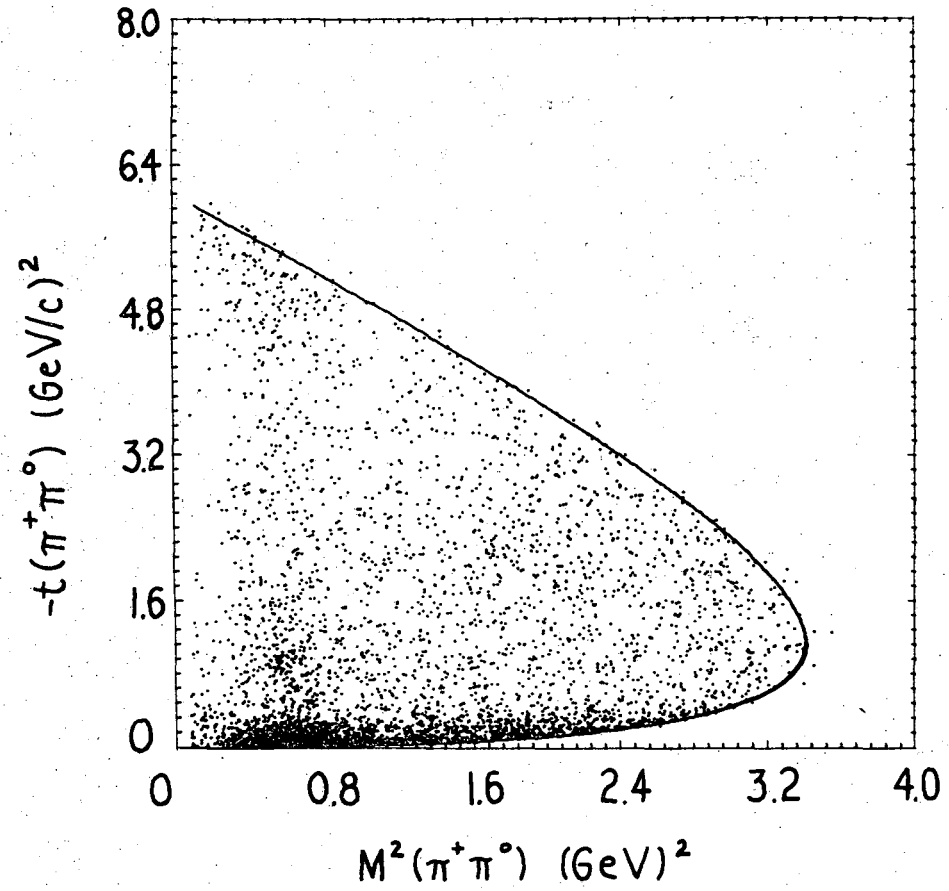

Fig. 25c. XBL713-3160

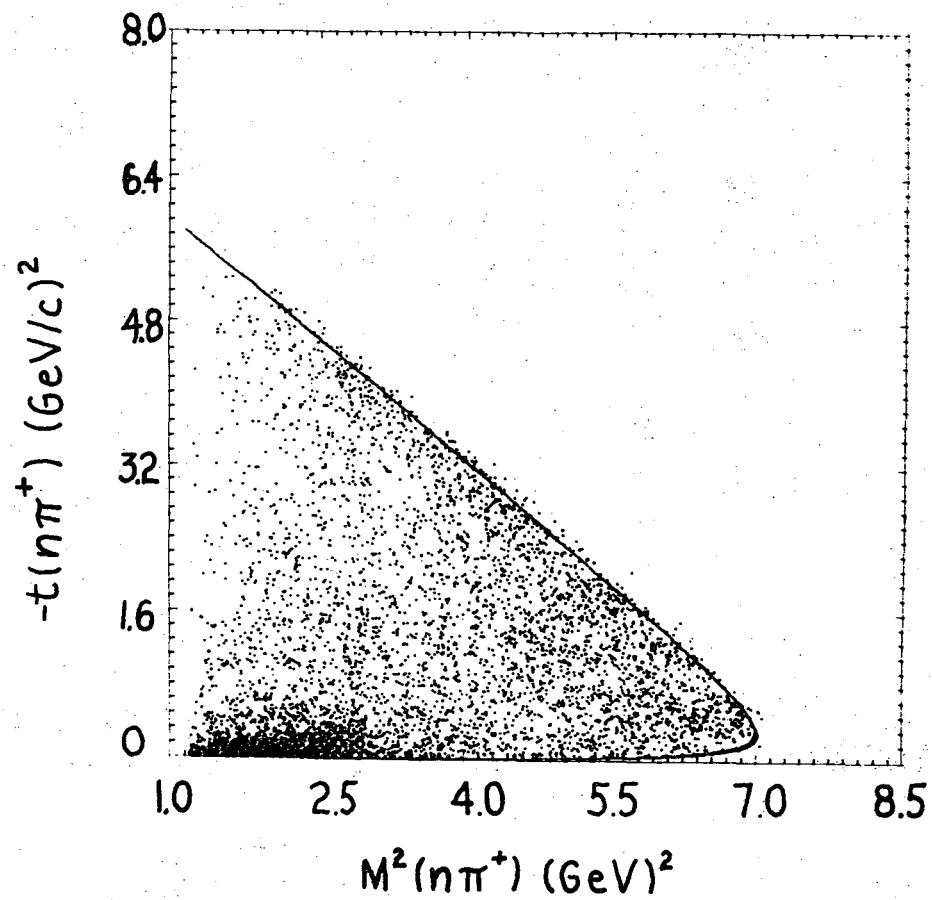

Fig. 25d. XBL713-3165

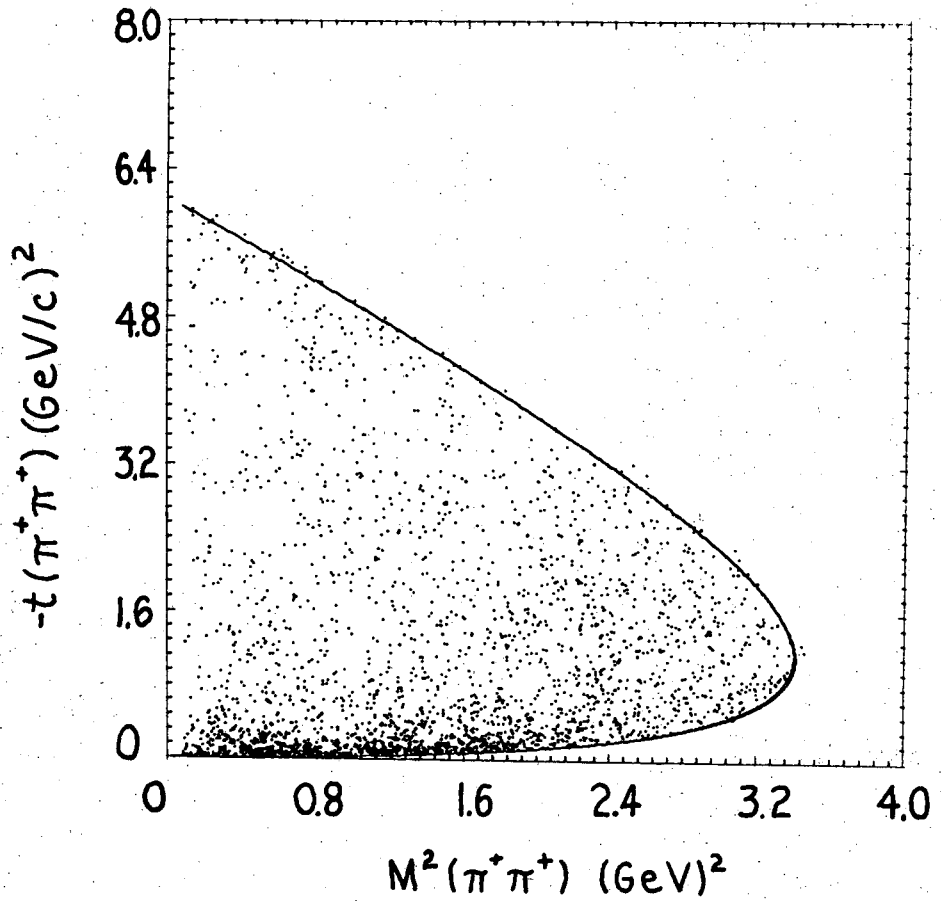

Fig. 25e. XBL713-3159

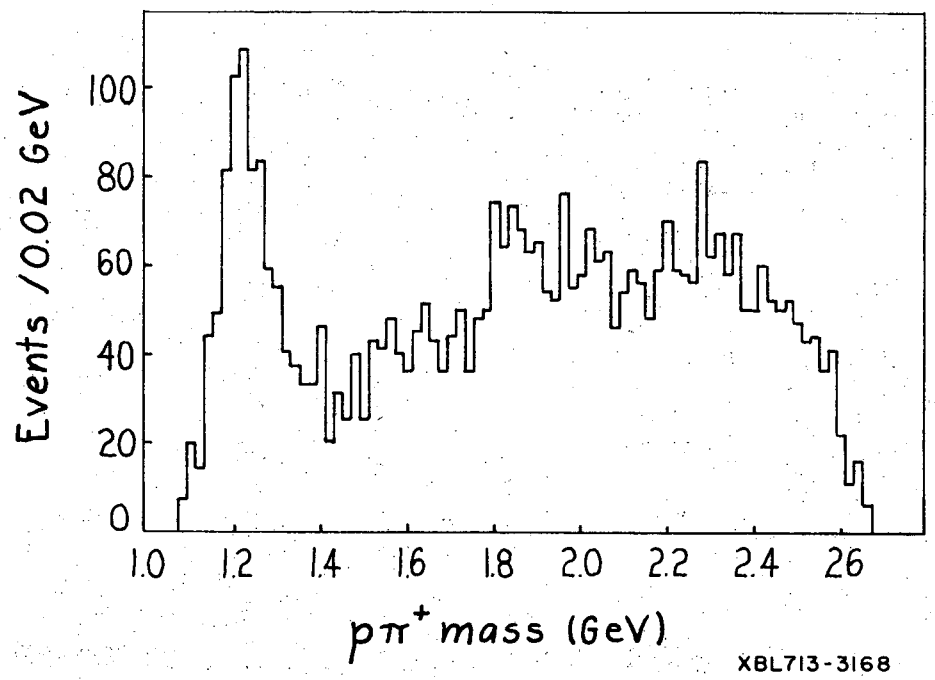

Fig. 26. $p\pi^+$ mass spectrum in the final state $p\pi^+\pi^0$.

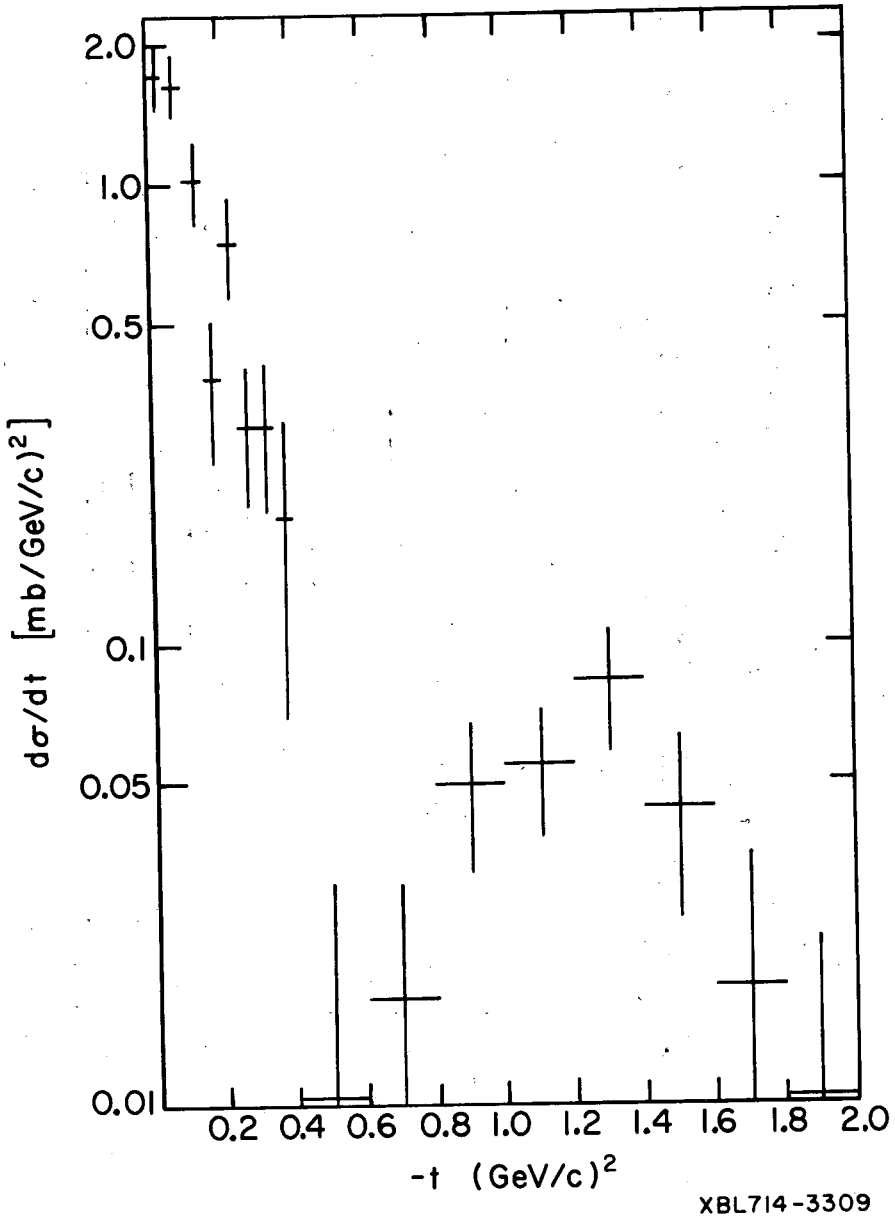

Fig. 27. Momentum transfer distribution in the reaction $\pi^+ p \rightarrow \pi^0 \Delta^{++}$.

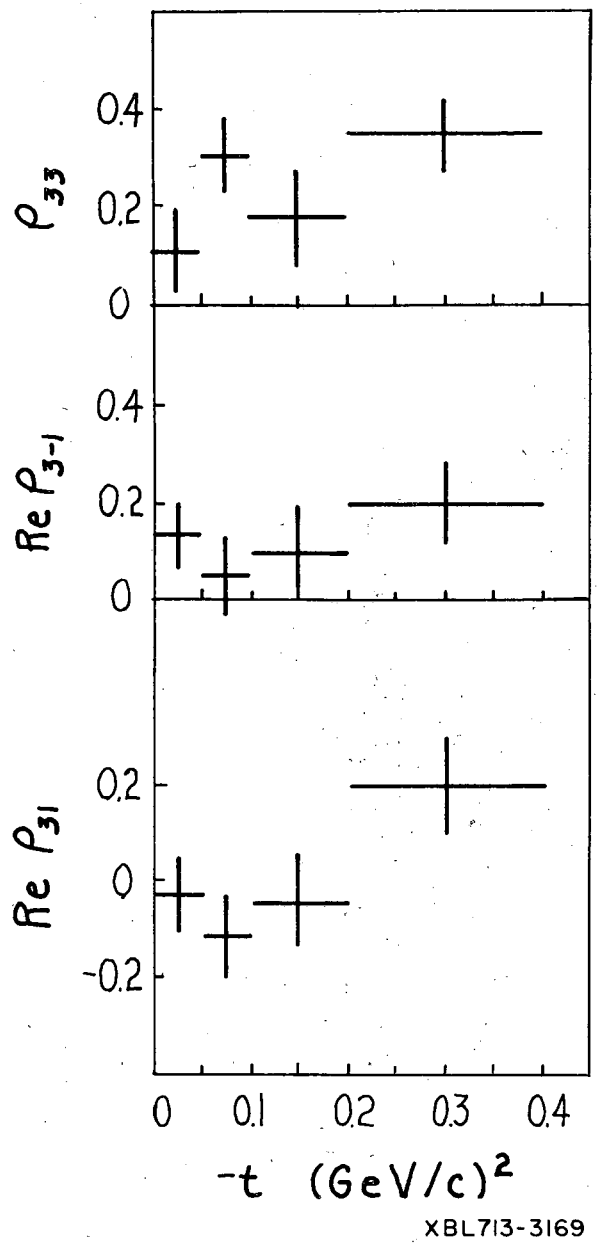

Fig. 28. Density matrix elements for the Δ from the reaction $\pi^+ p \rightarrow \pi^0 \Delta^{++}$. Only events with $\cos \alpha < 0$ are used.

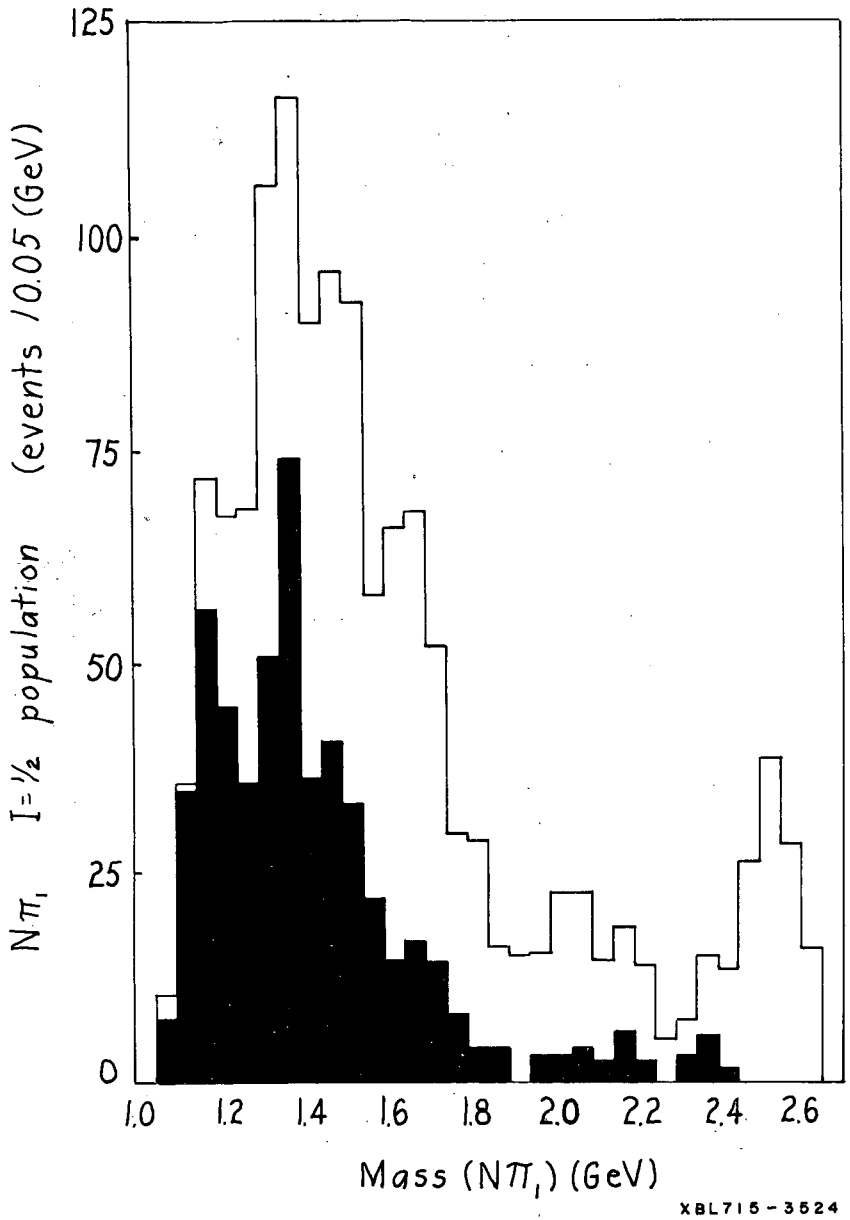

Fig. 29. Mass distribution of the quantity $(n\pi^+)+(p\pi^0)-2/3\ (p\pi^+)$ for $t < 0.4\ (\mathrm{GeV})^2$ and $\cos\lambda$ greater than -0.5. Shaded events have $t < 0.1\ (\mathrm{GeV})^2$.

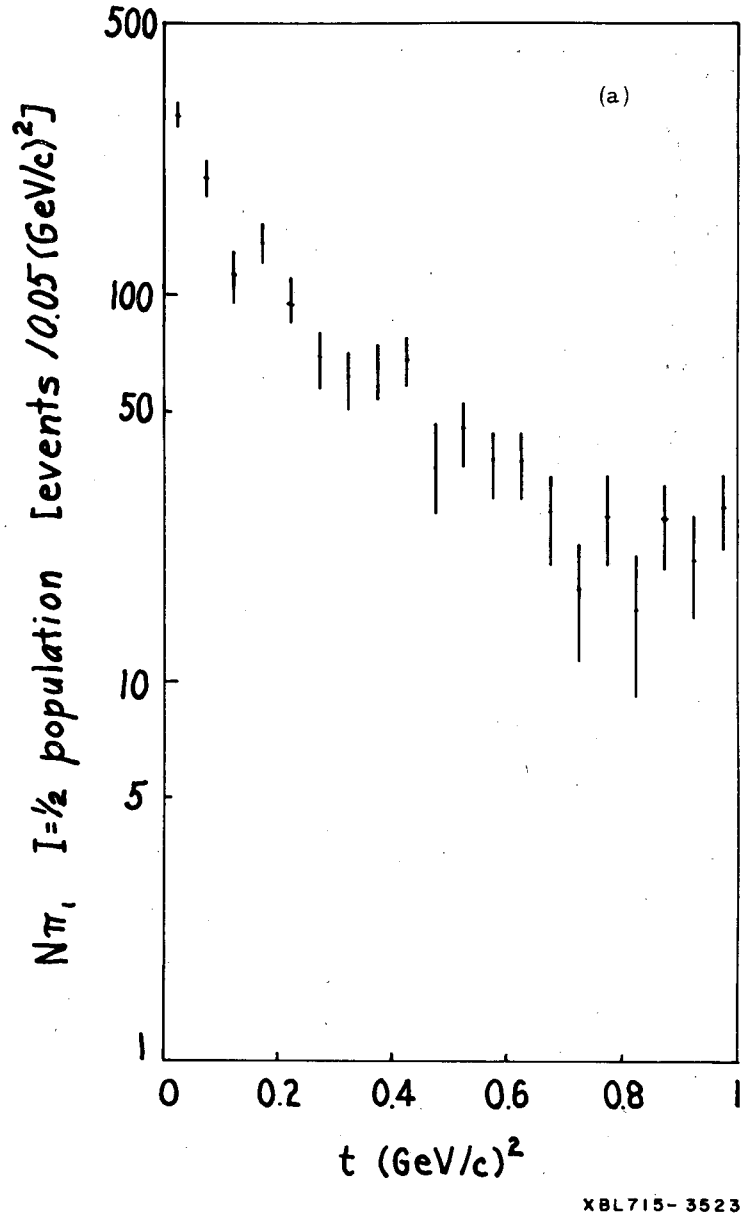

Fig. 30. t distribution of the quantity $(n\pi^+)+(p\pi^0)-2/3(p\pi^+)$ for $\cos\lambda$ greater than -0.5 and a) $m_{N\pi_1} < 1.8$ GeV; b) $m_{N\pi_1} < 1.3$ GeV; c) $m_{N\pi_1}$, 1.3-1.5 GeV; and d) $m_{N\pi_1}$, 1.5-1.8 GeV.

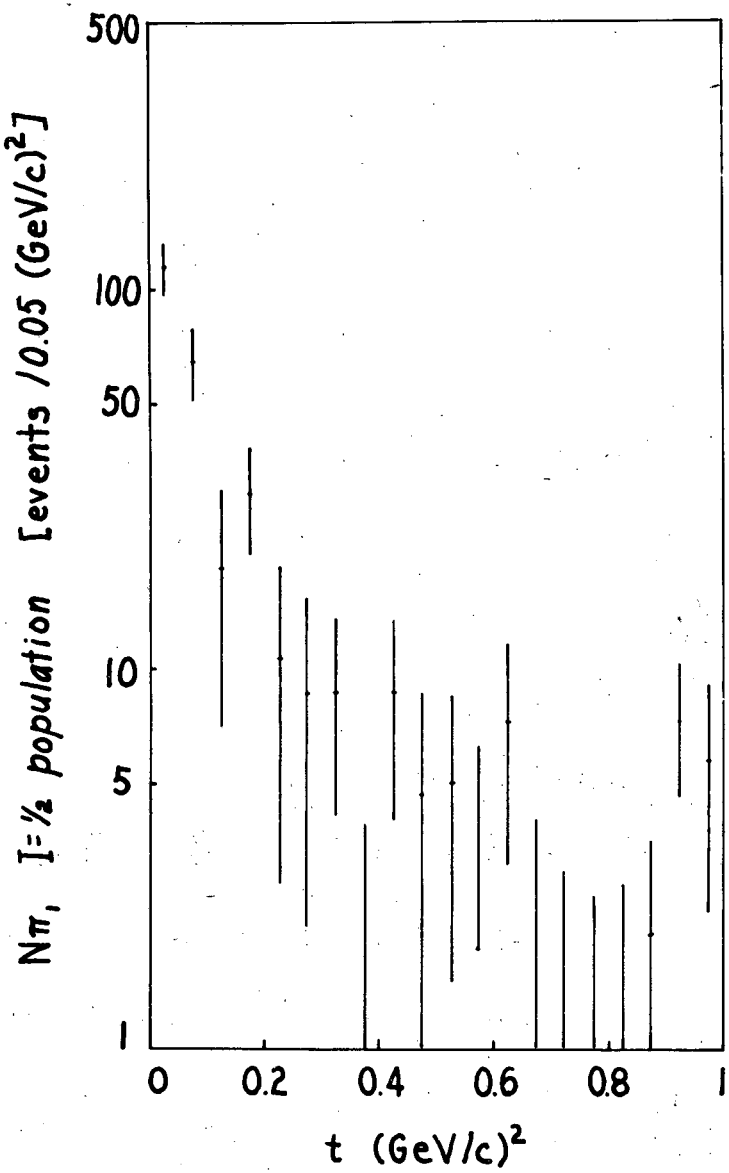

Fig. 30b. XBL715-3522

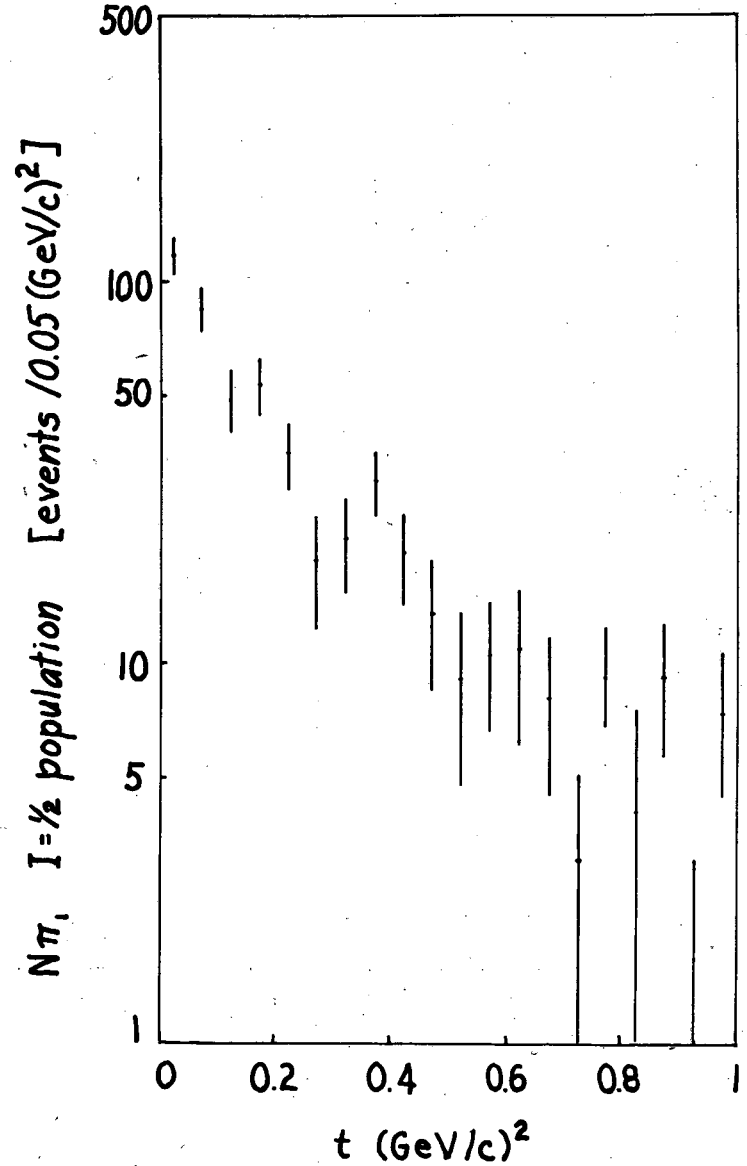

Fig. 30c. XBL715-3521

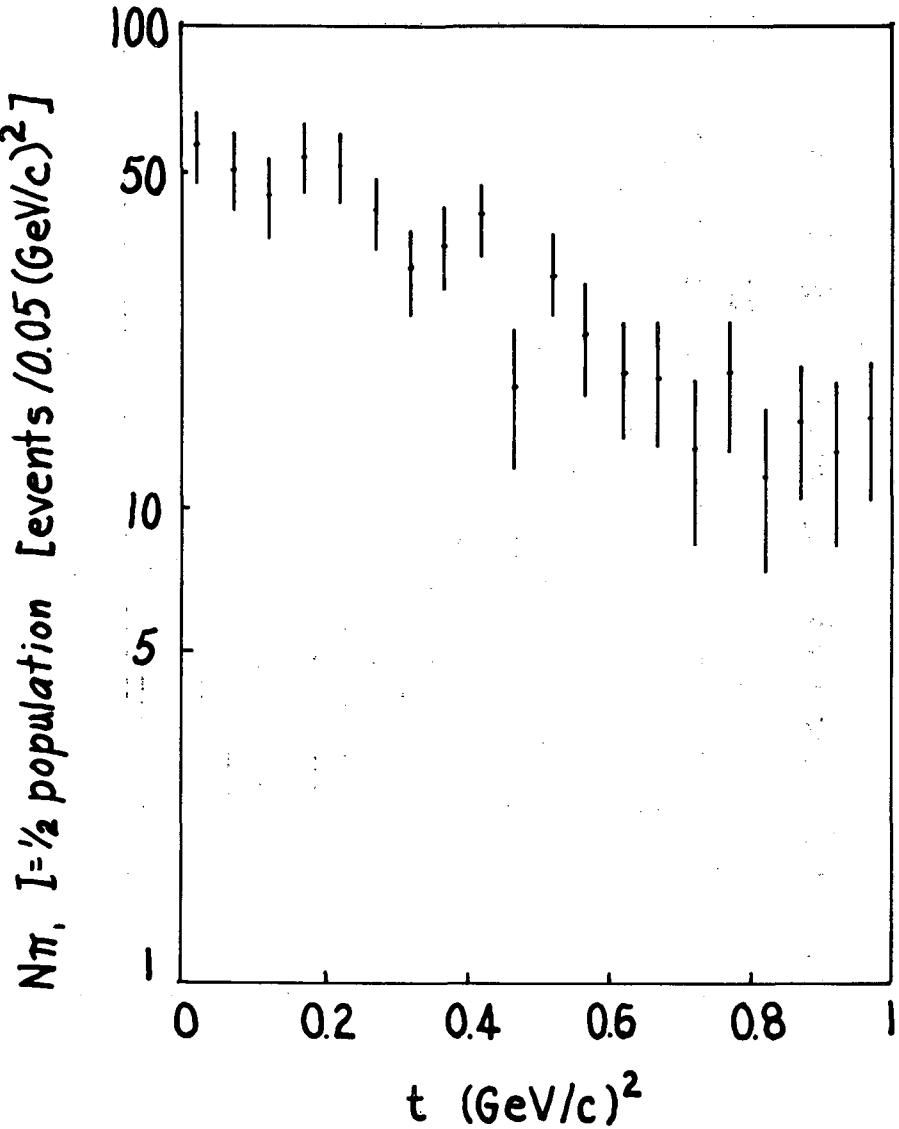

Fig. 30d.

XBL715-3520

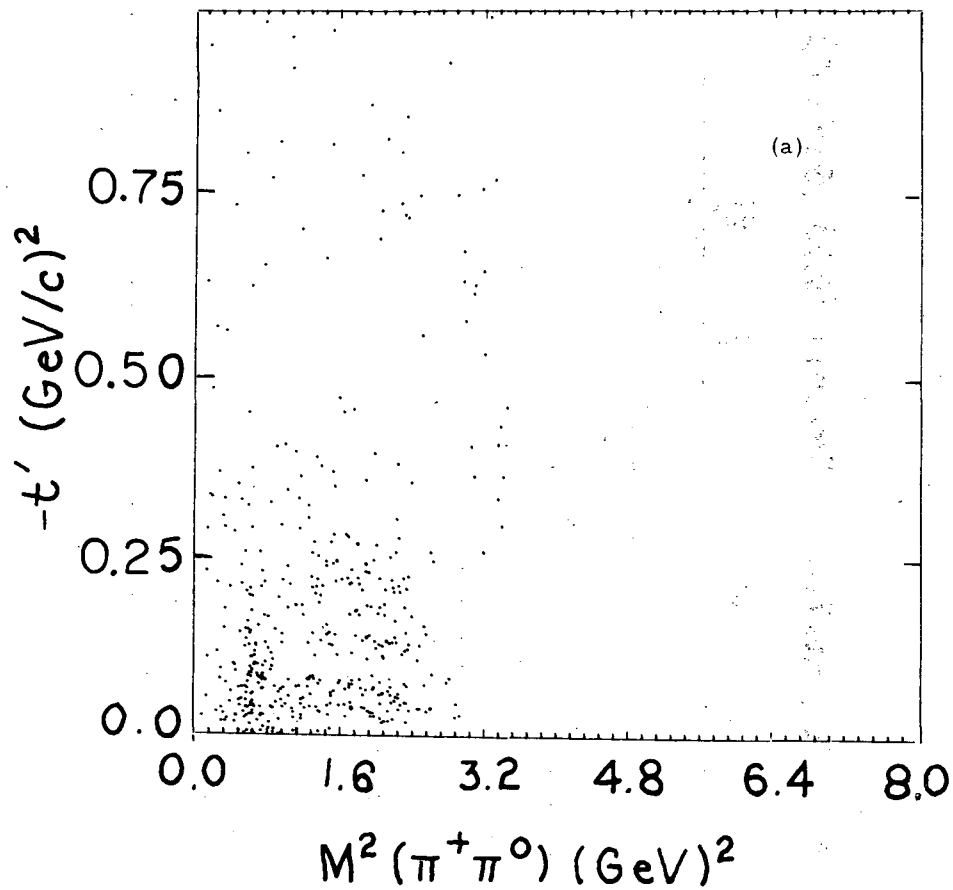

XBL711-2536

Fig. 31. Scatter plot of t vs $\pi^+\pi^0$ mass squared for various cos α regions:
a) -1 -0.8, b) -0.8 -0.6, c) -0.6 -0.4, d) -0.4 -0.2, e) -0.2-0
f) 0 -0.2, g) 0.2 -0.4, h) 0.4 -0.6, i) 0.6 -0.8, j) 0.8 -1.0.

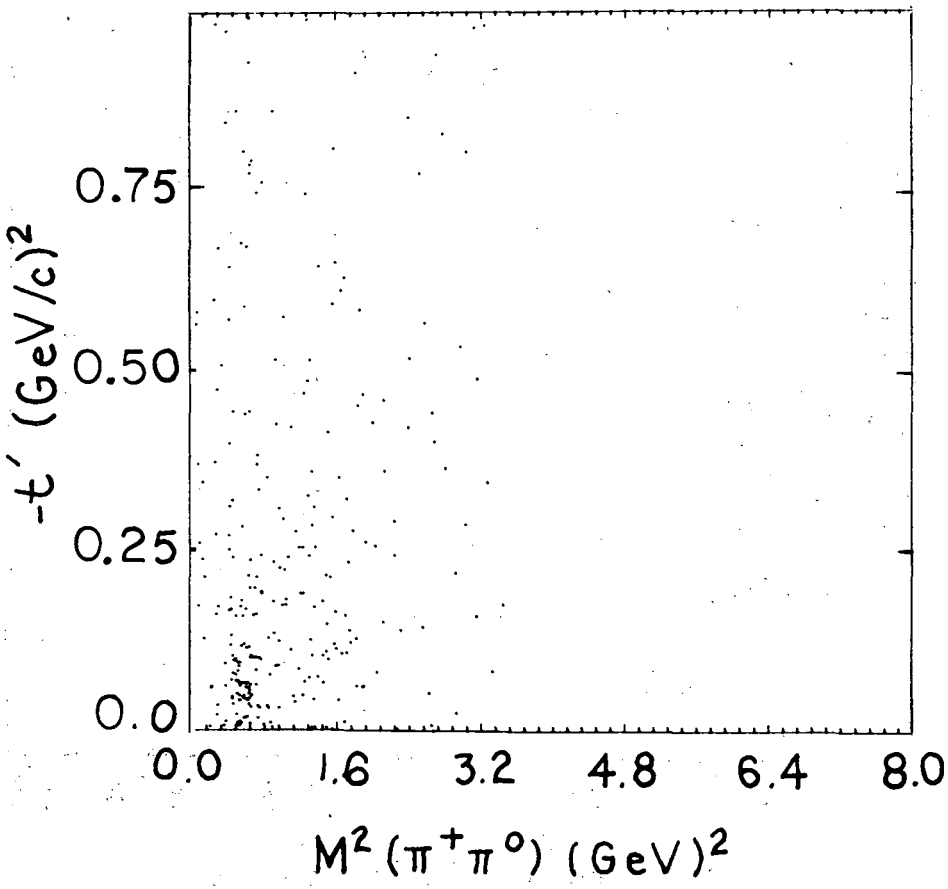

Fig. 31b. XBL711-2535

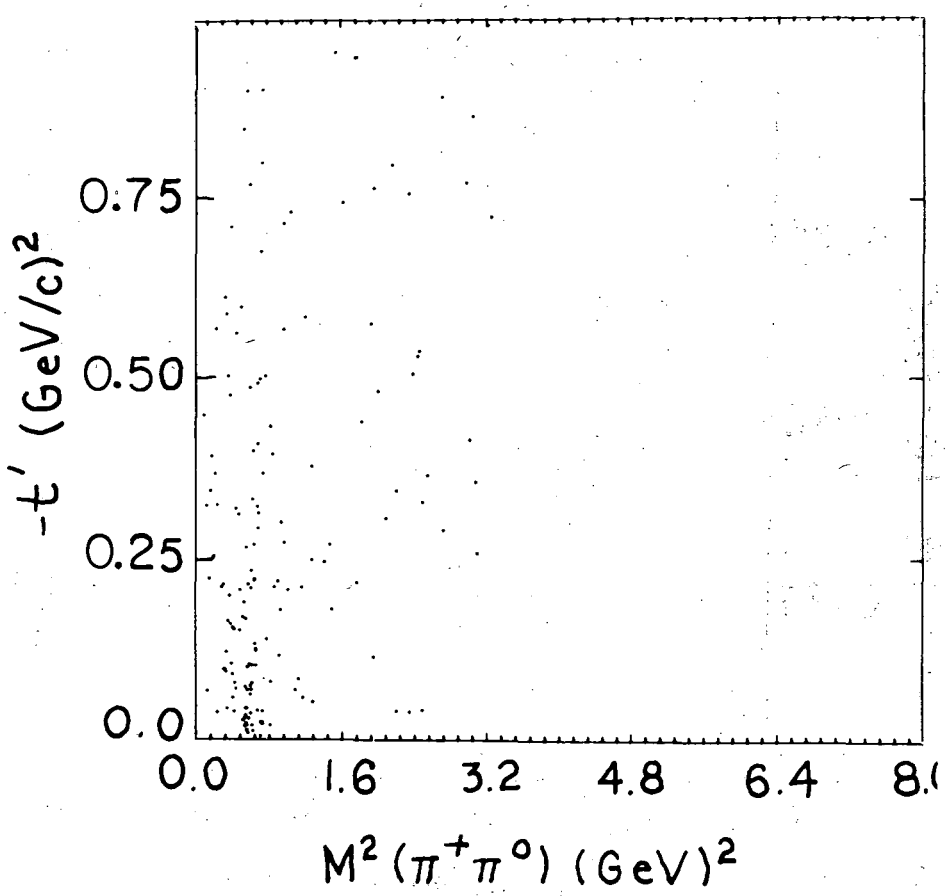

Fig. 31c. XBL711-2534

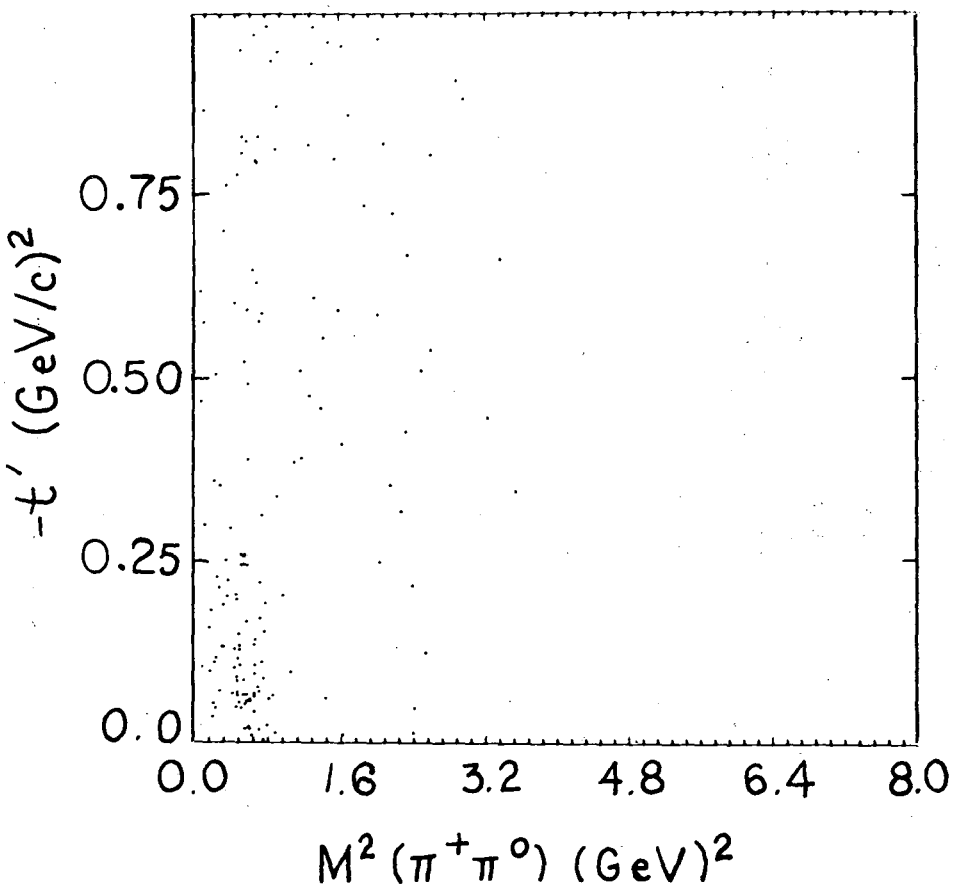

Fig. 31d. XBL711-2533

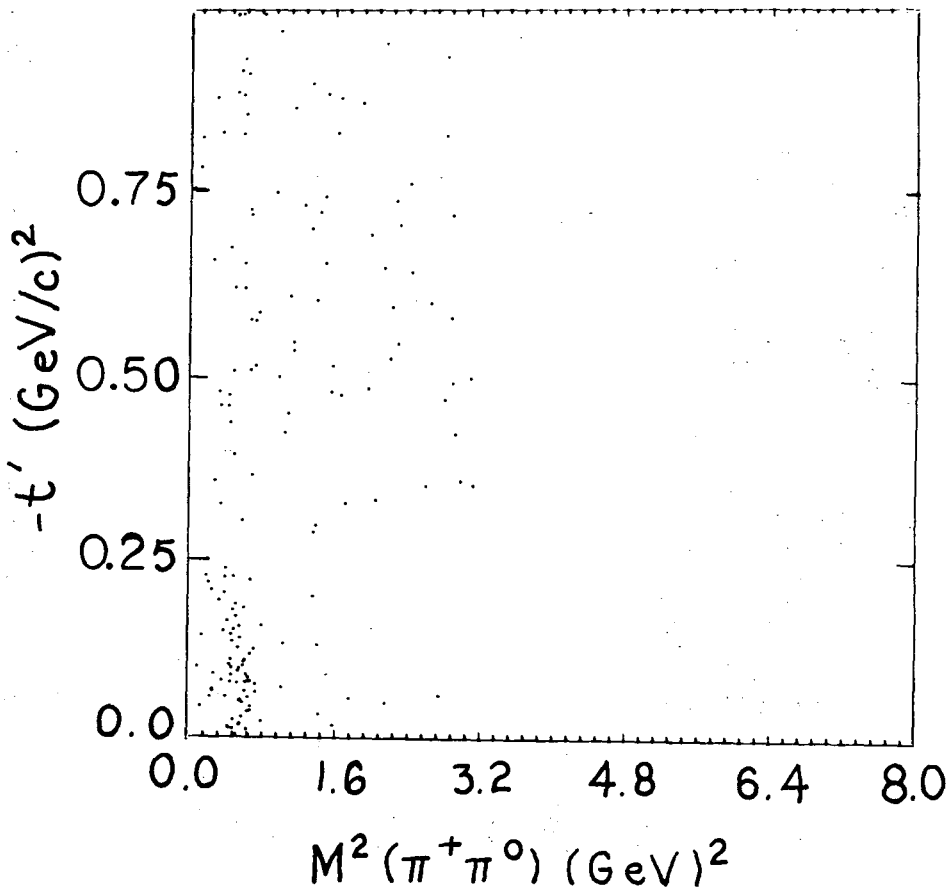

Fig. 31e. XBL711-2532

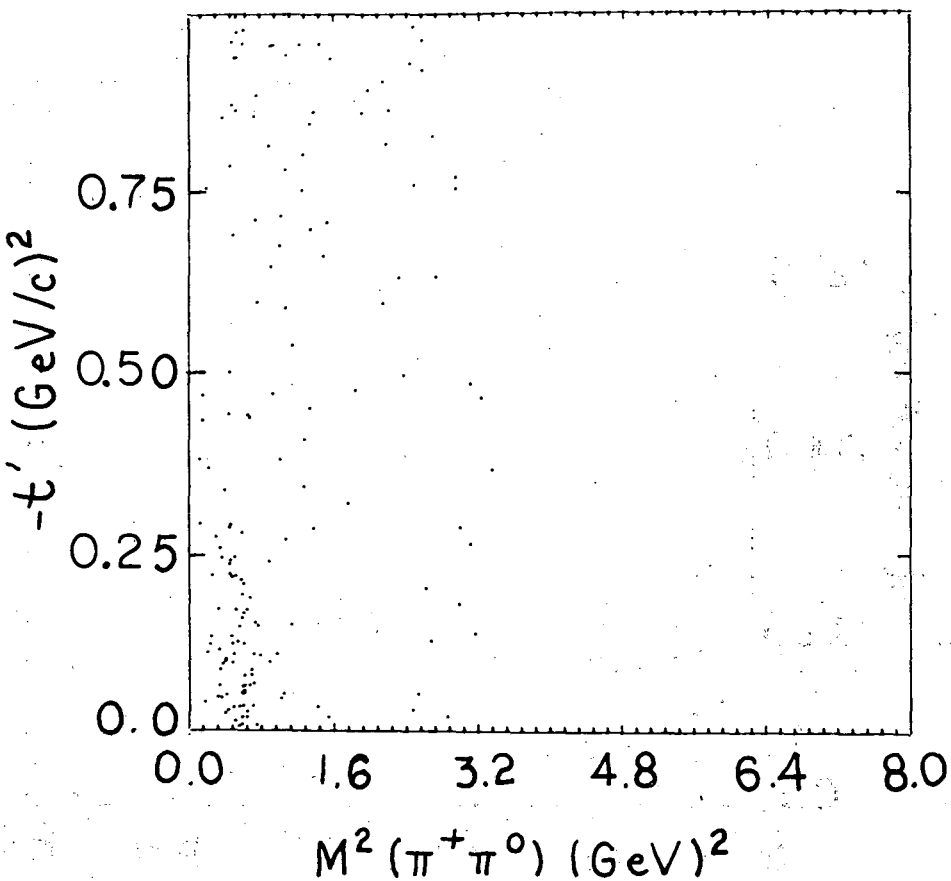

Fig. 31f. XBL711-2531

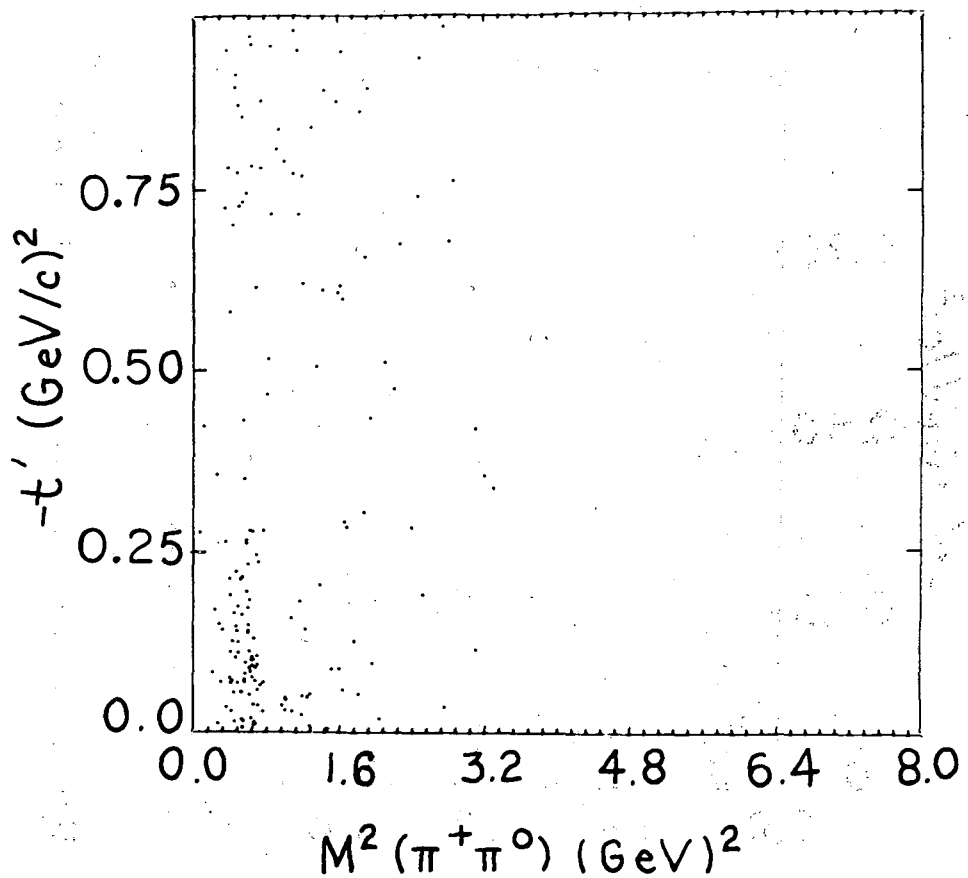

Fig. 31g. XBL711-2530

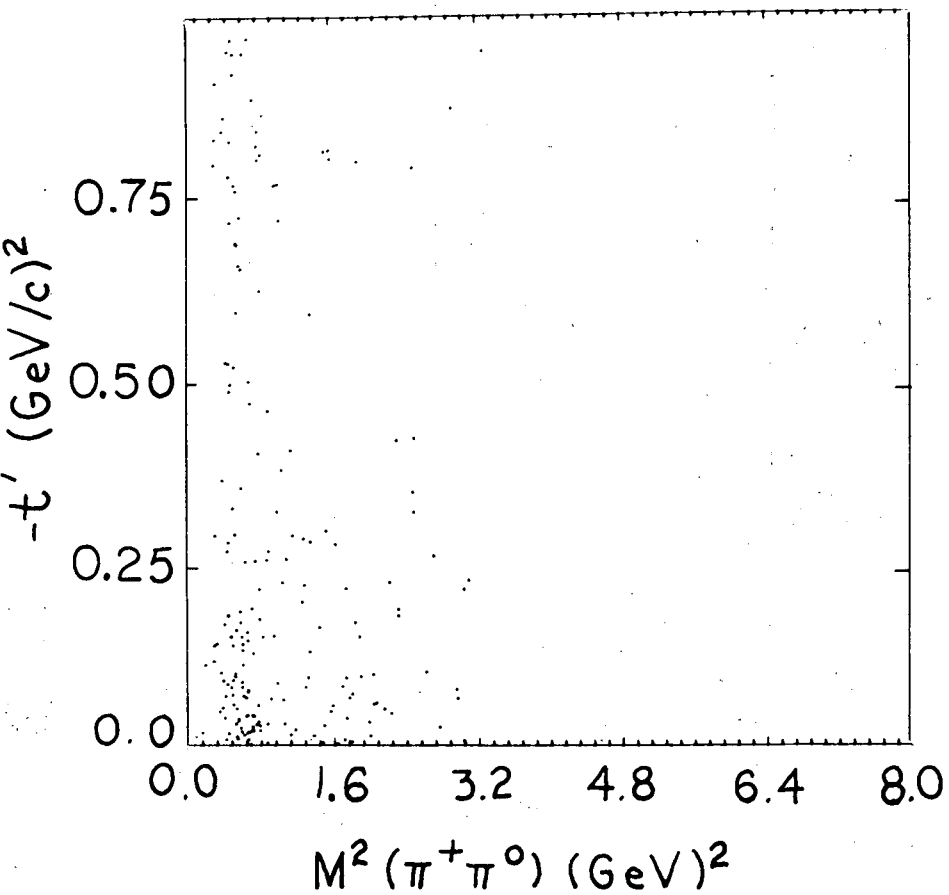

Fig. 31h.

XBL711-2529

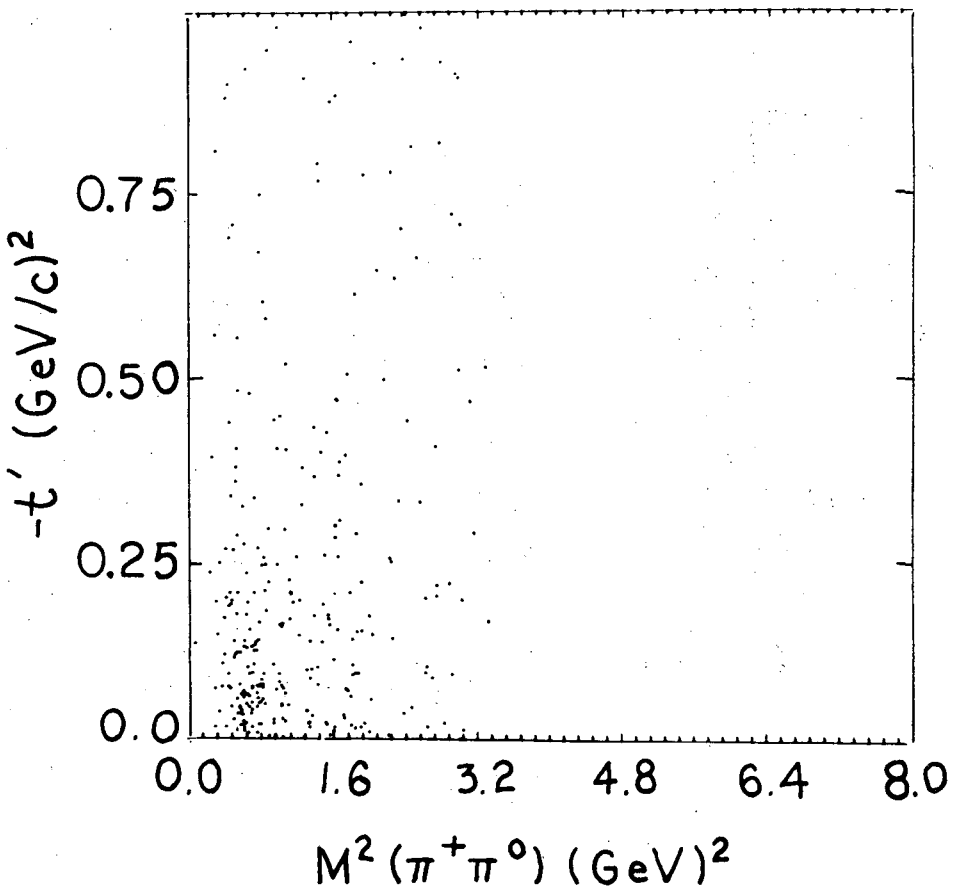

Fig. 31i.

XBL711-2528

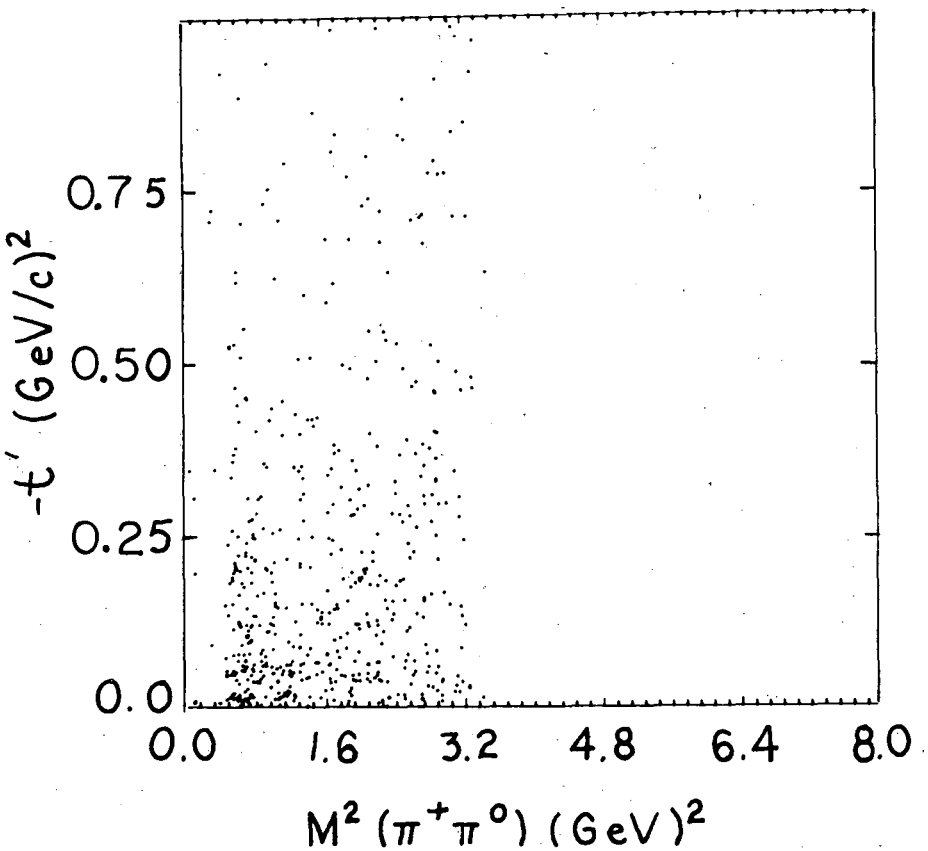

Fig. 31j. XBL 711-2527

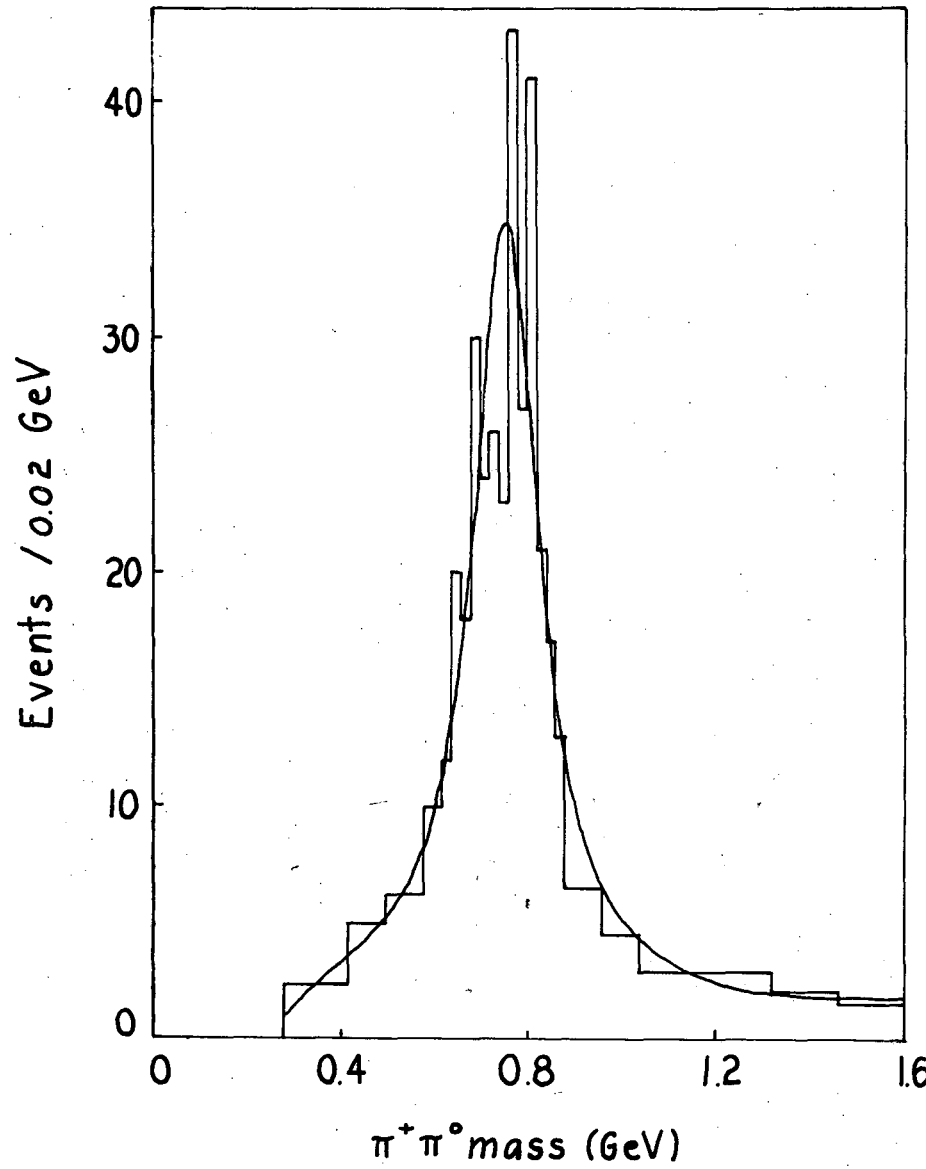

XBL 715-3387

Fig. 32. $\pi^+\pi^0$ mass spectrum with $t_p < 0.5$ (GeV/c)^2 and $|\cos\alpha| < 0.5$. The curve is the fit discussed in the text.

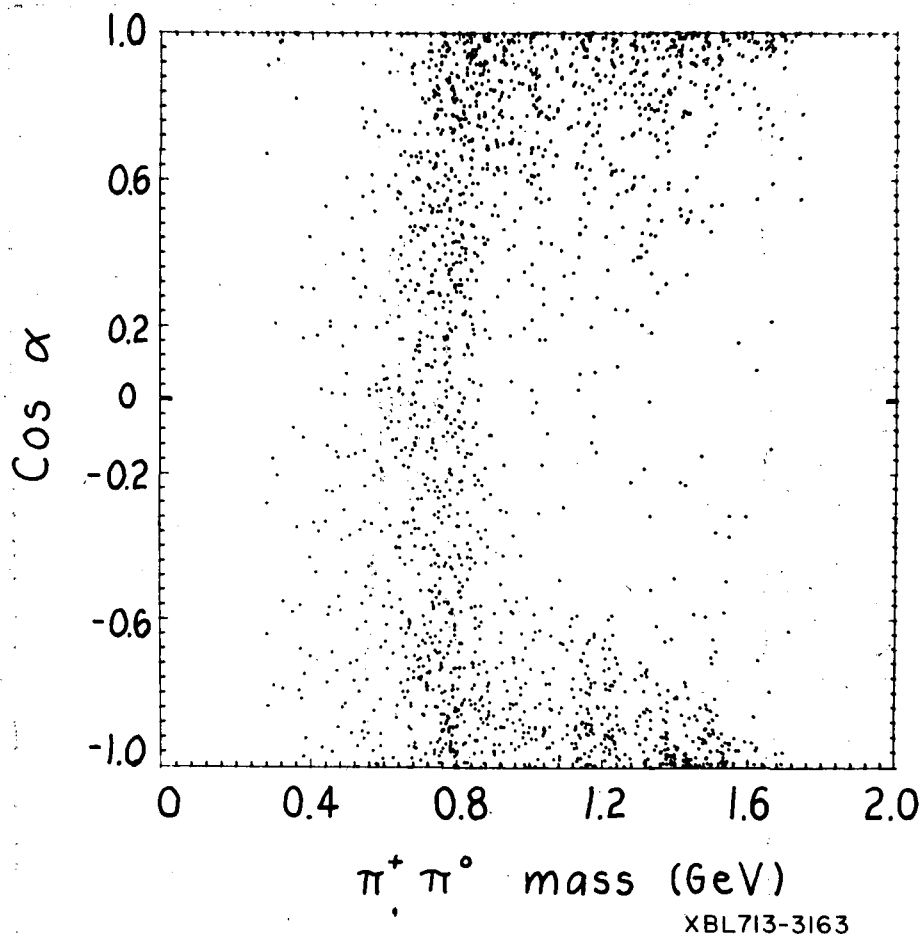

Fig. 33. Scatter plot of cos α vs. $\pi^+\pi^0$ mass for $t < 0.5$ $(\mathrm{GeV})^2$.

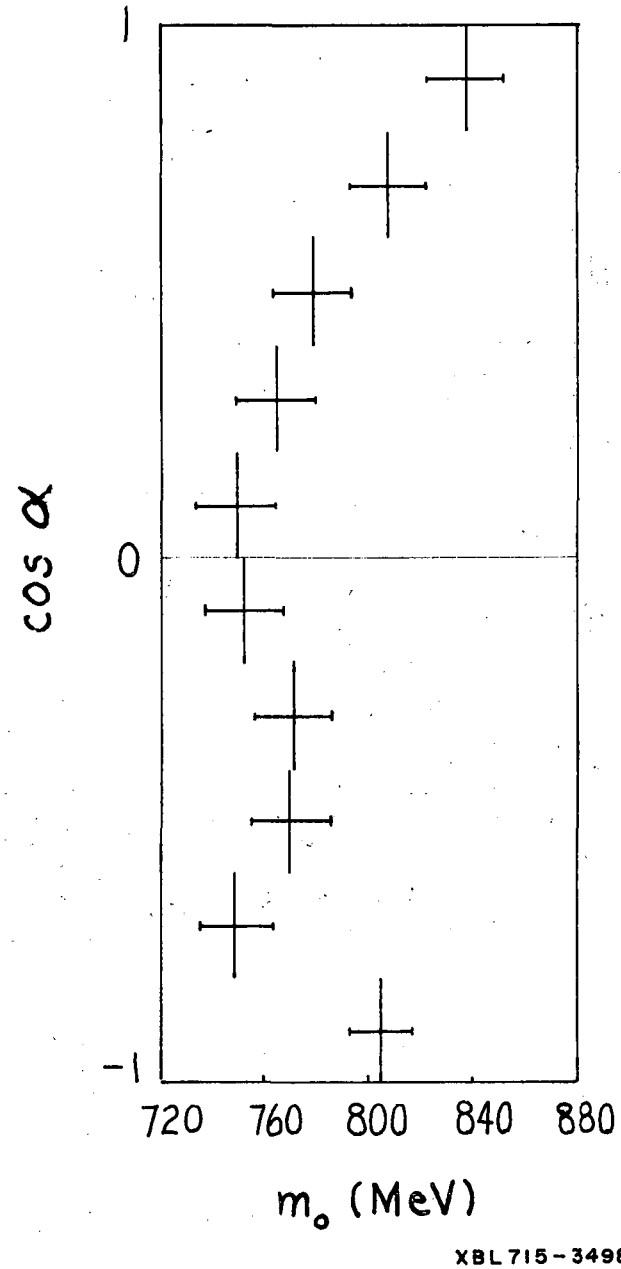

Fig. 34. A plot of the fitted central value of ρ^+ mass as a function of cos α.

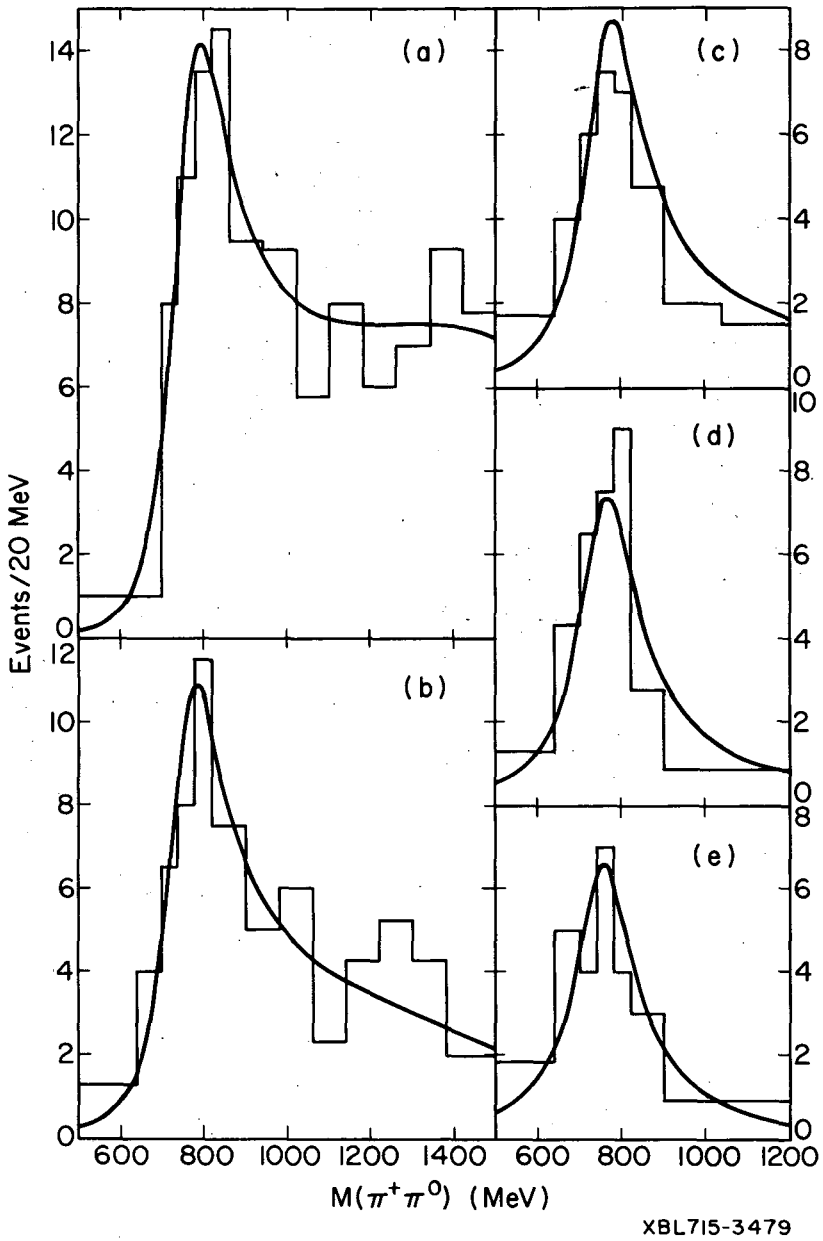

Fig. 35. $\pi^+\pi^0$ mass spectra used in fitting the ρ^+-diffraction interference model. a) cos α, 0.8 -1.0; b) cos α, 0.6 -0.8; c) cos α, 0.4 -0.6; d) cos α, 0.2-0.4; e) cos α, 0 -0.2. The curves are the fits of the ρ^+-diffraction interference model with $\delta = 10°$.

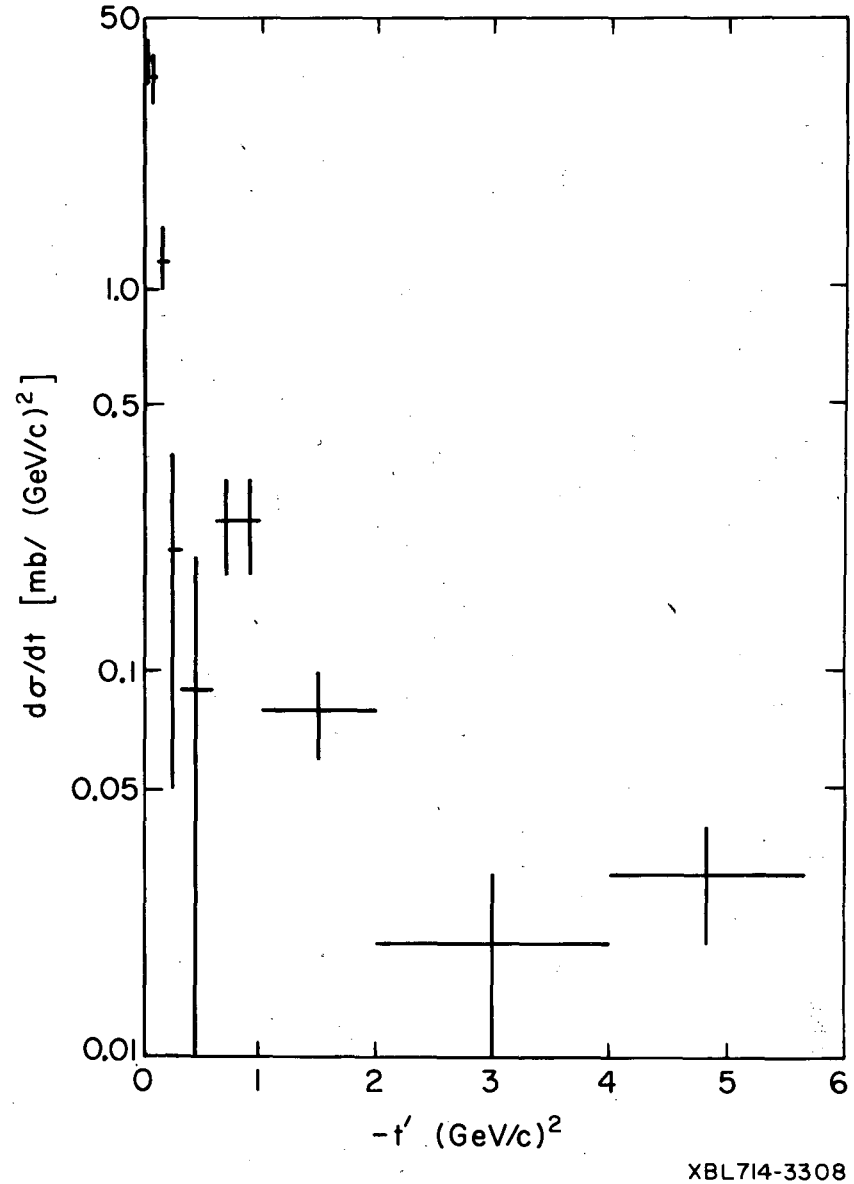

Fig. 36. Momentum transfer distribution in the reaction $\pi^+p \rightarrow \rho^+p$.

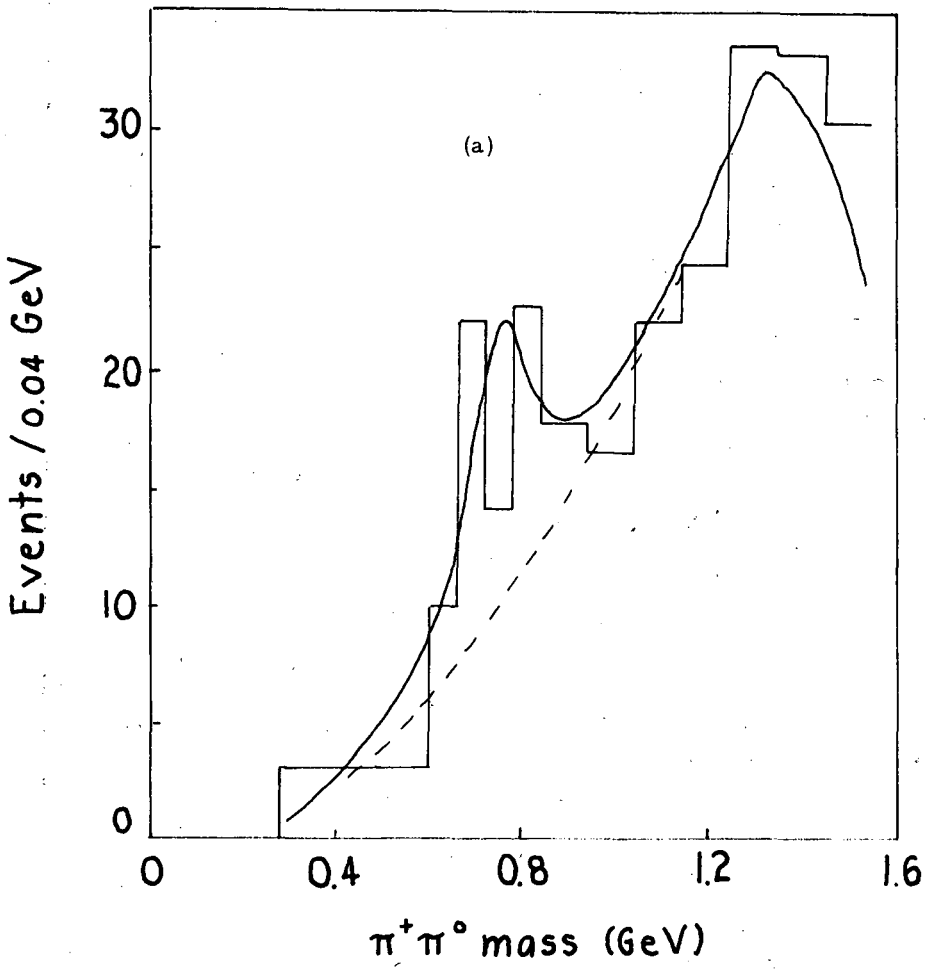

XBL715-3385

Fig. 37. $\pi^+\pi^0$ mass spectra for a) t'_p, 2-4 $(GeV/c)^2$ and b) $t'_p > 4$ $(GeV/c)^2$. The solid curves are the fits including ρ^+ production plus background. The dashed curves are the background contributions to the fits.

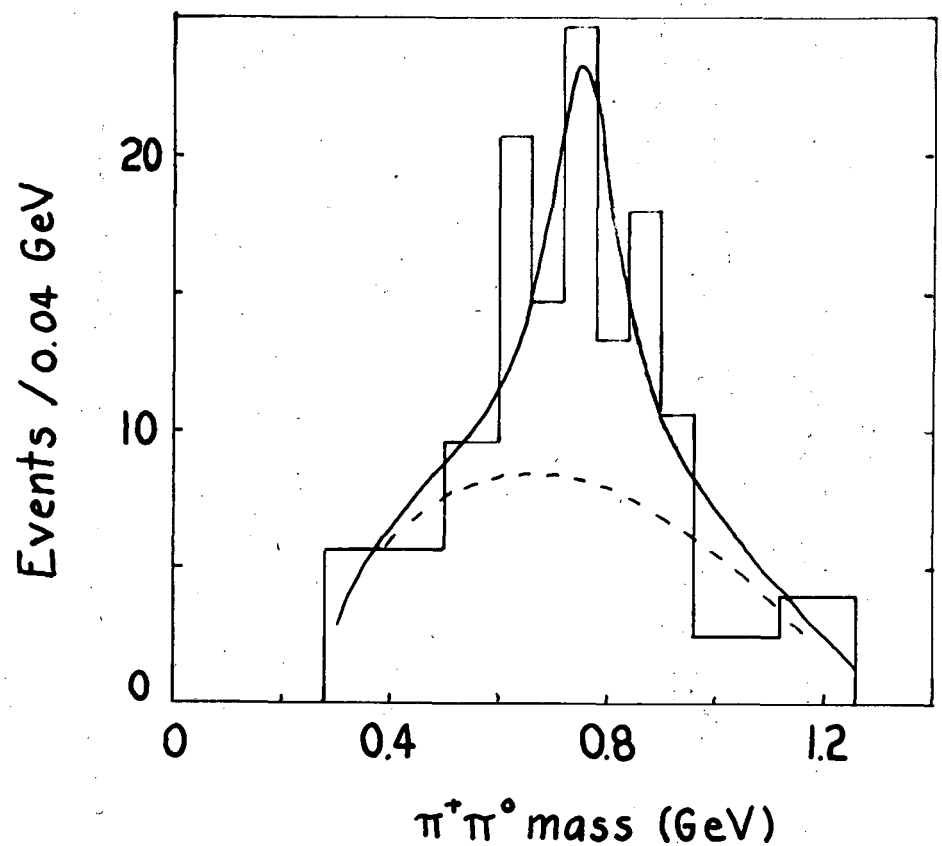

Fig. 37b. XBL715-3386

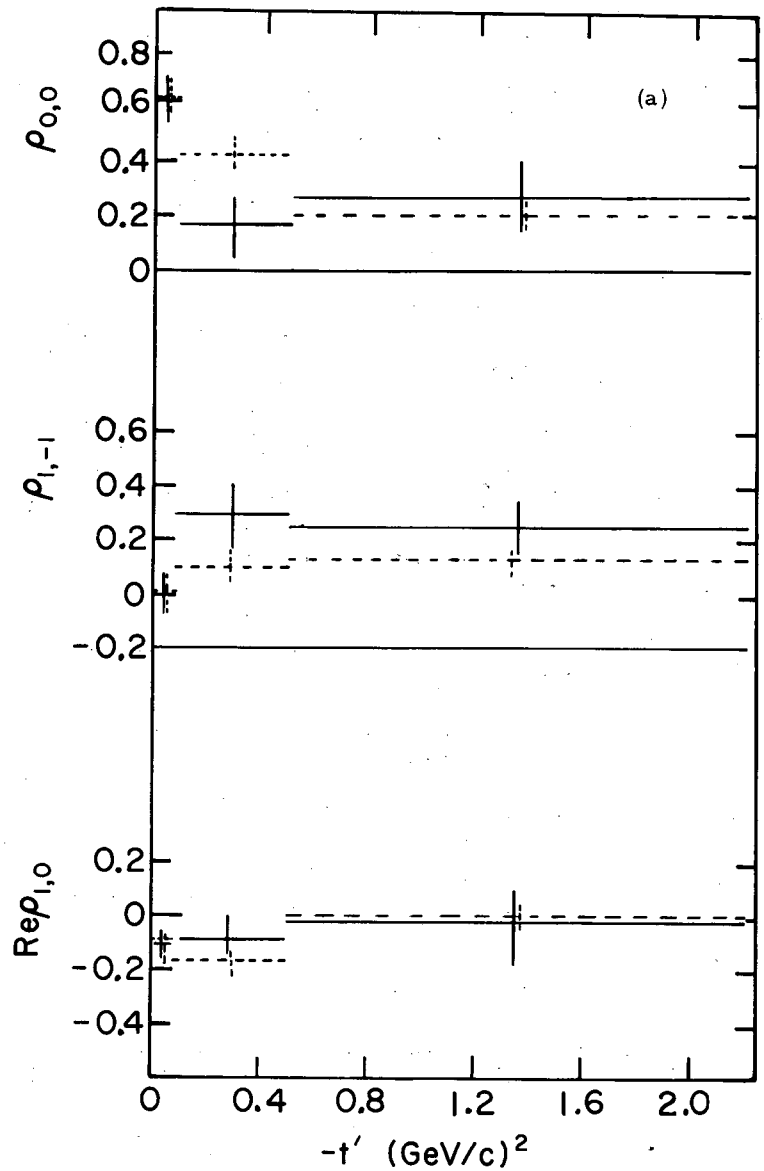

XBL714-3310

Fig. 38. Density matrix elements for the ρ^+ from the reaction $\pi^+p \rightarrow \rho^+p$ in the Jackson frame. The only difference between a) and b) is the t' bins selected. The dashed crosses in Fig. 38a are calculated by taking a $\pi^+\pi^0$ mass selection of 0.66 -0.86 GeV only.

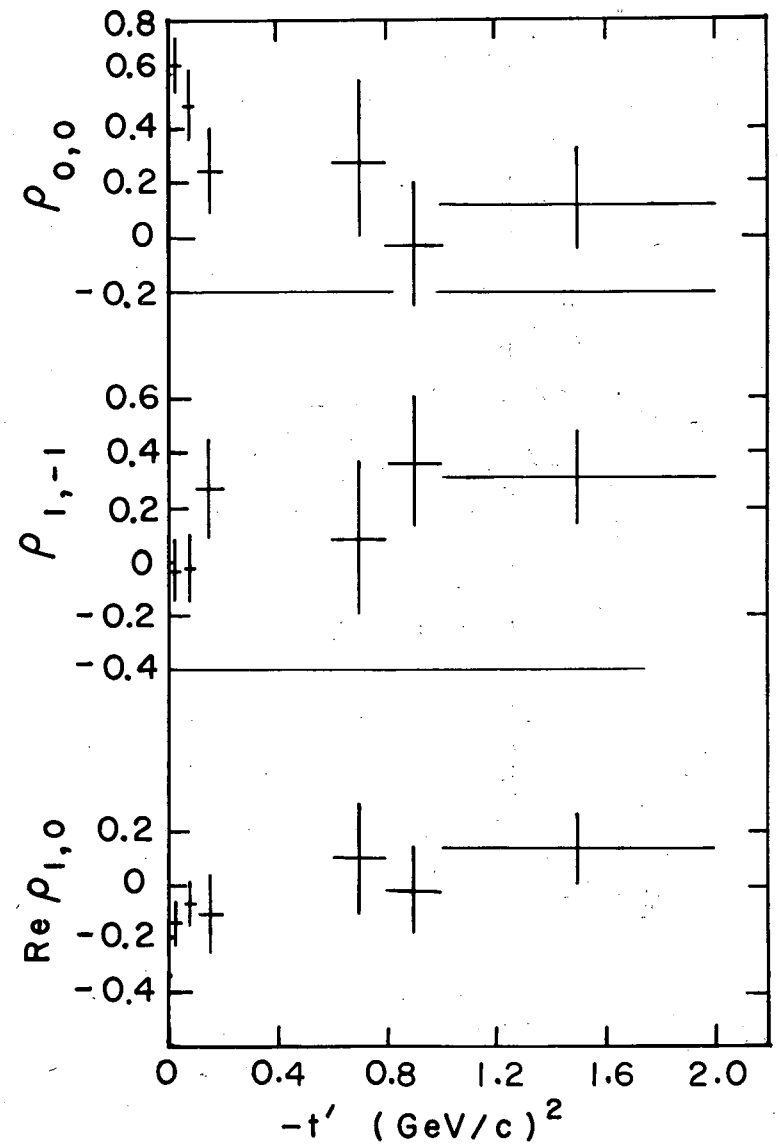

Fig. 38b. XBL714-3303

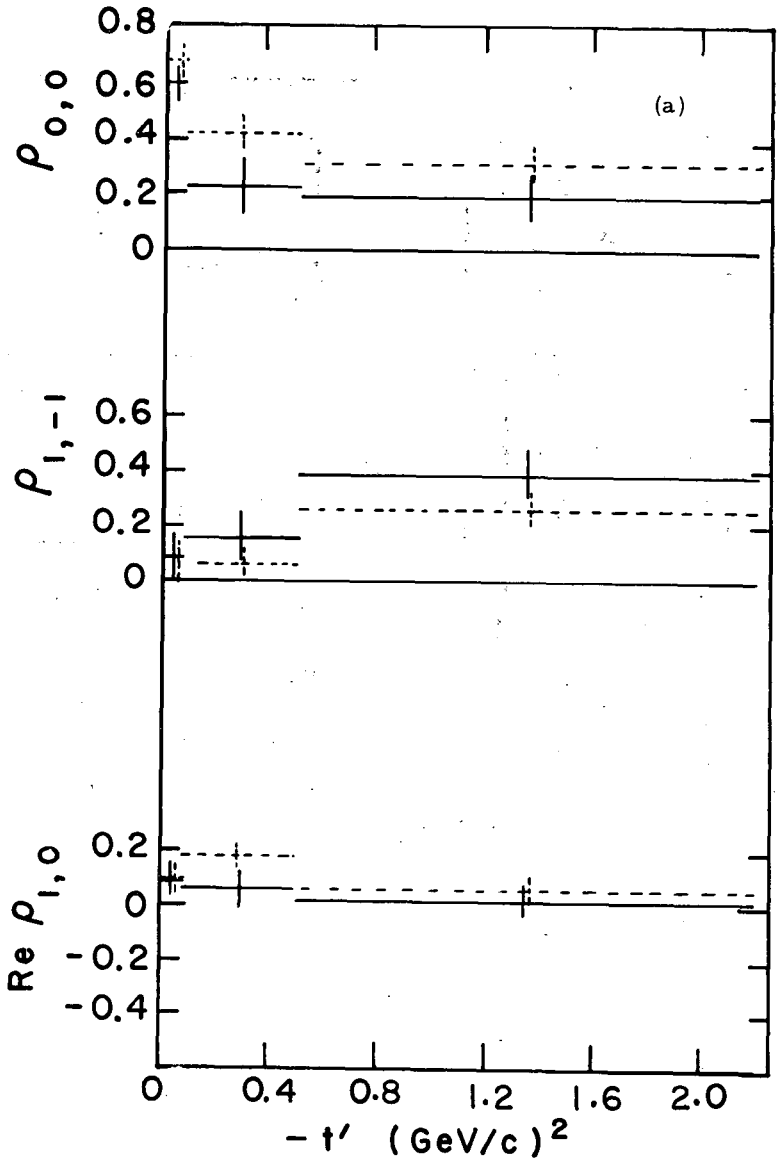

XBL714-3305

Fig. 39. Density matrix elements for the ρ^+ from the reaction $\pi^+p \rightarrow \rho^+p$ in the helicity frame. The only difference between a) and b) is the t' bins selected. The dashed crosses in Fig. 39a are calculated by taking a $\pi^+\pi^0$ mass selection of 0.66 -0.86 GeV only.

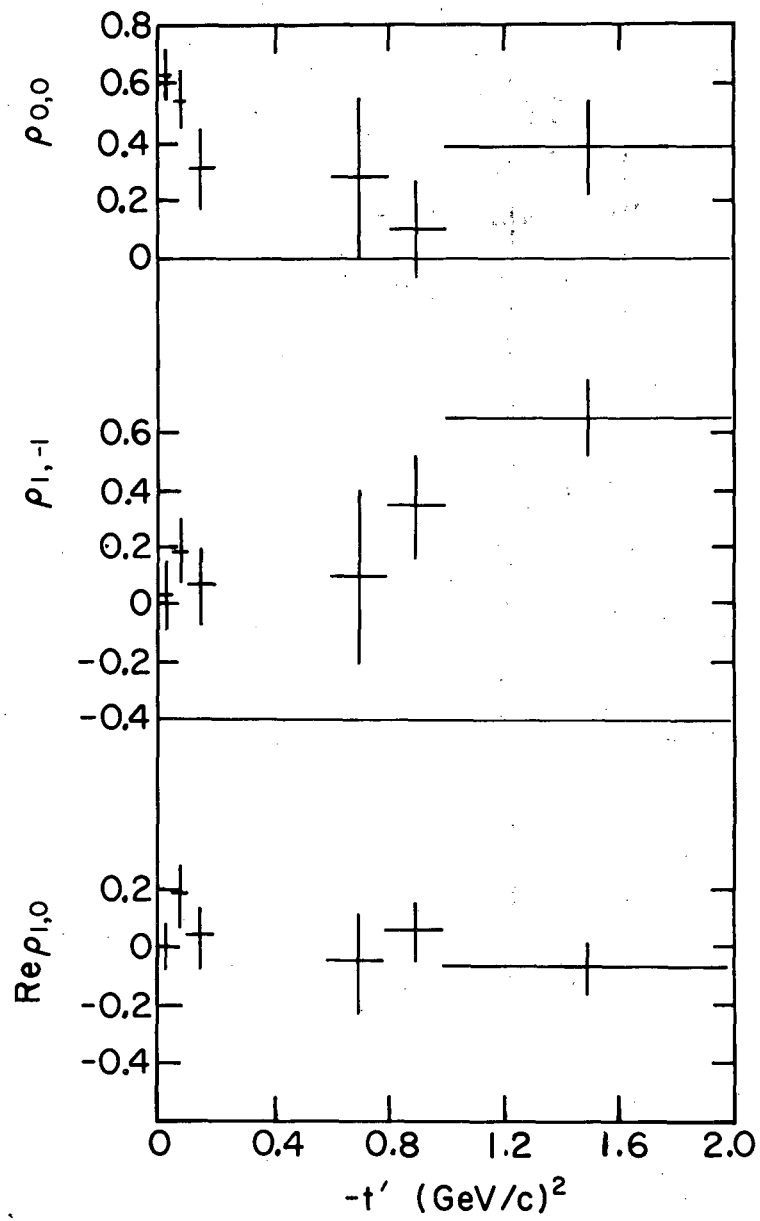

Fig. 39b. XBL714-3307

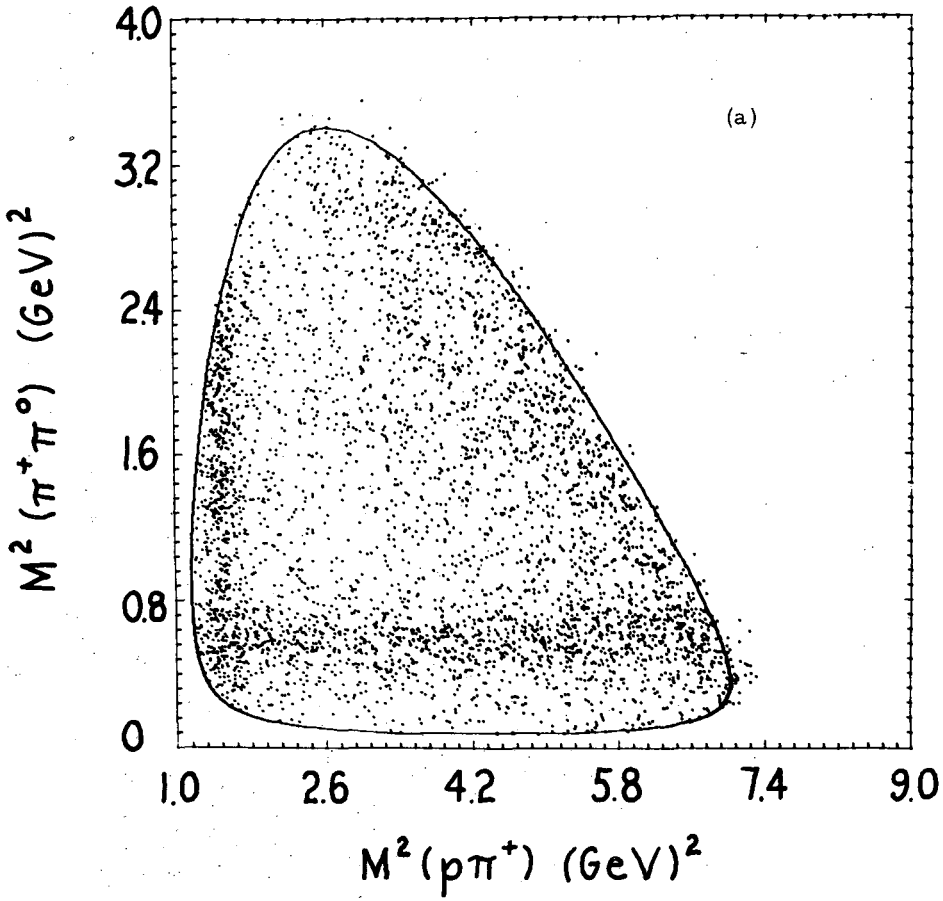

XBL715-3382

Fig. 40. Dalitz plots for the final state $p\pi^+\pi^0$. a) all t'; b) t', 0 -0.08 (GeV/c)^2; c) t', 0.08 -0.5 (GeV/c)^2.

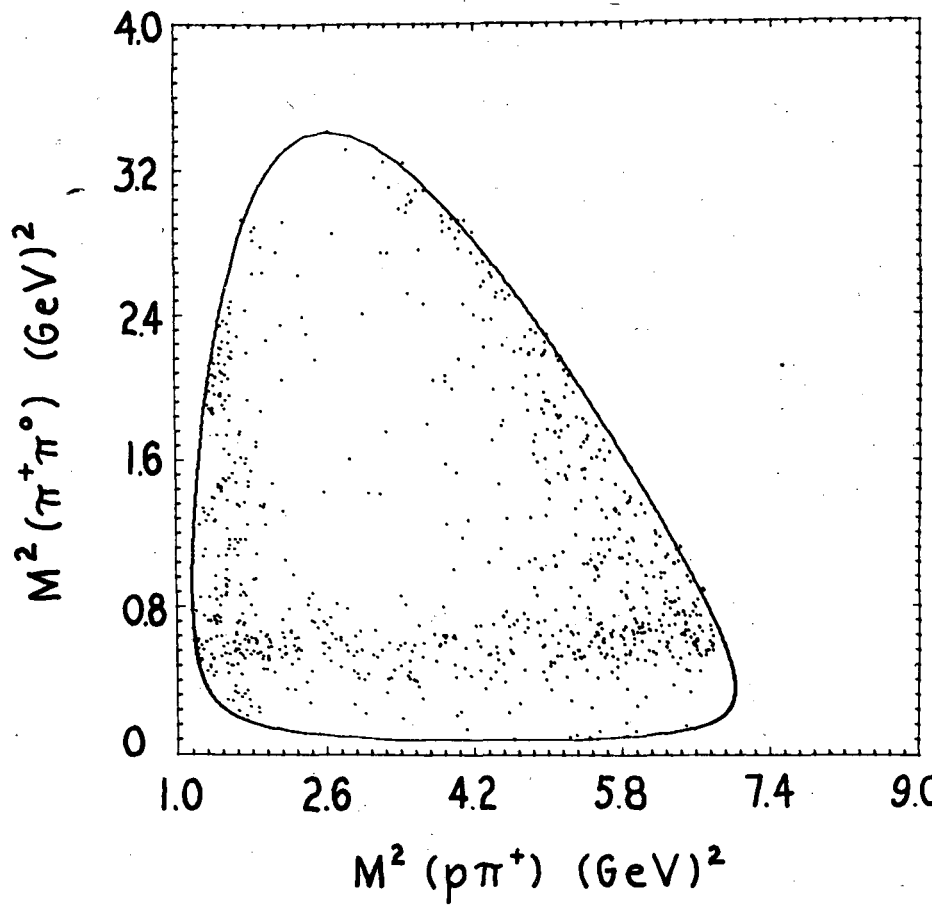

Fig. 40b.

XBL715-3383

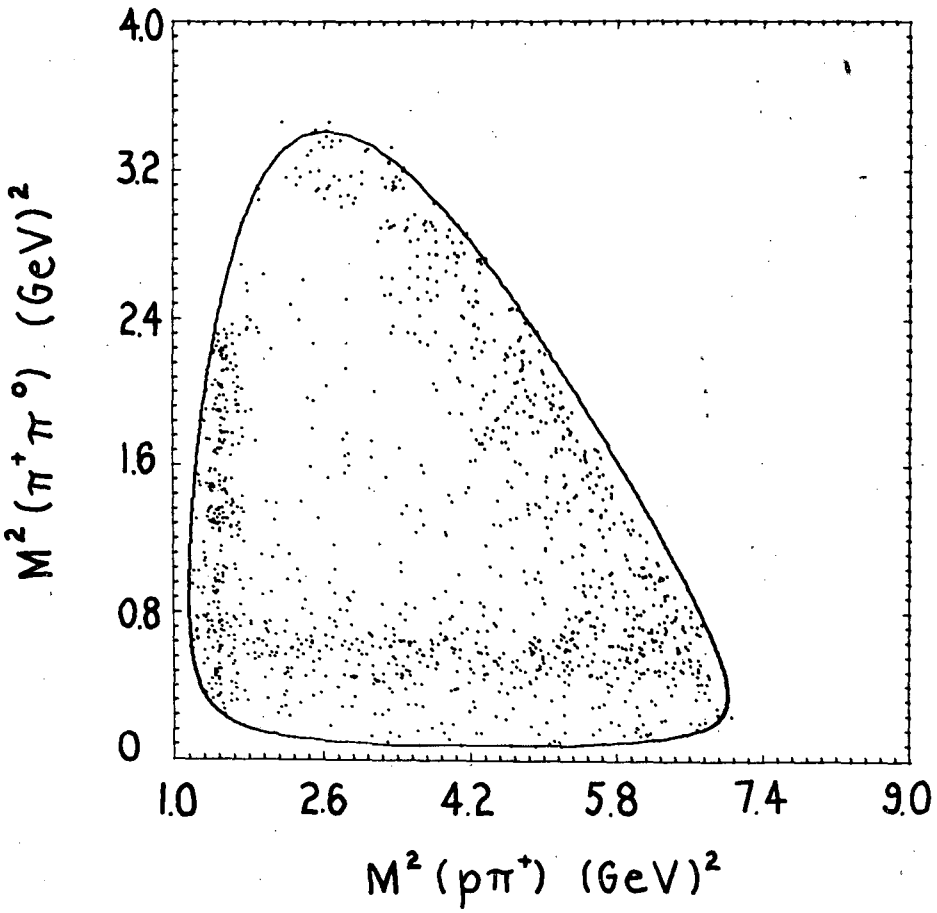

Fig. 40c.

XBL715-3384

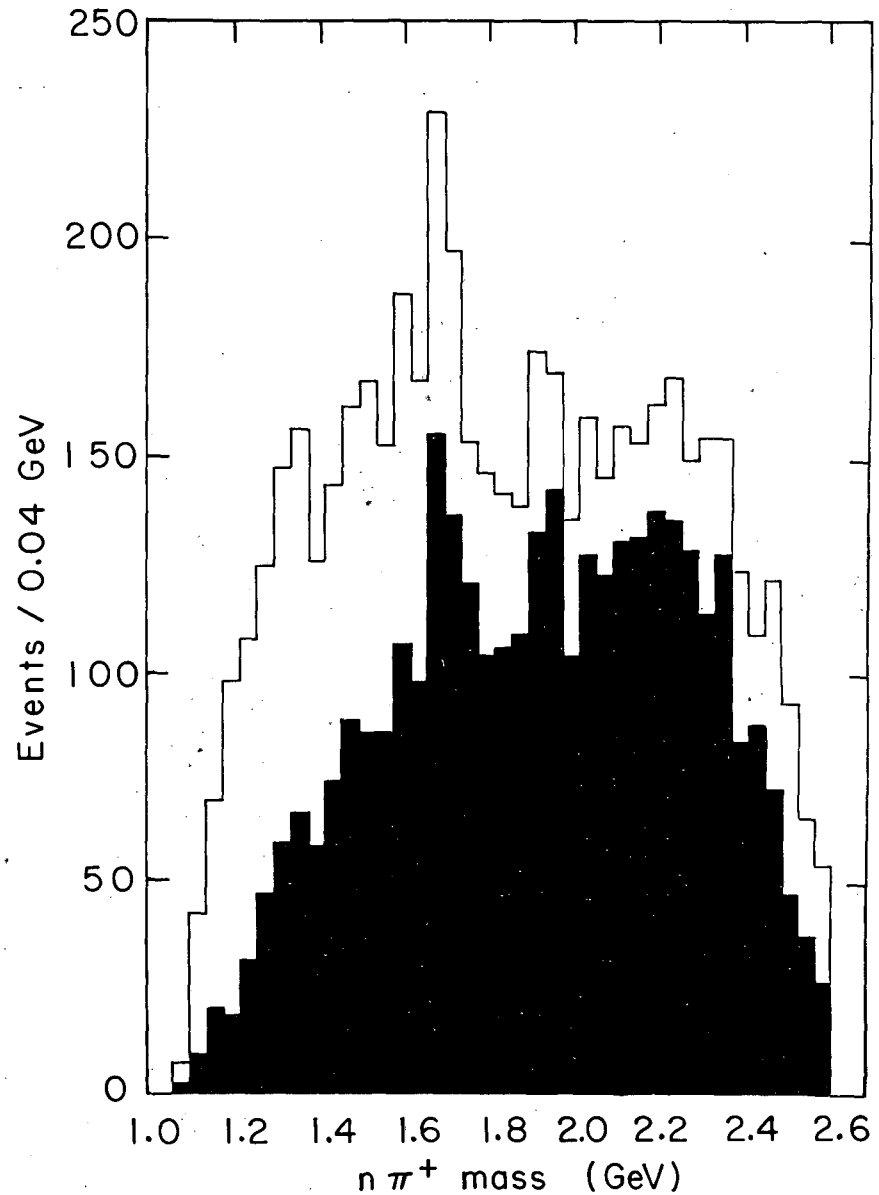

XBL714-3304

Fig. 41. $n\pi^+$ mass spectrum. Shaded events are for t_{π^+} greater than 0.5 $(GeV)^2$.

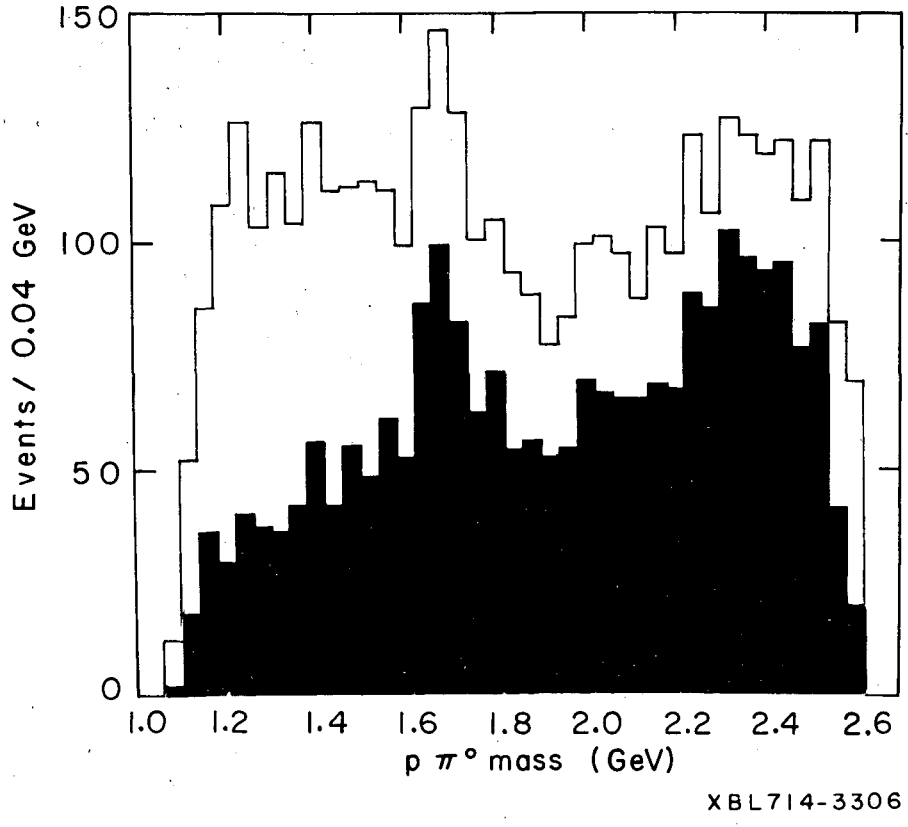

Fig. 42 $p\pi^0$ mass spectrum. Shaded events are t_{π^+} greater than 0.5 $(GeV/c)^2$.

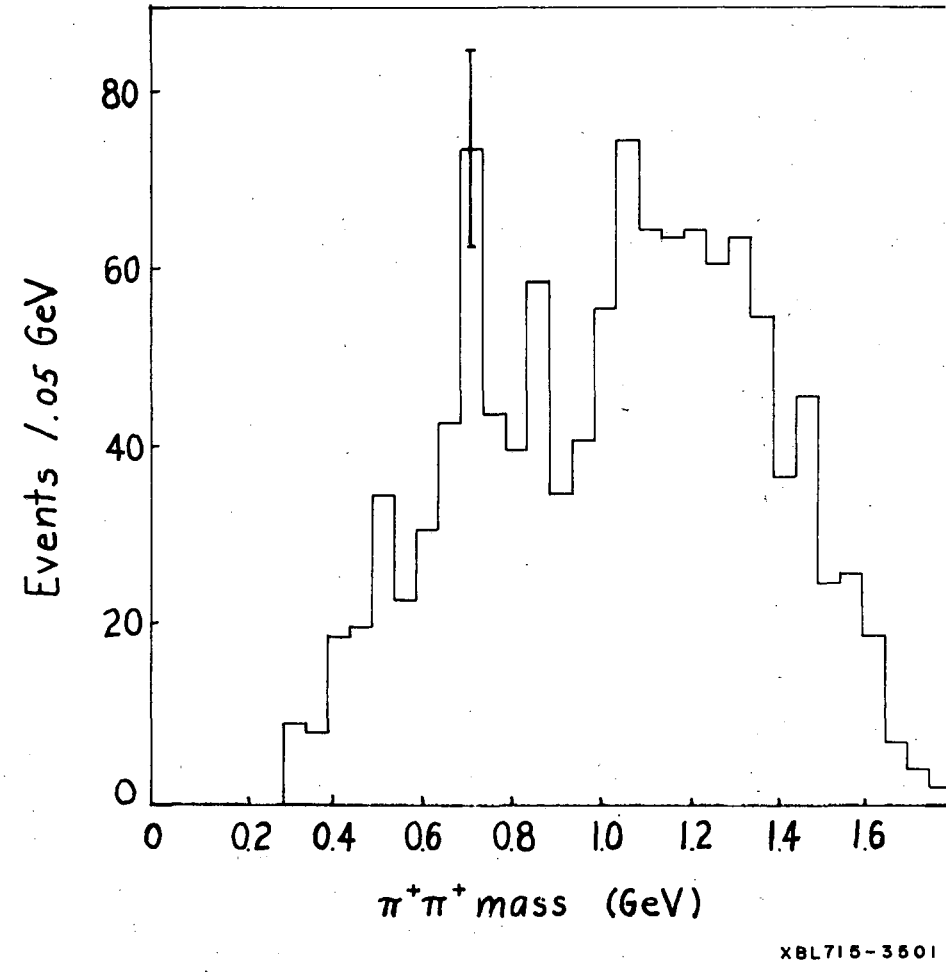

Fig. 43. $\pi^+\pi^+$ mass spectrum for t_n less than 0.5 $(GeV/c)^2$.

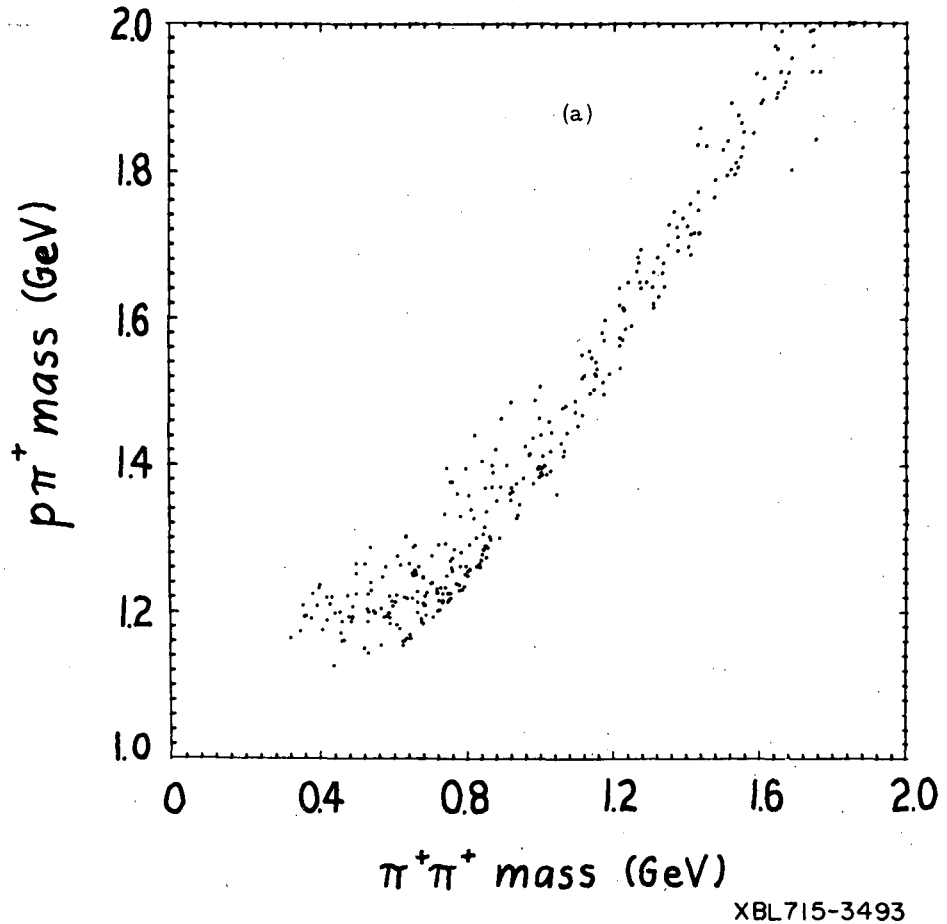

Fig. 44. Scatter plots of "p"π^+ mass vs. $\pi^+\pi^+$ mass for events selected as $n\pi^+\pi^+$ as discussed in the text. a) Highly contaminated rolls. b) Rolls with relatively small proton contamination.

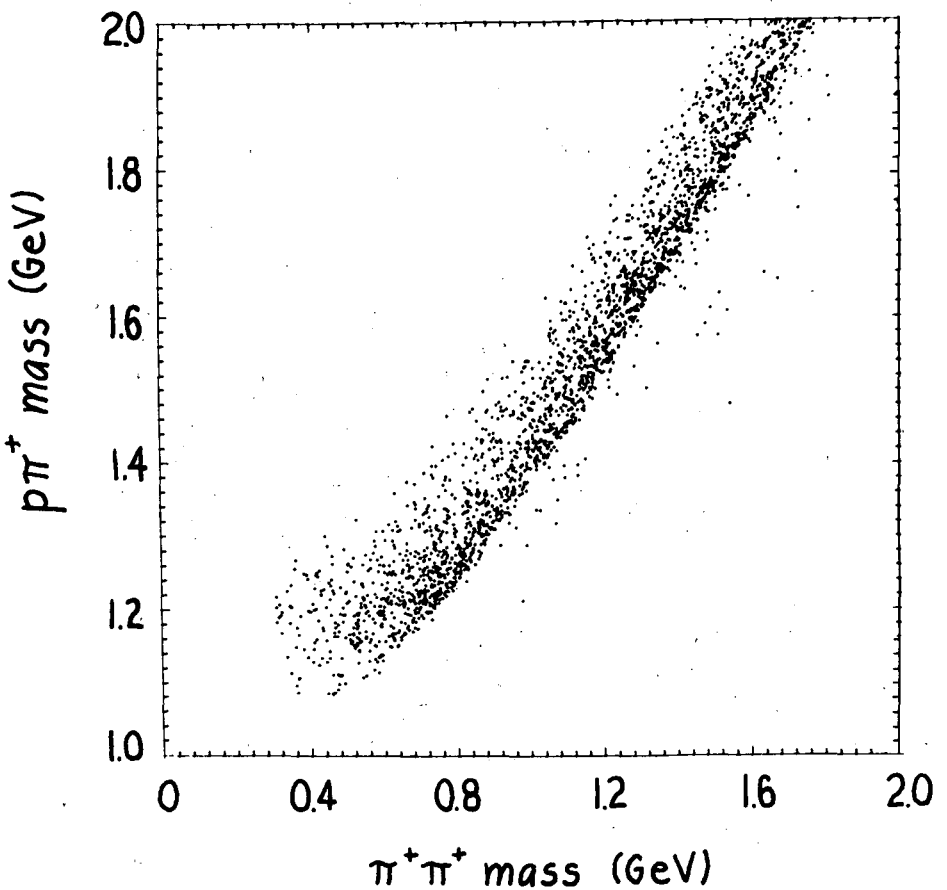

Fig. 44b.

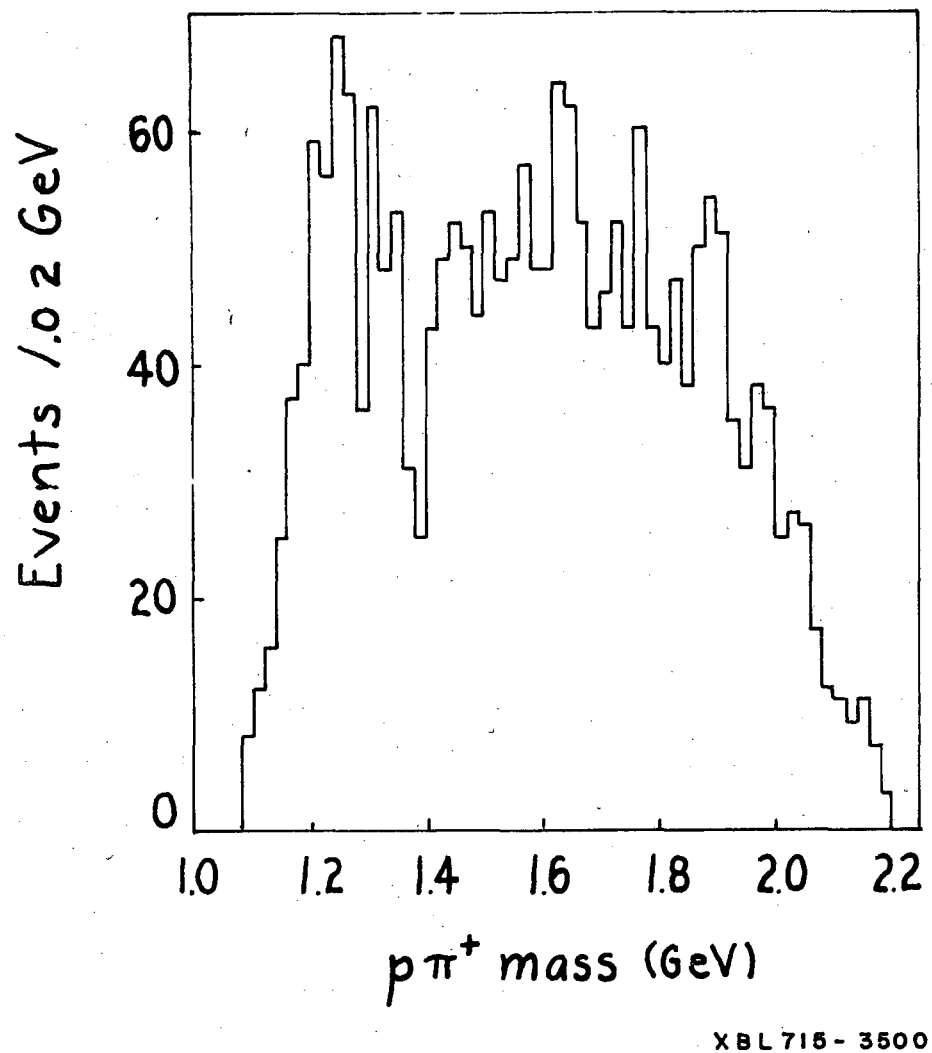

Fig. 45. "p" π^+ mass spectrum for events with unique possibility of misidentification as discussed in the text.

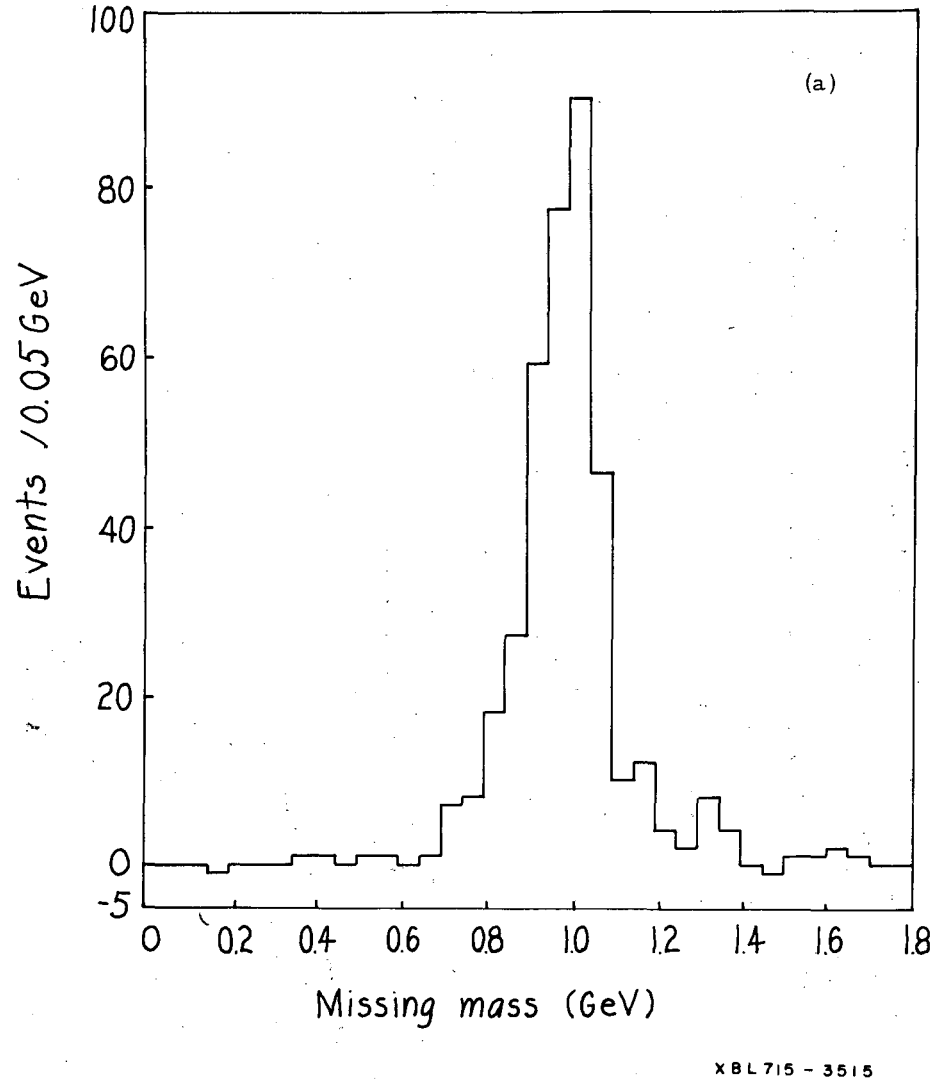

Fig. 46. Missing-mass spectra, based on the following hypotheses:
a) $\pi^+p \rightarrow \pi^+\pi^+MM$
b) $\pi^+p \rightarrow \pi^+pMM$,
c) $pp \rightarrow \pi^+pMM$.
for events selected as $n\pi^+\pi^+$ as discussed in the text.

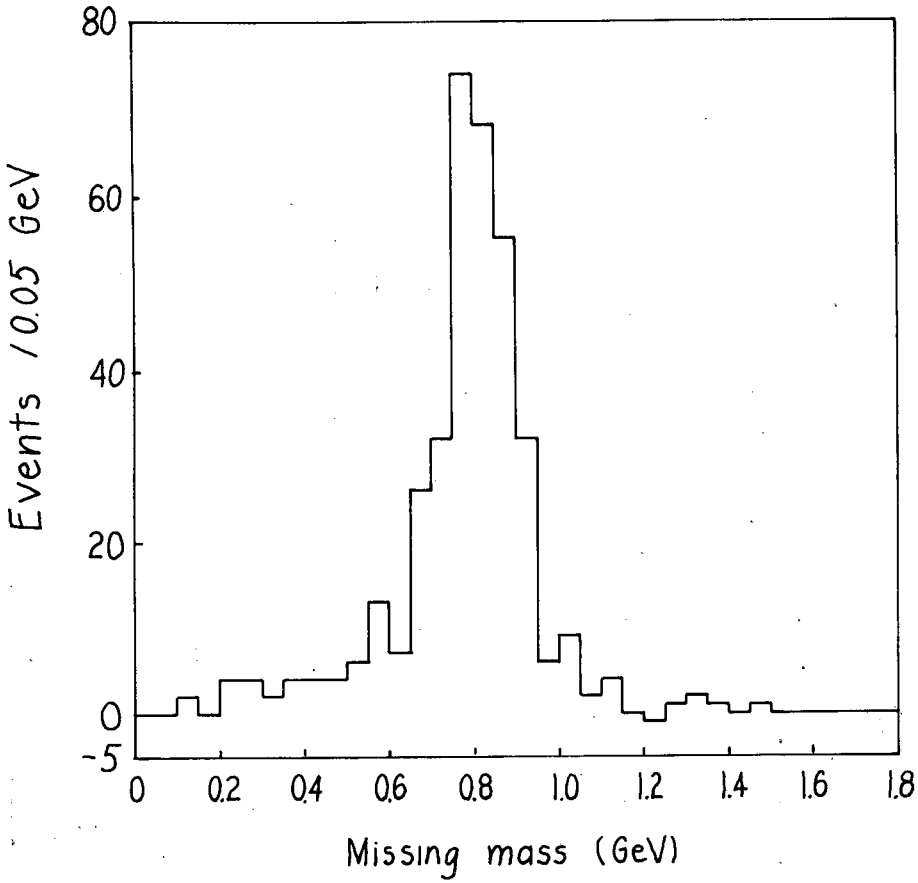

Fig. 46b.

XBL715-3516

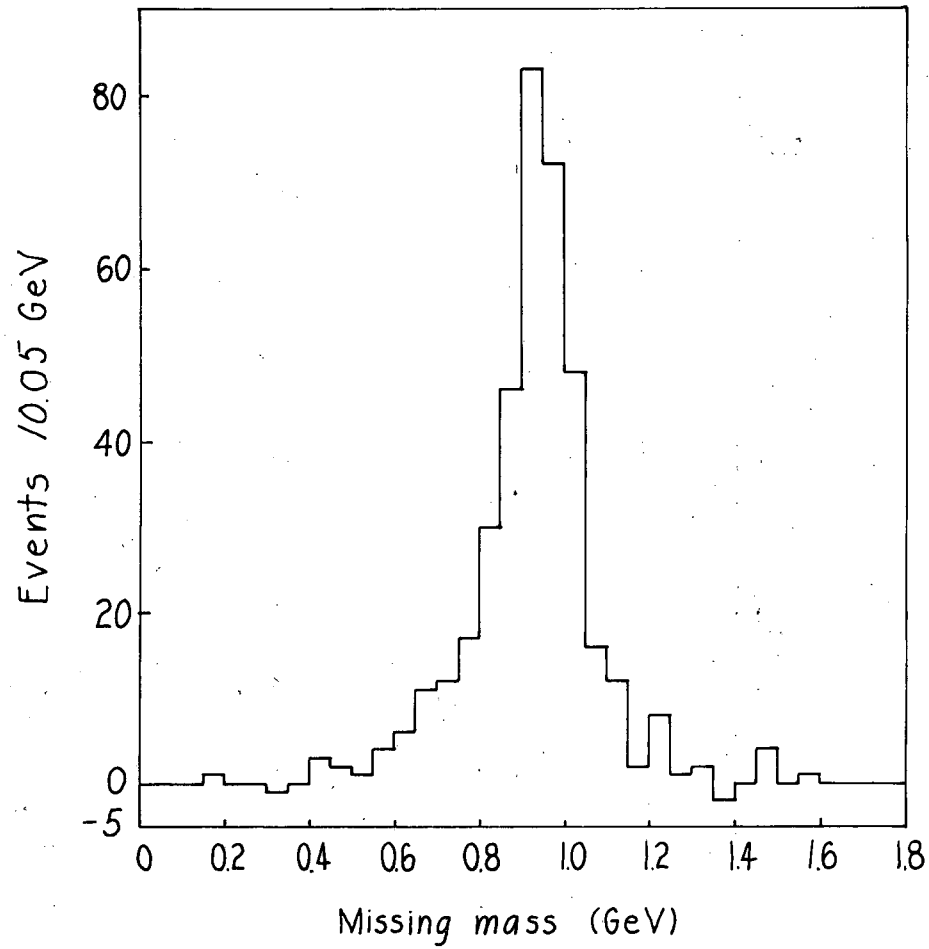

Fig. 46c.

XBL715-3517

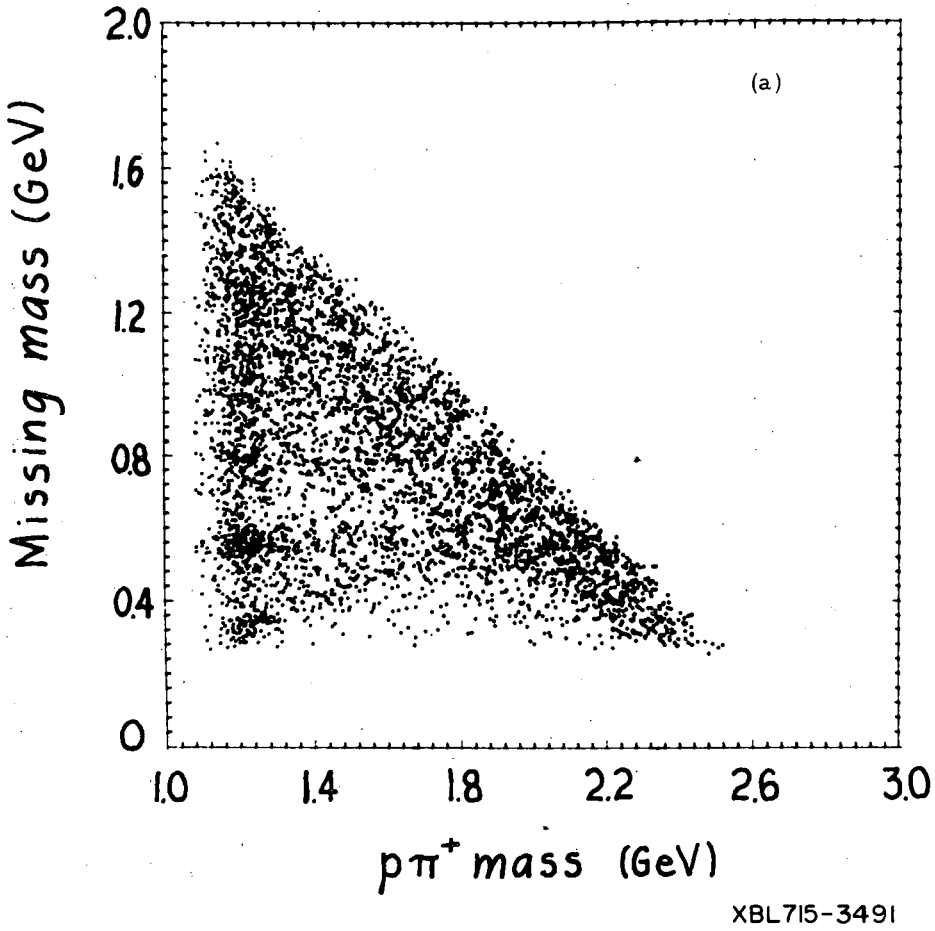

Fig. 47. Scatter plot of $p\pi^+$ mass vs. missing mass for events selected as $p\pi^+MM$ for a) $t_p < 1.5\ (GeV/c)^2$ and b) $t_p > 1.5\ (GeV/c)^2$.

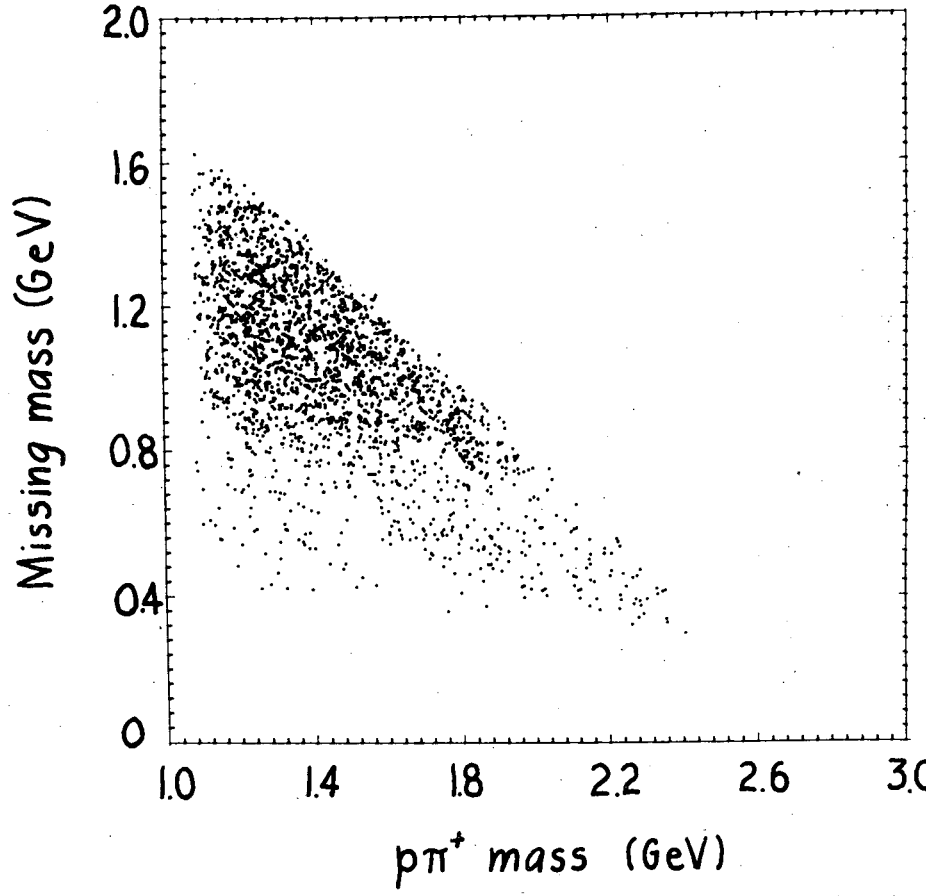

Fig. 47b. XBL715-3492

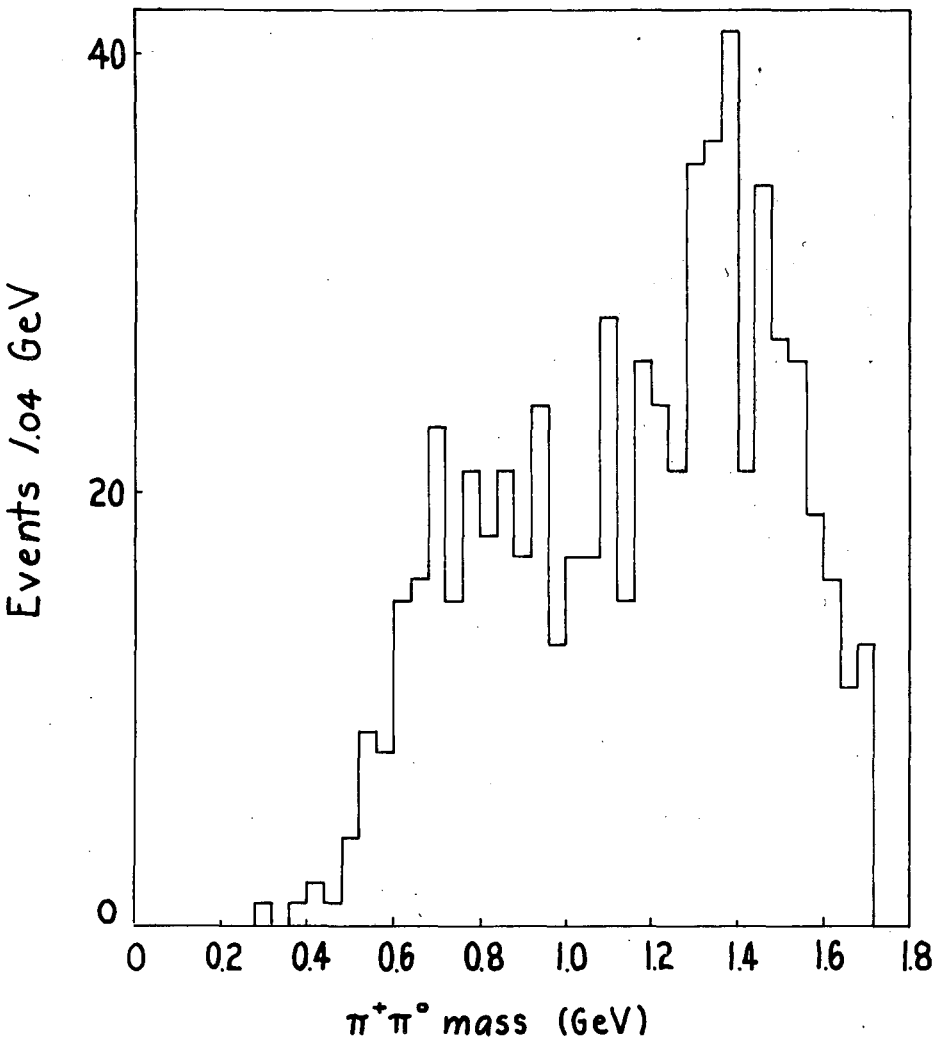

XBL715-3499

Fig. 48. $\pi^+\pi^0$ mass spectrum for t_p from 2.2 to 4.4 $(GeV/c)^2$.

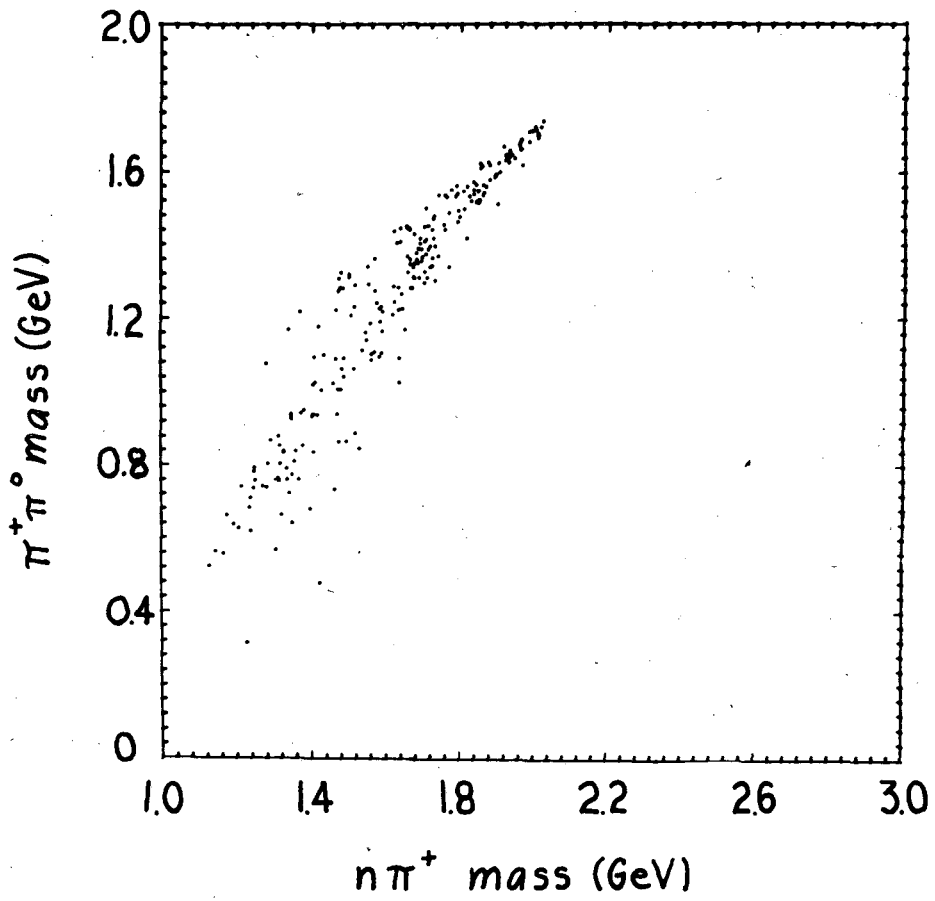

XBL715-3526

Fig. 49. Scatter plot of $\pi^+\pi^0$ mass vs. $n\pi^+$ mass for events ambiguous between $p\pi^+\pi^0$. and $n\pi^+\pi^+$ with t_p from 2.2 to 4.4 $(GeV/c)^2$.

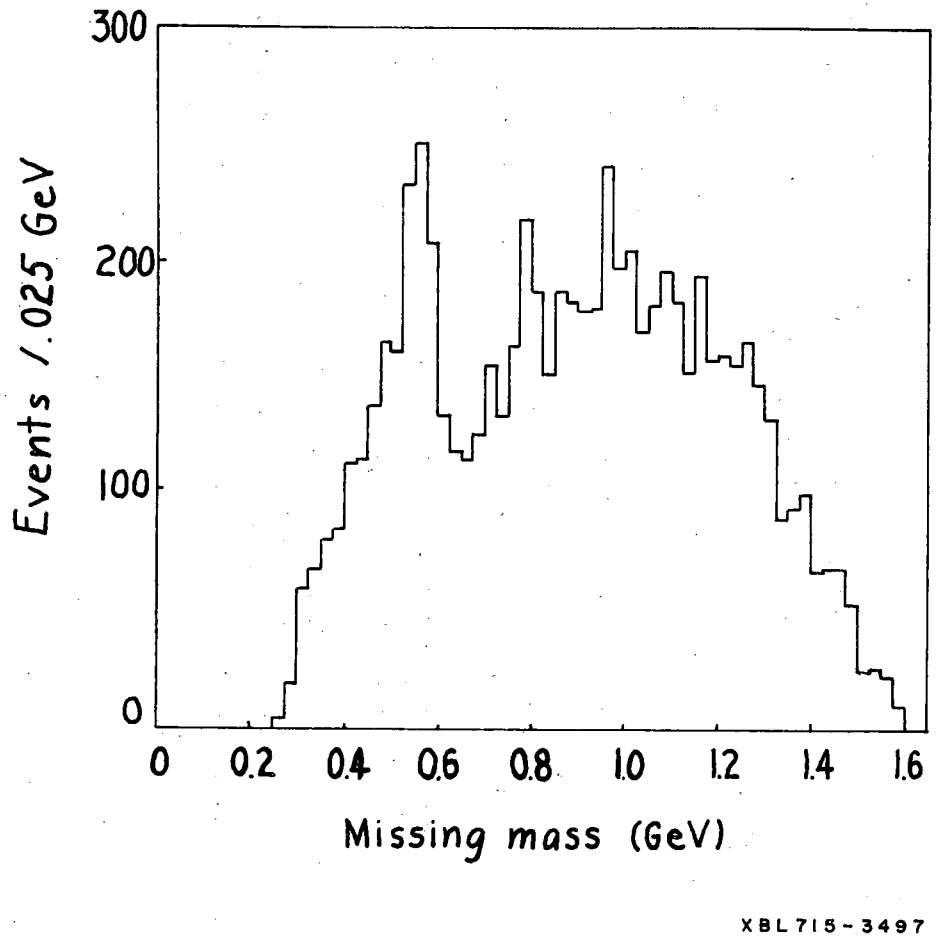

Fig. 50. Missing-mass spectrum for the final state $p\pi^+MM$.

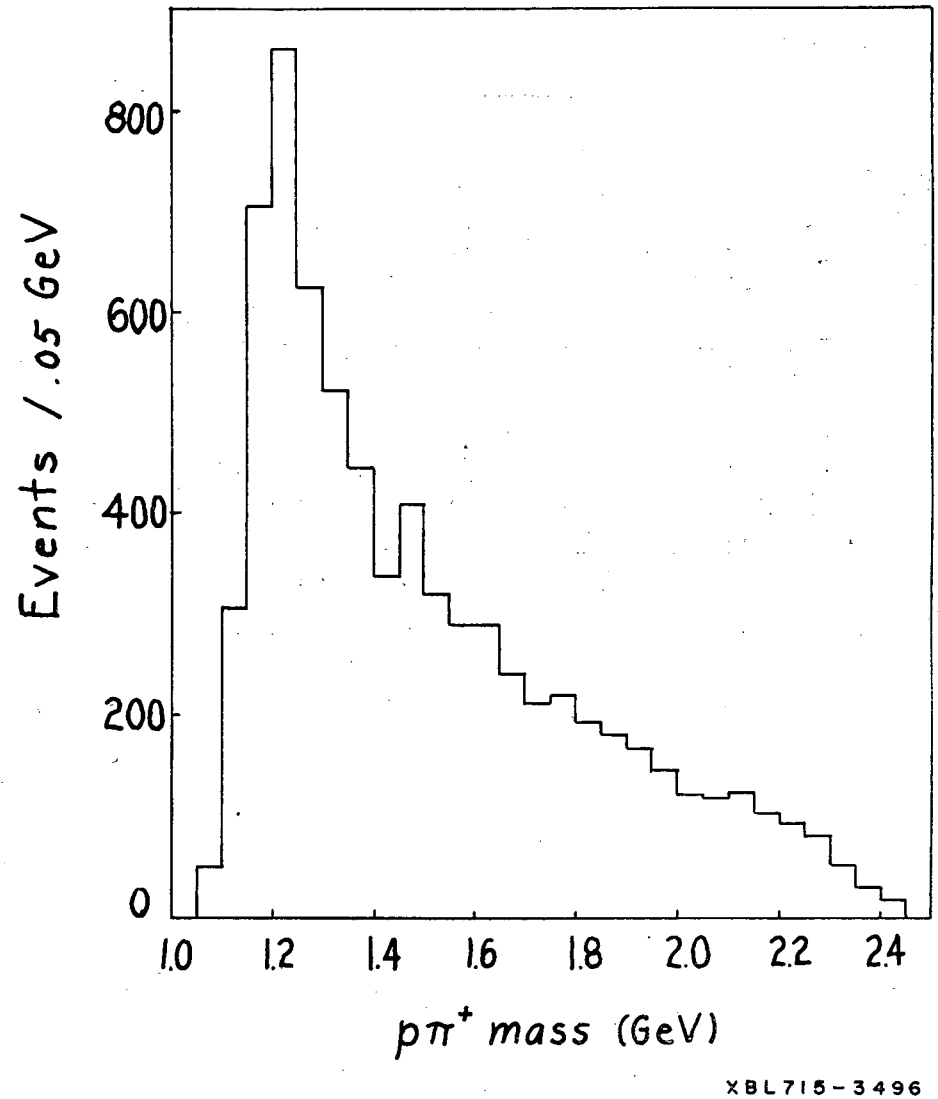

Fig. 51. $p\pi^+$ mass spectrum for the final state $p\pi^+MM$.

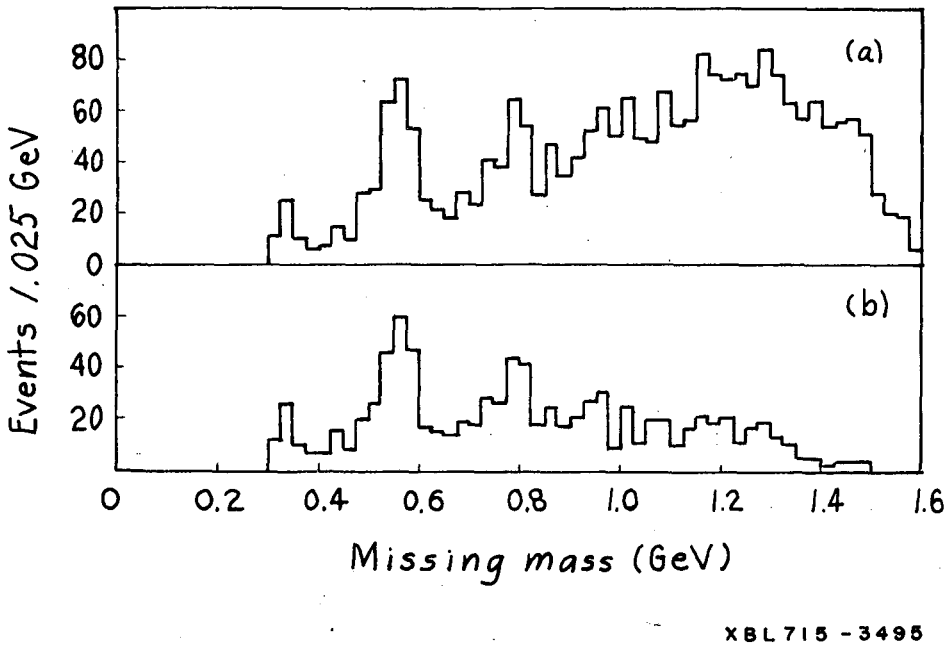

Fig. 52. Missing-mass spectrum for the final state $p\pi^+MM$ with $p\pi^+$ mass of 1.14 -1.3 GeV and a) all t_{MM}, b) $t_{MM} < 0.6\ (GeV/c)^2$.

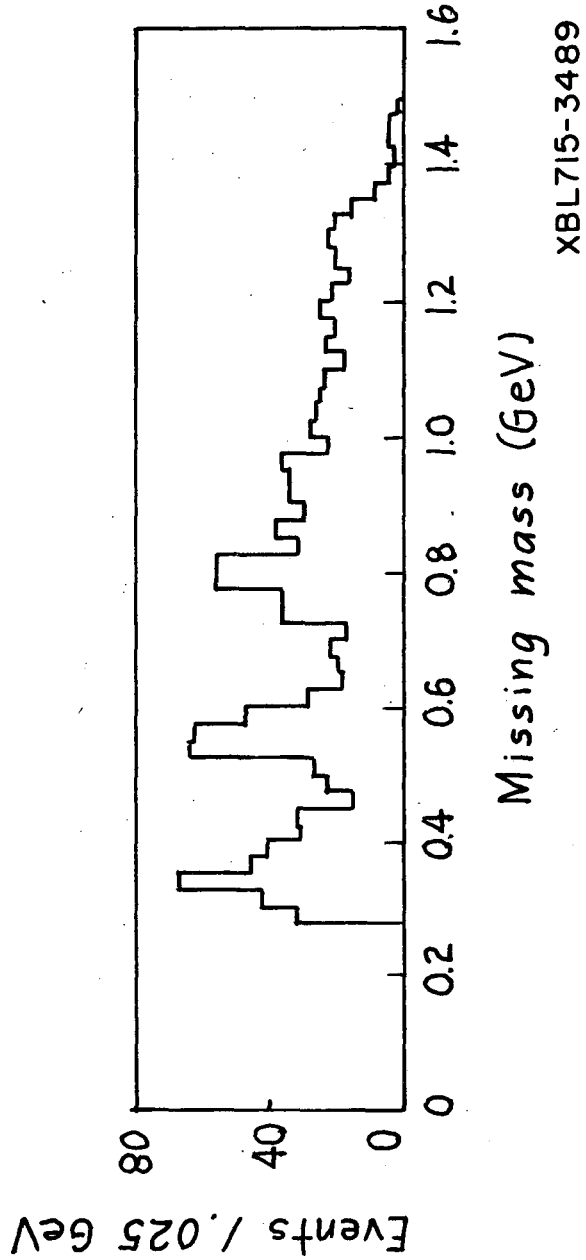

Fig. 53. Same as Fig. 52b, but without proton contamination subtraction.

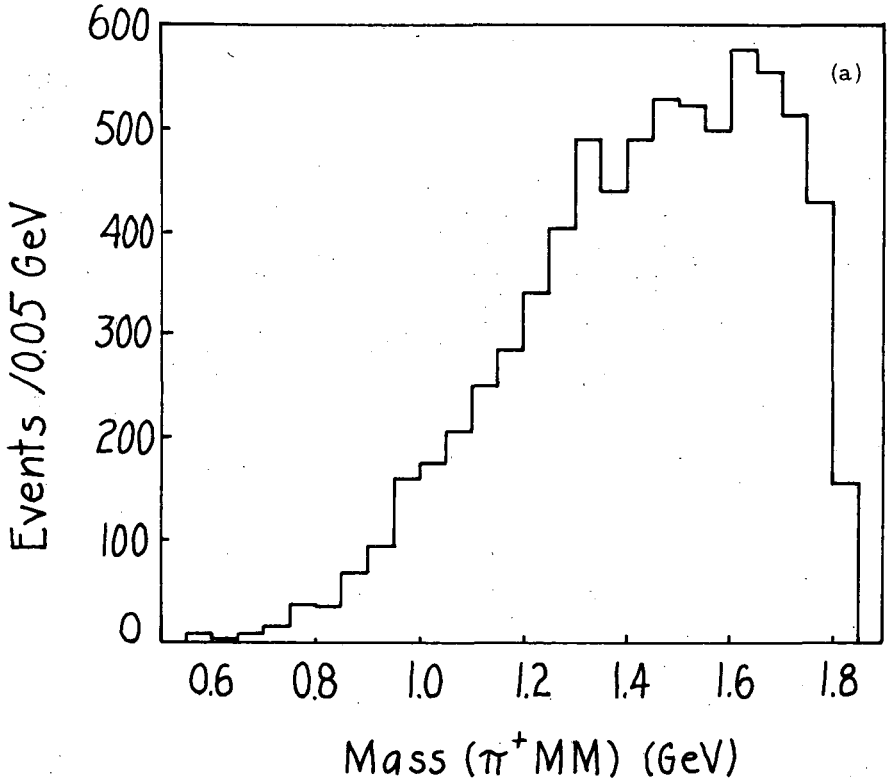

XBL715-3518

Fig. 54. (π^+MM) spectra for the final state pπ^+MM and a) all t_p b) $t_p < 1.2$ (GeV/c)^2.

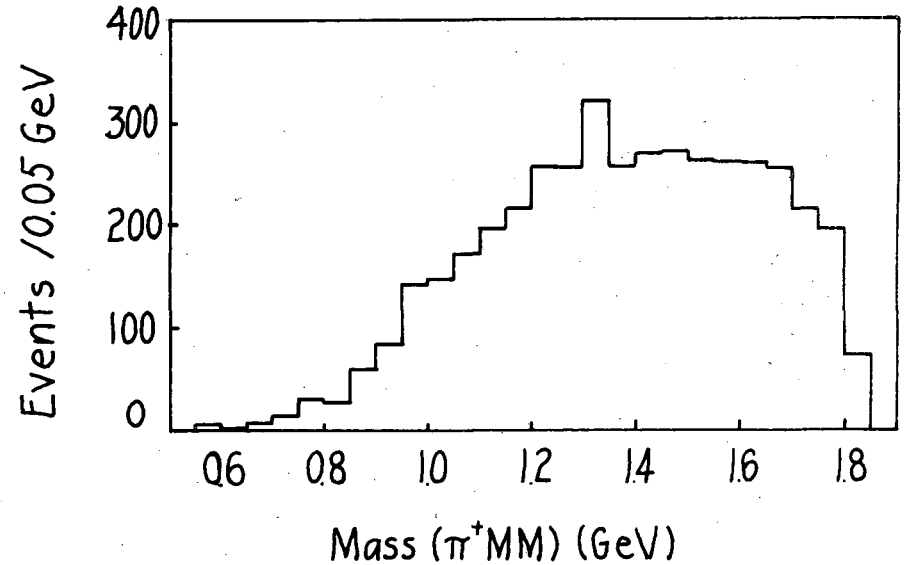

Fig. 54b.

XBL715-3519

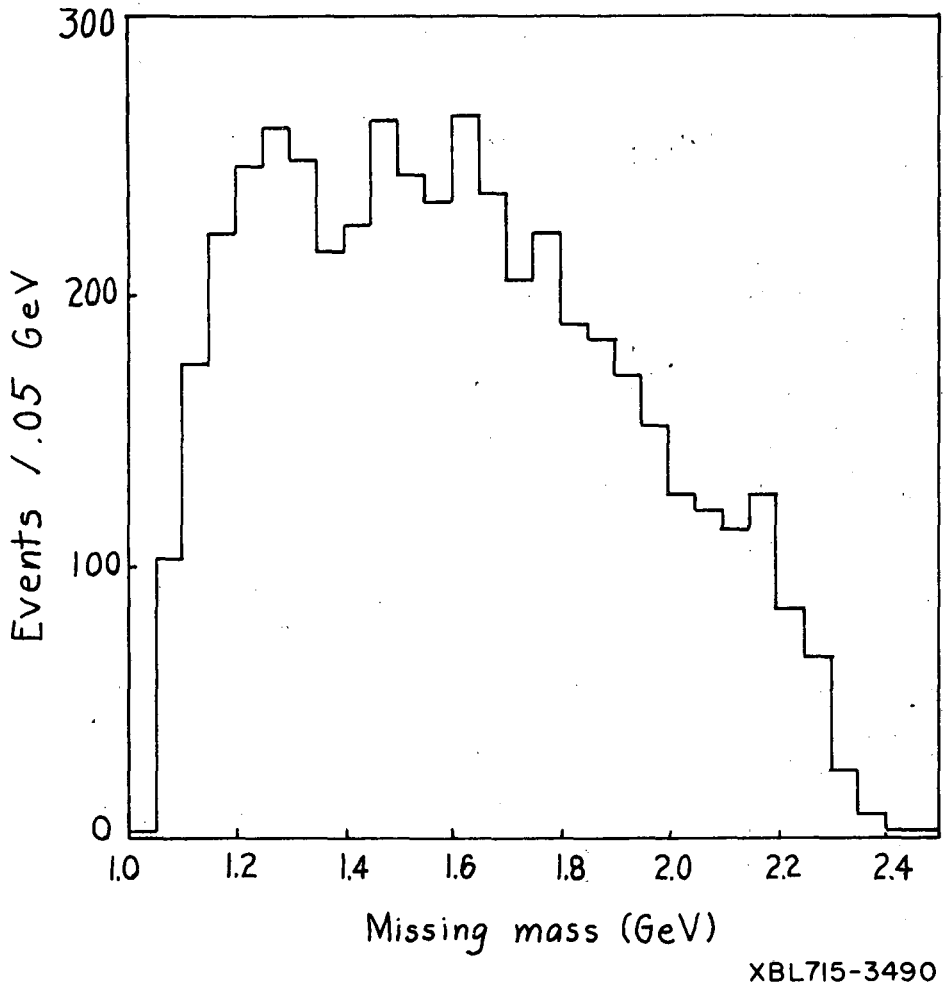

Fig. 55. Missing-mass spectrum for the final state $\pi^+\pi^+$MM.

LEGAL NOTICE

This report was prepared as an account of work sponsored by the United States Government. Neither the United States nor the United States Atomic Energy Commission, nor any of their employees, nor any of their contractors, subcontractors, or their employees, makes any warranty, express or implied, or assumes any legal liability or responsibility for the accuracy, completeness or usefulness of any information, apparatus, product or process disclosed, or represents that its use would not infringe privately owned rights.

TECHNICAL INFORMATION DIVISION
LAWRENCE BERKELEY LABORATORY
UNIVERSITY OF CALIFORNIA
BERKELEY, CALIFORNIA 94720